

erklärt werden können, wenn der “return current” berücksichtigt wird. Wenn sich ein Strom von Elektronen entlang von magnetischen Feldlinien von der Korona zur Chromosphäre bewegt wird erwartet, dass sich ein Rückstrom in entgegengesetzter Richtung ausbildet. Die Beobachtungen und das erweiterte Modell zeigen wie wichtig dieser “return current” ist.

In einem zweiten Teil werden Beobachtungen von sogenannten “Pre-flares” präsentiert. Diese früheste Phase eines Flares kann nicht mit dem klassischen Modell der Chromosphärischen Evaporation erklärt werden, in welchem die Chromosphäre durch das Auftreffen hochenergetischer Elektronen aufgeheizt wird und heisses Gas die magnetischen Bögen füllt. In Pre-flares wird ein Anstieg der Dichte und des Emissionsmasses beobachtet, was auf das Vorhandensein von Evaporation hinweist. Allerdings werden keine Signaturen von hoch-energetischen Elektronen beobachtet. Wir zeigen, dass Energietransport in Form von Wärmeleitung anstelle schneller Elektronen diese Beobachtungen erklären kann.

Contents

Abstract	v
Zusammenfassung	vii
1. Introduction	1
1.1 The laboratory at our doorstep	1
1.1.1 A century of solar coronal observations	1
1.1.2 The Sun in X-rays	4
1.1.3 Solar flares	7
1.1.4 RHESSI	9
1.2 Particle kinematics in solar flares	11
1.2.1 Particle acceleration	13
1.2.2 Propagation	17
1.3 Outline	19
2. Size dependence of solar X-ray flare properties	21
2.1 Introduction	22
2.2 Event selection and data reduction	24
2.2.1 Data selection	24
2.2.2 Background subtraction and peak time selection .	26
2.2.3 Spectral fitting	27
2.2.4 Flares with more than one fitting model	32
2.3 Results	32
2.3.1 Non-thermal emission	32
2.3.2 Thermal flare properties compared to non-thermal properties	37
2.3.3 Thermal flare plasma	39
2.3.4 Inspection of exceptional flares	42

2.4	Discussion	43
2.5	Summary and Conclusions	45
3.	Relations between concurrent hard X-ray sources in solar flares	49
3.1	Introduction	50
3.2	Observations, Event Selection and Spectroscopy	51
3.2.1	Event selection	52
3.2.2	Imaging spectroscopy	52
3.3	Results	58
3.3.1	Soft-Hard-Soft (SHS)	58
3.3.2	Difference in spectra between sources of the same event	61
3.4	Discussion	66
3.4.1	Coronal source shows SHS-behavior	66
3.4.2	Soft-hard-soft behavior of the full sun	67
3.4.3	Differences in spectra	67
3.5	Conclusions	69
4.	Exploring the connection between coronal and footpoint sources in a thin-thick target solar flare model	73
4.1	Introduction	74
4.2	Theoretical model	75
4.3	Observations	75
4.3.1	Event selection and spectral analysis	75
4.3.2	Density and critical energy	78
4.3.3	Position of coronal source at different energies	79
4.4	Results	79
4.4.1	Energy input into the corona	80
4.5	Discussion	82
4.6	Conclusions	83
5.	Observational evidence for return currents in solar flare loops	85
5.1	Introduction	86
5.2	Thin and Thick target emission	88
5.3	Event description and spectral analysis	88
5.3.1	Spectral fitting and analysis	89

5.4	Method	90
5.5	Results	92
5.5.1	Observed spectra	92
5.5.2	Expected footpoint emission and energy loss . . .	94
5.6	Return current and electric field	96
5.6.1	Results	98
5.7	Discussion	98
5.7.1	Instability	98
5.7.2	Low energy electron cutoff	100
5.7.3	Source inhomogeneity and filling factor	100
5.7.4	Collisions and other possible scenarios	101
5.8	Conclusions	102
6.	Observations of conduction driven evaporation in the early rise phase of solar flares	105
6.1	Introduction	106
6.2	Flare selection	109
6.3	Time evolution of events	111
6.3.1	Spatial evolution	111
6.3.2	Spectral evolution	114
6.3.3	Time evolution of flare parameters	114
6.4	A theoretical model to explain the observations	117
6.4.1	Theory of thermal conduction	118
6.4.2	Observation of thermal conduction	119
6.4.3	Chromospheric evaporation	121
6.5	Discussion	122
6.5.1	Electron beams in the pre-flare phase	122
6.5.2	Influence of assumptions	123
6.5.3	Mode of conduction	124
6.5.4	Acceleration vs. heating	124
6.6	Conclusions	125
7.	Summary and Outlook	127
A.	Units and unit conversions	129
B.	Conversion of photon to electron spectra	131

Bibliography	135
Acknowledgments	141
List of Publications	143
Curriculum Vitae	145

Chapter 1

Introduction

1.1 The laboratory at our doorstep

One of the main differences between astrophysicists and most other physicists is that the former cannot reproduce and study their research objects in the laboratory. We depend on what we get by observations. Photons from all parts of the Universe are the messengers that carry information about distant objects to us. Naturally, that information can be incomplete and difficult to obtain. Among the astrophysicists, solar physicists are in a somewhat privileged situation, as their study-subject is among the closest in our universe. The Sun is the only star of which the surface can be spatially resolved in detail by direct observations, allowing us to study fine structures as small as several hundred kilometers. Further, it is constantly monitored by both, ground based and space born instruments which deliver gigabytes of data every day. In some sense one could call the Sun a laboratory at our doorstep. We cannot change the laboratory setup, but we can study physical processes which may also take place elsewhere in the Universe, for example particle acceleration, in great detail.

1.1.1 A century of solar coronal observations

Because of its closeness, 1 AU or $1.469 \cdot 10^8$ km, the Sun can be and has been studied in more detail than any other star. Large sunspots are observable by the naked eye. Therefore, first observations of sunspots are passed down by the Chinese from 800 BC. With a simple backyard telescope and an $H\alpha$ filter, one can already observe details such

as prominences and filaments. To observe the solar corona, the bright photospheric emission has to be masked. This happens naturally during a solar eclipse. Coronal observations independent of a solar eclipse became possible with the construction of the first coronagraph by Bernard Lyot in 1930. A decade later, solar radio astronomy was born with the first detection of solar radio waves (Hey 1946). Since then, radio spectrometers all over the world have been observing the Sun from centimeter to meter-wavelengths. ETH Zürich has been operating radio spectrometers since 1972, the latest being Phoenix-2, the first digital instrument in the microwave band (Messmer et al. 1999). With the development of radio interferometry, the first radioheliograph was built in 1968 at the Culgoora radio observatory (Labrum 1972). Followed by an observatory near the Japanese village of Nobeyama (Nakajima et al. 1994) and the Naçay radioheliograph (Kerdraon & Delouis 1997).

Radio observations are relatively easy to obtain in the sense that the observed wavelengths are not significantly affected by atmospheric absorption. High quality optical observations are possible from the ground using techniques such as adaptive optics to account for atmospheric disturbances. Higher energetic electromagnetic radiation from extreme ultra-violet (EUV) to X-rays and γ -rays however, is absorbed in the upper earth atmosphere, requiring observations from space. Therefore, a whole new world of solar observations opened up with the beginning of the space age. A multitude of satellites has observed the Sun in wavelengths ranging from optical to EUV and as far as X-rays and γ -rays in the last half a century. The first X-ray observations of the Sun were made in the nineteen-forties on rockets. The first satellites to observe the Sun in EUV and X-rays up to γ -rays were the Orbiting Solar Observatories (OSO 1-8) which observed energies up to 10 MeV. They were complemented by the ESA TD-1A mission (van Beek & de Feiter 1973) and followed by EUV and soft X-ray telescopes on Skylab (Vaiana et al. 1977). The Solar Maximum Mission (SMM, Orwig et al. 1980) was the first satellite to observe the Sun over a full activity-cycle. The GOES satellites of the National Oceanic and Atmospheric Administration (NOAA) are geostationary weather satellites with an additional soft X-ray monitor that measures the solar X-ray emission (Garcia 1994). They have been providing a 24 hour coverage of solar X-ray observations for thirty years. Nowadays, the GOES classification is the main classification scheme used

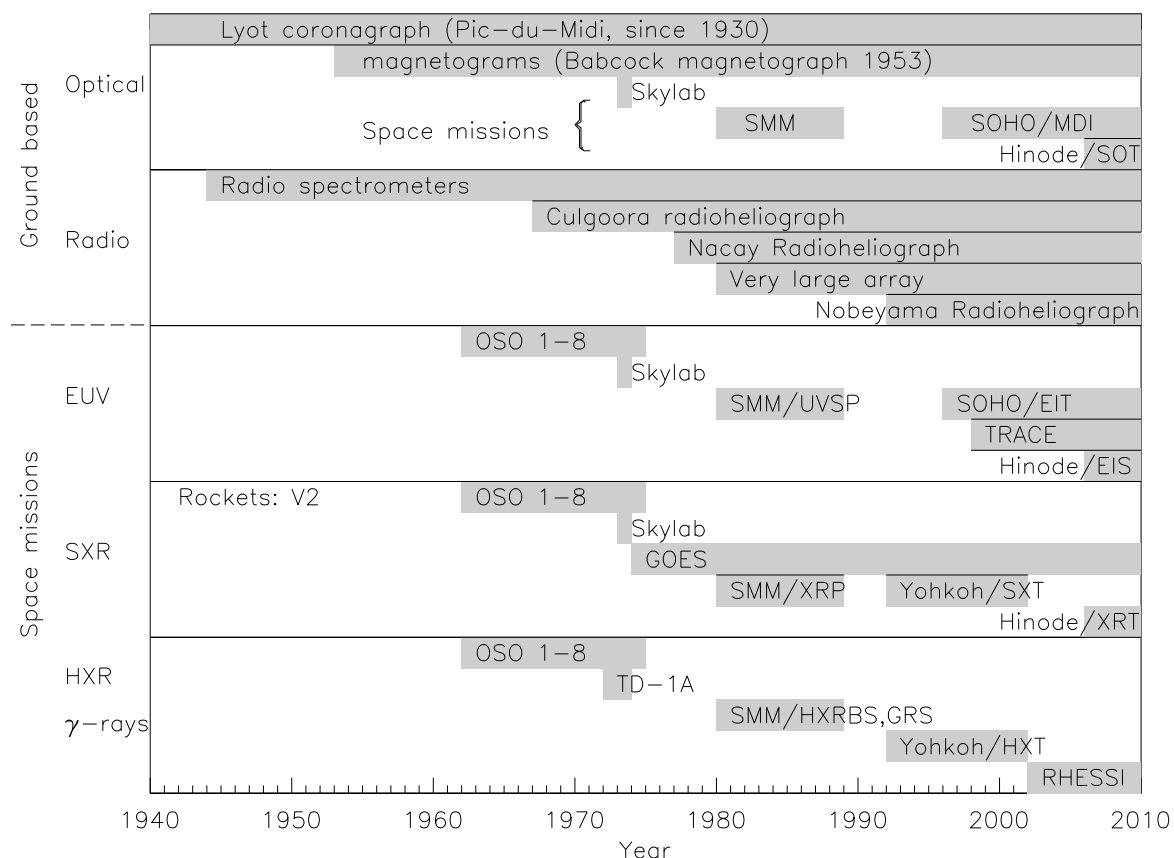


Figure 1.1: Solar observatories, ground based and space borne in the last century (following Aschwanden 2005)

for solar flares. The size of a flare is defined as its peak flux intensity in Wm^{-2} in the GOES 1-8 Å channel. Each order of magnitude in the intensity is associated with a letter as shown in Table 1.1.

In recent years, the most important mission for solar X-ray observations was RHESSI (Lin et al. 2002), currently the only solar instrument covering the wavelength range from hard X-rays to γ -rays. In 2006, the Japanese Hinode mission was successfully launched, carrying an X-ray telescope which observes the soft X-ray (thermal) regime (Golub et al. 2007). An overview of some of the important solar coronal observatories in the last 70 years is given in Fig. 1.1.

The spatial and spectral resolution of the satellites has improved considerably over the past decades. For example, the HXT instrument on the

Flux [Wm^{-2}]	GOES class
10^{-8}	A1
10^{-7}	B1
10^{-6}	C1
10^{-5}	M1
10^{-4}	X1
10^{-3}	X10

Table 1.1: Overview of the GOES flare classification scheme. Intermediate classes are eg. $5 \cdot 10^{-7} \text{ Wm}^{-2} \Leftrightarrow \text{B5}$.

Yohkoh satellite (Kosugi et al. 1992) provided three energy bands in the energy range from 23 keV to 93 keV (23-33-53-93 keV), whereas RHESSI provides a spectral resolution of about 1 keV in that energy range, resulting in much more detailed spectra. Despite or just because of the increasing amount and quality of observational data, many questions in solar physics still remain unanswered.

1.1.2 The Sun in X-rays

The multi-wavelength Sun

In X-rays, the Sun looks completely different from what we are used to by observing it with backyard telescopes. Fig. 1.2 shows the changing face of the Sun observed in visible light, $\text{H}\alpha$, UV and X-rays. The peak of the solar irradiance is in the optical light, which constitutes mostly of continuum emission originating from the photosphere (upper left in Fig. 1.2). The upper right image displays the solar chromosphere in the $\text{H}\alpha$ line of hydrogen at 6562.8 Å. Moving further up in the solar atmosphere, the transition region is visible in emission lines in the EUV (lower left image). Finally, the lower right image shows the solar corona in X-rays.

Emission of the corona

X-ray emission of the Sun originates mostly from the corona, in flares also from lower regions down to the chromosphere. In the quiet Sun, the ob-

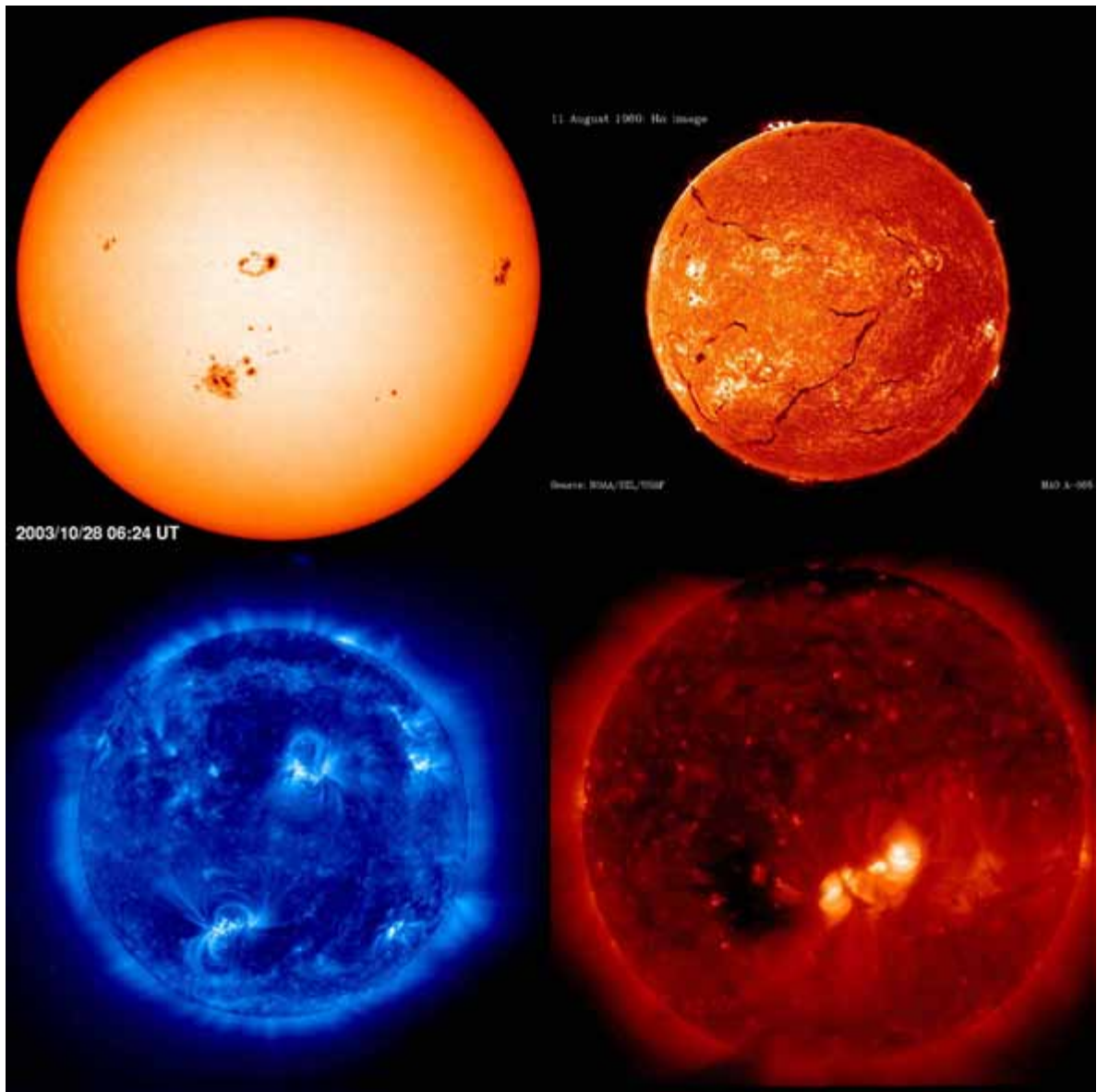


Figure 1.2: The changing face of the Sun. *Top left:* Image of the photosphere in white light with sunspots from SOHO/MDI (ESA & NASA) *Top right:* Image in the $H\alpha$ emission line (6562.8 \AA), displaying the chromosphere (image credit: NOAA/SEL/USAF). Prominences are visible as condensed gas over the limb, dark filaments appear in projection on the disk. *Bottom left:* SOHO/EIT image in the 171 \AA wavelength of the EUV spectrum, illustrating the upper transition region at a temperature of about 1 Mio. K. *Bottom right:* Image in X-rays, showing the corona at a temperature of about 2 Mio. K, observed by Hinode (JAXA/NASA/PPARC). (The size of the solar disc is not to scale).

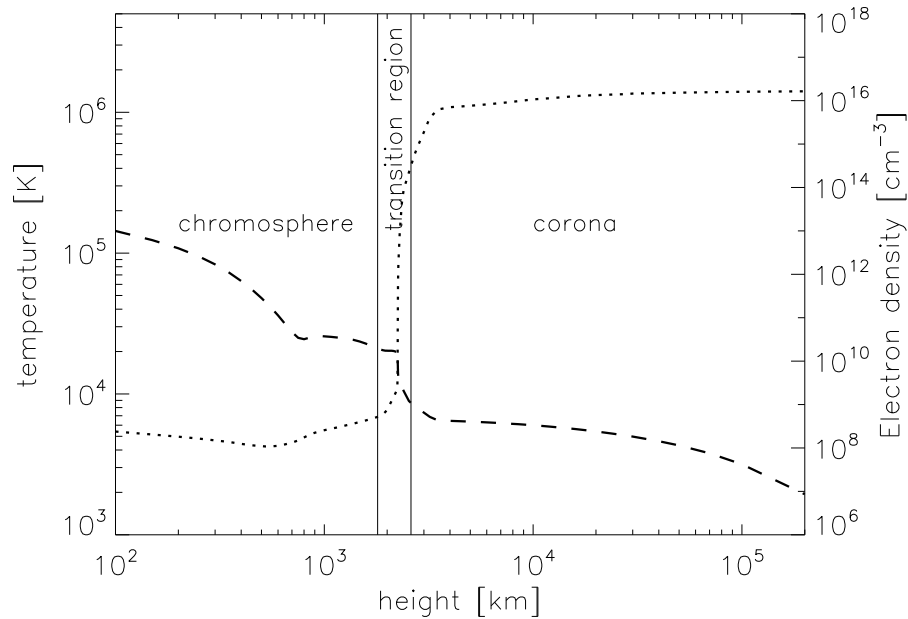


Figure 1.3: Electron temperature (*dotted*) and density (*dashed*) structure of the quiet solar atmosphere (following Benz 2002). The temperature increases by two orders of magnitude from the high layers of the chromosphere to the corona while the electron density decreases considerably.

served emission is hot plasma emission in the form of continuum emission by free electrons, as well as line emission from highly ionized ions. Typical quiet Sun coronal temperatures lie in the range of 1-2 Million degrees. Fig. 1.3 illustrates the electron temperature and electron density structure of the quiet solar atmosphere. In a narrow boundary layer known as transition region, the temperature increases dramatically, while the density decreases with increasing distance from the photosphere. This temperature increase, also known as the *coronal heating problem* is one of the fundamental questions in solar physics and has still not been answered conclusively. An overview of the controversy is given in Aschwanden (2005), reviews can be found in Narain & Ulmschneider (1990) and Narain & Ulmschneider (1996).

Types of X-ray emission

Solar physicists distinguish between two types of X-ray emission, soft - and hard X-rays.

Soft X-rays: Thermal bremsstrahlung emission as well as line emission by excited ions is referred to as soft X-rays (SXR). The associated photon energies lie typically in the range of $\approx 0.1\text{-}15$ keV ($124\text{-}0.8$ Å) but can range up as high as 25 keV (0.5 Å).

Hard X-rays: Photons with energies higher than the SXR energies, up to 300 keV (0.04 Å) are referred to as hard X-rays (HXR). They are thought to be mainly thick or thin target bremsstrahlung emission by high energetic electrons. Often, a power-law, i.e. a straight line in a double-logarithmic representation of the energy/flux spectrum, is observed.

Overall, signatures of a variety of physical processes in the solar atmosphere can be observed in X-rays. Observations in this wavelength range are therefore an important tool to study the physics of the transition region and corona and hopefully solve puzzles such as the coronal heating problem.

1.1.3 Solar flares

Among the various solar activity phenomena, solar flares are particularly fascinating because of their enormous power. Flares can release energies of the order of 10^{32} erg (10^{25} Joule) in seconds to minutes. The energy is thought to be of magnetic origin, being released when magnetic field lines reconnect in the corona. In this process, particles are accelerated to high energies and either escape into interplanetary space along open field lines or precipitate down to the chromosphere along the field lines of a magnetic loop. Collisional interaction with background particles causes them to slow down and eventually stop, emitting non-thermal bremsstrahlung (free-free emission) which is observable in hard X-rays (so-called footpoints). Chromospheric plasma is heated and expands upwards the magnetic loops. This process has been termed chromospheric evaporation. The loops filled with the hot plasma become visible in soft X-rays and EUV.

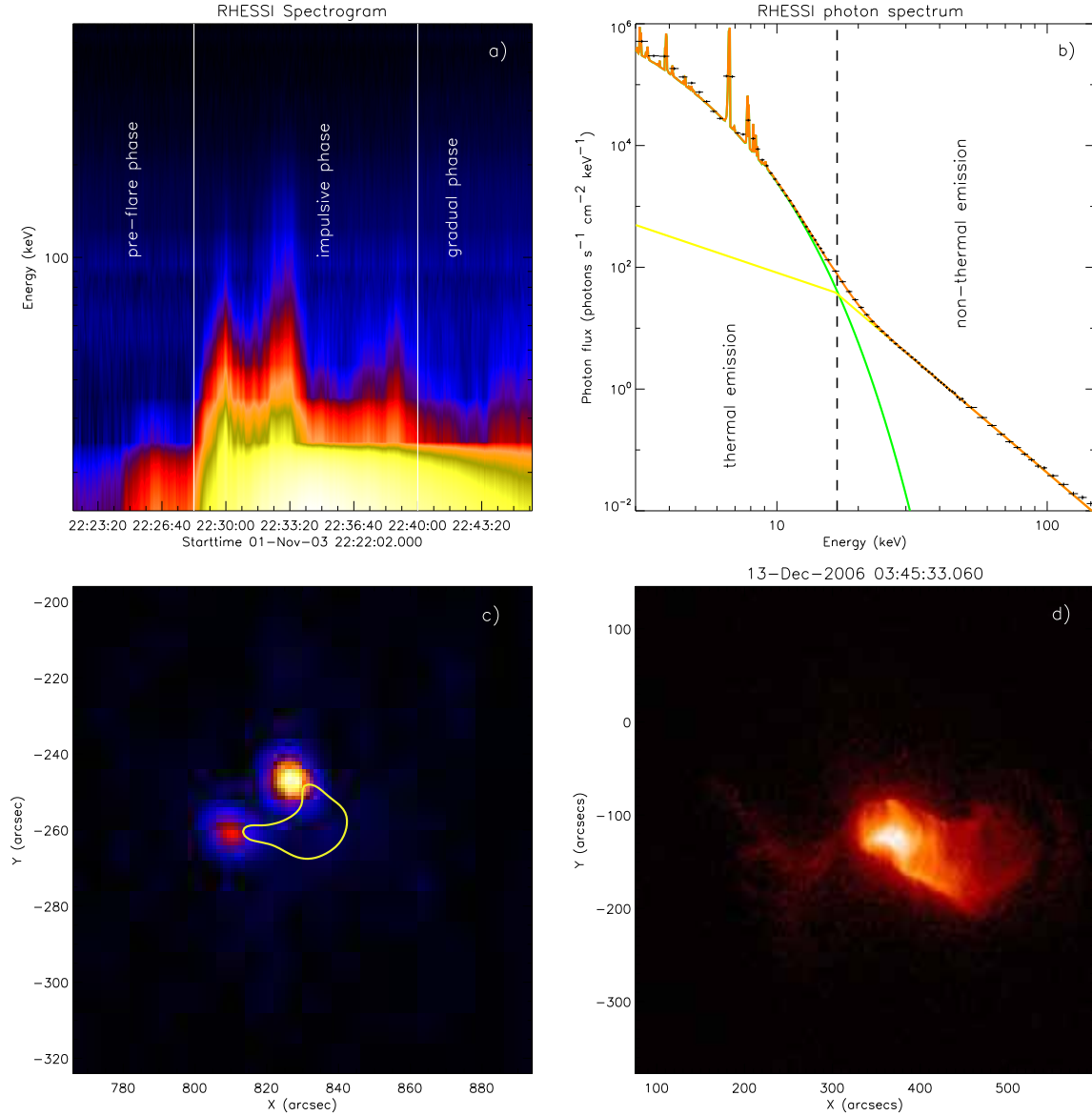


Figure 1.4: RHESSI spectrogram of a typical flare illustrating the three main flare phases (a). b): RHESSI spectrum (*crosses*), taken at the second hard X-ray peak displayed in the spectrogram. The solid lines are fits described in the text. c) is a RHESSI image, taken at the hard X-ray peak in the 25-50 keV energy band. The yellow contour indicates the emission at 6-12 keV. In image d), an arcade of post-flare loops observed by Hinode is shown (JAXA/NASA/PPARC).

Flare time evolution

In the classical view, the evolution of a flare is divided into three phases; a *pre-flare phase*, the *impulsive phase* and the *gradual phase*. Fig. 1.4a displays a spectrogram of a typical flare, where the flare phases are drawn. In the pre-flare phase, an increase in soft X-ray emission is observed. The impulsive phase is characterized by a steep increase in hard X-ray emission. It is thought to be the phase when the main energy release occurs and particles are accelerated. In the gradual phase, particle acceleration stops and the hot plasma slowly cools. In this phase, hot, post-flare loops can often be observed as shown in Fig. 1.4d. However, not all events fit into this picture. Some events display a prolonged, intense pre-flare phase, associated with strong heating, but with no indications of particle acceleration. This phase can last up to several minutes. Other flares start with the impulsive phase and some events are purely gradual with no distinct impulsive phase.

Flare spectrum

Fig. 1.4b shows the X-ray spectrum of a typical flare at the peak of the impulsive phase (crosses). At energies 6-8 keV, the Iron-Nickel line complex, originating from highly ionized Iron and Nickel is shown. A thermal model (Maxwellian, green curve) was fitted, revealing a temperature of $2.2 \cdot 10^7$ K. In the presented model, the emission lines were not fitted. However, a detailed analysis of the line features in suitable events can provide information on the plasma temperature and Fe/H abundance ratios (eg. Phillips et al. 2006). At higher energies, the spectrum has the shape of a power-law $\epsilon^{-\gamma}$ with index $\gamma = 3.8$. This can provide information on the total number of accelerated electrons and the non-thermal energy in the flare (see Appendix B and Saint-Hilaire & Benz 2005).

1.1.4 RHESSI

The Reuven **R**amaty **H**igh **E**nergy **S**olar **S**pectroscopic **I**mager (RHESSI, Lin et al. 2002) was launched on February 12th 2002 and has been observing the Sun for the past 6 years. The observed energy range spans from 3 keV to 17 MeV with an energy resolution of 1 keV at the lowest energies and 5 keV at MeV energies. This energy range covers thermal

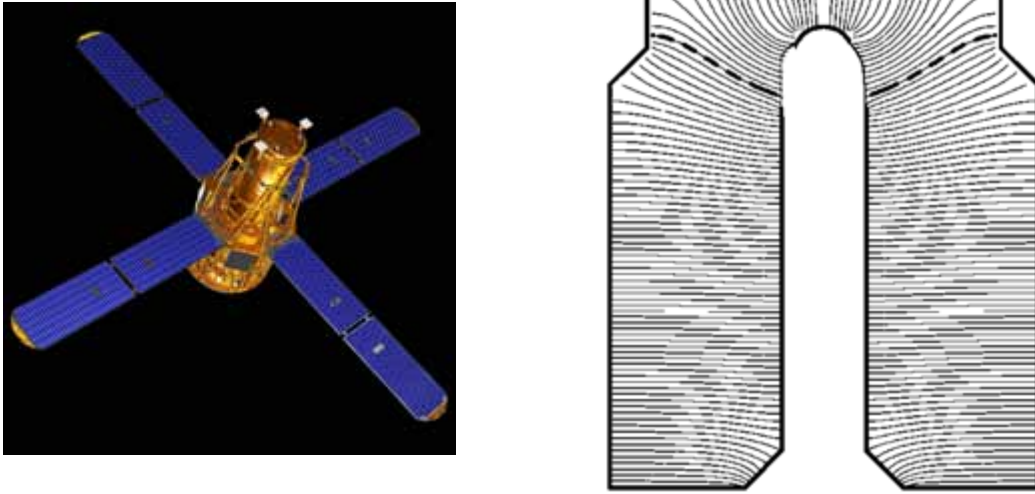


Figure 1.5: Illustration of the RHESSI satellite. The *right* image is an illustration of a detector and the electric field lines across it. The *dashed* line indicates the boundary field line which divides the detector into a front and a rear segment (taken from Smith et al. 2002).

flare emission, emission from non-thermal electrons as well as γ -ray lines and continuum emission from excited ions. The large energy range and high resolution are provided by nine germanium detectors operated at cryogenic temperatures. High voltage applied to the detectors provides an electric field across the detectors. The detectors are separated into two segments (front and rear) by a boundary electric field line, signals are registered separately above and below the boundary line. The front segment is most sensitive to photon energies from 3 keV up to 300 keV. All photons with energy smaller than 100 keV will be stopped in the front segment, while most photons in the γ -ray regime will pass through and be fully stopped in the rear segments. To avoid saturation of the detectors due to very high photons flux in intense flares, two aluminum attenuators (or shutters), a thin and a thick one can be moved in front of the detectors. This provides a wide dynamic range, allowing the study of microflares as well as the largest events. As hard X-rays and γ -rays cannot be focused using currently available techniques, the RHESSI imaging system is based on the rotating modulation collimator technique. Grids of different pitch width are placed in front of the detectors. While the telescope spins around its axis, this results in a modulation curve of the

intensity of the incoming photon flux on each detector. From these modulation curves, images can be reconstructed. The different pitch width and combinations of grids provide varying angular resolution, theoretically as high as 2.3 arcseconds (Hurford et al. 2002).

1.2 Particle kinematics in solar flares

As denoted in Sect. 1.1, the Sun can be used to study physical processes that take place all over the Universe. Solar flares accelerate a large amount of particles to very high energies, but particle acceleration takes place at many sites in the Universe, including the earth's magnetosphere, supernovae and active galactic nuclei. The differential cosmic ray spectrum is a composite of 3 power-laws, not unlike a solar flare spectrum. When the particles are released from their acceleration site they may suffer collisions with other particles or interact with plasma waves. They can be deflected by magnetic fields or slowed by an electric potential. Such transport effects can change the initial distribution of a particle spectrum. It is tempting to use solar flares as proto-type particle accelerators, however Longair (1992) gives a word of warning at the beginning of Sect.12.6 of his book

This section will be a severe disappointment to those astronomers who might look to solar flares for guidance in solving the problem of accelerating high energy particles in galactic and extragalactic systems.

Indeed, acceleration in strong shocks is discussed as the primary acceleration mechanism for cosmic rays while electric DC field acceleration is more specific to solar flares. Stochastic acceleration in a second order Fermi type mechanism may be found in all settings. Therefore, solar flares may not solve the general problem of particle kinematic processes in the Universe in the end but many processes can be studied in flares with an accuracy never achievable for cosmic rays and valuable discoveries can be made.

The kinematics and physical processes of solar flares can be divided into 3 main phases (see also Fig. 1.6).

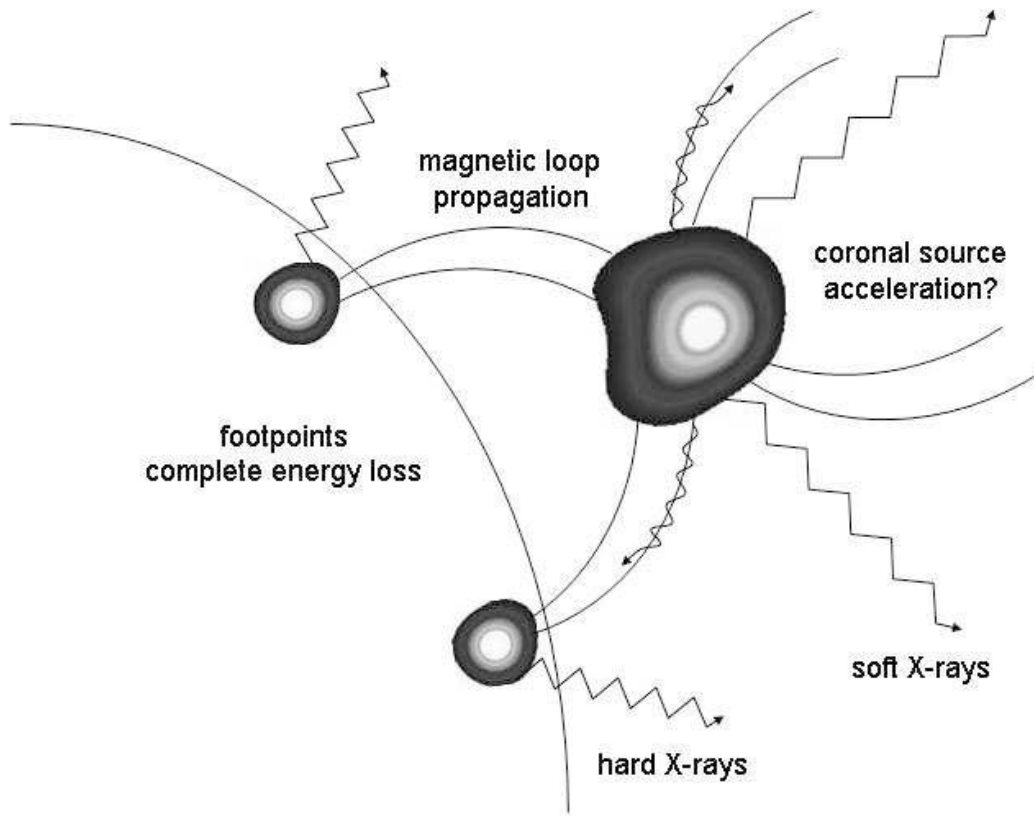


Figure 1.6: Generic flare model, illustrating the phases of particle acceleration, propagation and stopping. Acceleration is generally thought to take place in a region in the corona. In the process, the plasma at the acceleration site is heated and becomes observable in soft X-rays as coronal source. In sufficiently high densities, non-thermal bremsstrahlung may also be produced. The particles then precipitate down along the field lines of a magnetic loop to the chromosphere. Hard X-ray bremsstrahlung emission is observed from chromospheric footpoints when the particles lose all their energy in the dense gas.

1. Particle acceleration: particles are accelerated via a mechanism such as stochastic acceleration or DC electric field acceleration (see 1.2.1).
2. Propagation: Particles propagate down to the chromosphere along magnetic field lines (see 1.2.2).
3. Complete energy loss: When reaching the chromosphere, particles are fully stopped in the dense ambient plasma, emitting HXR bremsstrahlung.

In this picture, the propagation part is commonly assumed to be force free, i.e. the particles are freely streaming towards the chromosphere. As Chapter 5 will show, this is a simplification which is often not consistent with reality.

1.2.1 Particle acceleration

In the following sections, the acceleration of electrons will be discussed. In flares and other acceleration sites, protons and other ions are also accelerated, and the here presented acceleration mechanisms can often account for the acceleration of those particles, as well.

There are three main acceleration mechanisms thought to be of importance in solar flares, stochastic acceleration by wave-particle interaction (second order Fermi acceleration), shock-acceleration (first order Fermi acceleration), and DC-electric field acceleration. All three mechanisms are shortly summarized below. A more detailed description including the strenghts and weaknesses of the individual models in the context of particle acceleration in solar flares can be found in the review by Miller et al. (1997).

Second order Fermi acceleration

This type of acceleration was initially proposed by Fermi (1949) to explain the cosmic ray spectrum. In his original work he assumes a stochastic process in which particles are accelerated by collisions with magnetic clouds in the interstellar medium. However, this process is also conceivable in all settings involving dynamic magnetic fields. A big achievement

of Fermi acceleration is that one can reproduce a power-law spectrum as is observed in cosmic rays as well as solar flares. For this reason, the original Fermi acceleration shall be reviewed here. In Fermi's derivation it is assumed that charged particles are reflected by 'magnetic mirrors' which move randomly with an average velocity V . It is further assumed, that the particle distribution is isotropic between the mirrors and the particles are scattered randomly after an encounter. Statistically, head-on collisions are more likely than following collisions for particles with velocity $v > V$, therefore particles will gain energy on average. If an escape time τ_{esc} is introduced, after which a particle leaves the acceleration region, a power-law of the energy/particle density spectrum can be recovered. Following the treatment in Longair (1992), we compute the energy increase rate and the resulting spectrum.

Derivation of energy increase rate and power-law spectrum:

Assume an infinitely massive magnetic cloud, moving at velocity V . The particles hit the mirror under an angle θ relative to the normal to the surface of the mirror. In a relativistic treatment, the energy of the particle in the center of momentum frame of the cloud is then:

$$E' = \gamma_V(E + Vpcos\theta), \quad (1.1)$$

where γ is the Lorentz factor. Transforming back to the observer frame, the energy gain ΔE of a particle in an encounter is

$$E'' - E = \Delta E = \frac{2Vvcos\theta}{c^2} + 2\left(\frac{V}{c}\right)^2 \quad (1.2)$$

in second order of V/c . Assuming that the particle is randomly scattered between encounters in the cloud, a mean increase in energy can be found by averaging over the pitch angle θ . In the relativistic limit, an average energy gain per collision of

$$\left\langle \frac{\Delta E}{E} \right\rangle = \frac{8}{3} \left(\frac{V}{c} \right)^2 \quad (1.3)$$

is found. The mean energy increase rate dE/dt can be found by computing the average time between collisions from the mean free path of a

particle.

$$\frac{dE}{dt} = \frac{4}{3} \left(\frac{V^2}{cL} \right) E = \alpha E \quad (1.4)$$

Recovering a power law in particle density:

We start from the diffusion-loss equation in equilibrium for the particle density $N(E)$:

$$\frac{dN}{dt} = D\nabla^2 N + \frac{\partial}{\partial E}[b(E)N(E)] - \frac{N}{\tau_{esc}} + Q(E) \quad (1.5)$$

where $D\nabla^2 N$ is the diffusion term, $b(E) = -dE/dt$ is the energy loss term, τ_{esc} is the particle escape time and $Q(E)$ the source term. Assuming a steady state with no diffusion and no external sources, the first term on the lefthand side, as well as the first and the last term on the righthand side can be neglected. Finally, by replacing $b(E)$ with Eq. 1.4 one gets:

$$-\frac{d}{dE}[\alpha EN(E)] - \frac{N(E)}{\tau_{esc}} = 0 \quad (1.6)$$

which can be written in differential form:

$$\frac{dN(E)}{dE} = - \left(1 + \frac{1}{\alpha\tau_{esc}} \right) \frac{N(E)}{E} \quad (1.7)$$

The solution of this differential equation is a power-law given as:

$$N(E) = const. \cdot E^{-x} \quad (1.8)$$

with $x = 1 + \frac{1}{\alpha\tau_{esc}}$.

In flares, second order Fermi acceleration is encountered in form of a stochastic process of wave-particle acceleration. Particles can interact with waves, if they move with approximately the phase velocity of the wave or their gyrofrequency is in resonance with the wave frequencies. In a real setting such as the solar corona, a large number of different waves will be present, some are expected to have constructive interference with the motion of a particle, some destructive. In this stochastic process,

parts of a particle distribution will experience a net gain in energy. One specific model, termed transit time damping was presented by Miller et al. (1996). The model was extended by Grigis & Benz (2006) to account for particle escape and transport processes. With their model, Grigis & Benz (2006) could explain the soft-hard-soft time evolution of flare spectra. Furthermore they could reproduce observed flare spectra by RHESSI.

First order Fermi acceleration in shocks

As opposed to the second order Fermi acceleration, particles only encounter head-on collisions at shock fronts. The resulting energy increase rate (compare Eq. 1.3) will go as the first power of (V/c) , thus the term first order Fermi acceleration. As a result, this process is more efficient than second order Fermi acceleration. Generally, two types of shock acceleration are distinguished; shock-drift acceleration and diffusive shock acceleration. In the former, each particle has only a single encounter with the shock front while in the latter a particle can be reflected by moving fronts several times. A review on the history and the various mechanisms of particle acceleration in shocks can be found in Jones & Ellison (1991). For the case of flares, shock acceleration has been used to explain the acceleration of high energetic protons (eg. Bai et al. 1983).

DC electric field acceleration in solar flares

The general expression for the acceleration of a particle in electromagnetic fields is

$$\frac{d}{dt}(\gamma m \mathbf{v}) = e(\mathbf{E} + \mathbf{v} \times \mathbf{B}) \quad (1.9)$$

For the acceleration of electrons in electric DC fields in the flare environment, collisions of the accelerated electrons with other electrons in the distribution have to be taken into account. The general equation of motion for an electron in the presence of an electric field, including collisions, is:

$$m_e \frac{dv_{\parallel}}{dt} = eE_{\parallel} - \nu_e m_e v_{\parallel} \quad (1.10)$$

where it is assumed that the particles move parallel to the electric field. The second term on the righthand-side represents the deceleration by

collisions where ν_e is the collision frequency. The collision frequency in Eq. 1.10 for electron-electron collisions can be written as:

$$\nu_e = \frac{e^4 n_e \ln \Lambda}{2\pi \epsilon_0^2 m_e v^3} \quad (1.11)$$

where n_e is the electron density, $\ln \Lambda$ the coulomb logarithm (typically around 20 in the corona), m_e the electron rest mass and k_B the Boltzmann constant. As a consequence of the v^{-3} dependence of the collision frequency, collisions are less and less important the higher the velocity of a particle. Above a certain threshold velocity V_c , the electrons are accelerated without significant slowdown by collisions. This is called electron runaway. Likewise, there exists a critical electric field for a given temperature and density. In electric fields exceeding this so-called Dreicer field, all electrons are runaway. In flares, so-called sub-Dreicer as well as super-Dreicer acceleration of electrons are studied.

However, one of the fundamental problems in electric field acceleration is the generation of an electric field capable of accelerating particles (i.e. parallel to the magnetic field). The solar coronal plasma can be approximated as ideal plasma with infinite conductivity, therefore, following Ohm's law

$$\mathbf{E} + \mathbf{v} \times \mathbf{B} = 0. \quad (1.12)$$

Possible scenarios for electric field acceleration have been proposed by e.g. Litvinenko (1996) who investigates super-Dreicer acceleration in large reconnecting current sheets or Holman (1985) for sub-Dreicer acceleration.

1.2.2 Propagation

As seen above, particles can be accelerated as well as slowed by electric fields or deflected by magnetic fields. Further, they can have collisional encounters with other particles, losing energy in the process and being deflected from their initial path. Two main mechanisms of transport processes may be important in solar flares; collisional energy loss and non-collisional energy loss. Both are shortly discussed here.

Collisional losses

Electrons loose their energy in close encounters with ions and other electrons. The amount of energy lost and the time it takes until a particle is fully stopped depends on the initial electron energy, and the column depth $N = n_e \cdot l$ the electron passes. Here, n_e is the particle density of the surrounding plasma and l is the path length the electron travels. The column depth N_{stop} necessary to stop a particle completely can be approximated to

$$N_{stop} \approx 10^{17} E_0^2 \quad [\text{cm}^{-2}] \quad (1.13)$$

where E_0 is the initial electron energy in keV (Tandberg-Hanssen & Emshie 1988). In the classical flare scenario, energy loss by collisions is most important in the chromosphere, where electrons of all energies are fully stopped. It may also be important if there is a dense region in the corona (coronal source) that the particles pass from the acceleration site to the chromosphere. In such a region, not all electrons will be fully stopped, but the initial (accelerated) electron spectrum will be altered. Typical column densities in average flare loops are in the range of 10^{18} cm^{-2} , therefore, only very low energetic electrons are expected to be influenced at all by the passage through the loop.

Non-collisional losses due to electric field

The most obvious means of non-collisional losses for flare beam particles are electric fields. Assuming an electric field parallel to the particle velocity and zero magnetic field, the energy \mathcal{E}_{loss} a particle loses in the electric field E can directly be derived from Eq. 1.9. For the non-relativistic case we get

$$\mathcal{E}_{loss} = \int eE \, ds \quad (1.14)$$

where e is the elementary charge and s the distance the particle traveled. The energy lost is independent of the initial electron energy. Therefore, the low energetic electrons in a given distribution are most affected. Contrary to the collisional case, there will be no observable radiative signature if an electron loses energy by non-collisional means. Therefore, we need indirect measures to assess this case. Chapter 5 will illustrate how we can investigate energy losses due to return currents and the attributed electric field in flare loops. Figure 1.7 compares the influence of collisional

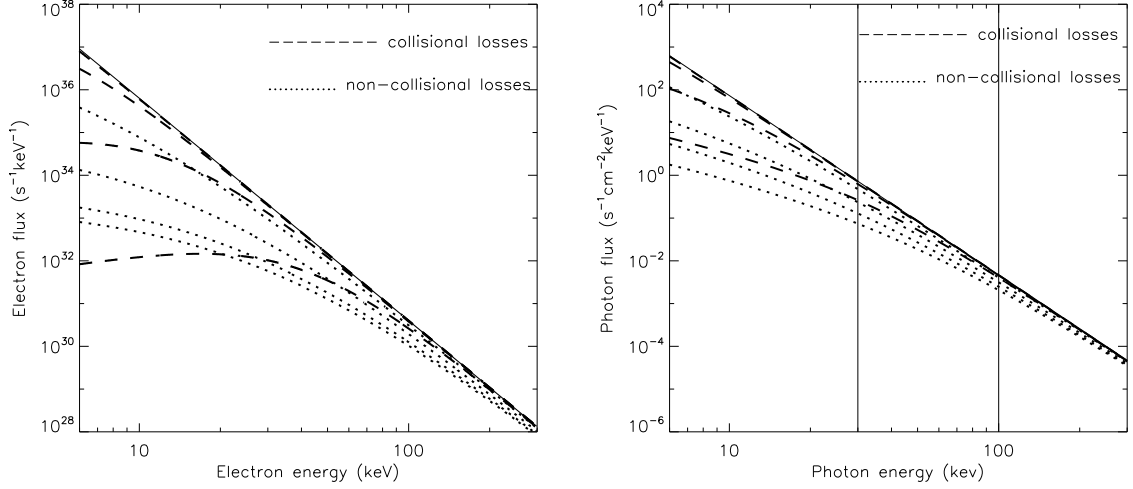


Figure 1.7: Influence of energy loss processes on an initial power-law electron spectrum (*left*) and the resulting observed photon spectrum (*right*). The vertical lines outline the non-thermal energy range observed in an average flare.

and non-collisional losses for different column densities and energy loss. The non-thermal energy range over which most flares are observed is indicated. The Figure shows that the spectra are not power-laws anymore, but slightly curved. The notion of power-laws goes back to the days when the energy resolution of our instruments in this energy range was orders of magnitude less than nowadays. Further, Fermi acceleration can reproduce power-laws. However, many observations of RHESSI flares reveal curved spectra. They are often fitted with two power-law components of different slope. Transport processes, as shown above, could explain those non-power-law spectra. However, there is increasing evidence that the acceleration process itself can also be responsible for such spectra. The transit time damping model Grigis & Benz (2006) results in curved spectra.

1.3 Outline

In the previous sections, an overview of the current state of flare research was given. Various and sometimes contradictory theoretical models and numerical simulations of particle acceleration and propagation

exist. Some are based on observations or explain observations at least qualitatively. In the following chapters, new observations of flares are presented and compared to existing theory in order to achieve a better understanding of particle acceleration and propagation in flares.

In Chapter 2, a statistical survey of flares of different intensity is presented in order to answer the question whether small flares are just scaled down versions of larger ones or whether their intrinsic properties are different.

Chapter 3 introduces the technique of imaging spectroscopy. This technique is used to study the relation between concurrent X-ray sources in flares. The time evolution of the individual source spectra may provide clues about the acceleration site and mechanism, while the quantitative differences between the individual source spectra can help understanding transport processes in flare loops.

In Chapter 4, the relations between individual sources as found in Chapter 3 are compared to a simple theoretical flare model. It is shown that the RHESSI data with its improved spectral resolution compared with previous instruments does not fit the theoretical predictions in most cases.

With Chapter 5, the simple model from Chapter 4 is expanded. By including transport effects the observations can be explained.

Chapter 6 shifts the focus from the impulsive flare phase to the pre-flare phase of events with pronounced heating. Here we compare energy transport by electron beams with thermal conduction.

Although the work presented here provides answers to some puzzles in modern flare physics, a lot of questions still remain open. Those are briefly addressed in an Outlook.

Chapter 2

Size dependence of solar X-ray flare properties *

M. Battaglia¹, P. Grigis¹, and A. O. Benz¹

Abstract

Non-thermal and thermal parameters of 85 solar flares of GOES class B1 to M6 (background subtracted classes A1 to M6) have been compared to each other. The hard X-ray flux has been measured by RHESSI and a spectral fitting provided flux and spectral index of the non-thermal emission, as well as temperature and emission measure of the thermal emission. The soft X-ray flux was taken from GOES measurements. We find a linear correlation in a double logarithmic plot between the non-thermal flux and the spectral index. The higher the acceleration rate of a flare, the harder the non-thermal electron distribution. The relation is similar to the one found by a comparison of the same parameters from several sub-peaks of a single flare. Thus small flares behave like small subpeaks of large flares. Thermal flare properties such as temperature, emission measure and the soft X-ray flux also correlate with peak non-thermal flux. A large non-thermal peak flux entails an enhancement in both thermal parameters. The relation between spectral index and the non-thermal flux is an intrinsic feature of the particle acceleration process, depending on flare size. This property affects the reported frequency distribution of flare energies.

* This chapter is published in *Astronomy & Astrophysics* **439**, 737 (2005)

¹ Institute of Astronomy, ETH Zurich, CH-8092 Zurich, Switzerland

2.1 Introduction

Do small flares differ from large flares? In the simplest flare scenarios small flares are just scaled down versions of large flares. This is predicted explicitly in theories that envision flares as a kind of avalanche process, consisting of many small elements (Lu & Hamilton 1991; Lu et al. 1993). On the other hand, one could speculate that a flare changes the environment of an active region and, in its course, alters the properties of the elementary events. Such an effect would be a feedback effect, thus a secondary phenomenon. However, big flares could be genuinely different because the initial conditions that lead to them may be more demanding on some plasma parameters that finally not only make them bigger but qualitatively dissimilar.

Kahler (1982b) noted that there is a statistical correlation between solar flare energy release and the observation of certain flare manifestations. This so-called ‘Big Flare Syndrome’ states that large flares tend to be associated with phenomena that may not be directly related to each other, such as solar protons (Kahler 1982a), Type II and IV radio bursts (Kahler 1982a), decimeter radio emissions (Simnett & Benz 1986), coronal mass ejections (Dougherty et al. 2002), and white light flares (Matthews et al. 2003). A simple interpretation of the Big Flare Syndrome proposes that the various signatures just get above the threshold for observations in large events (Kahler 1982a). However, some radiations do not increase linearly with flare size. Such a behavior was e.g. recently reported for the energy in decimeter type IV bursts, increasing with about the fifth power of the GOES soft X-ray flux (Benz et al. 2005).

A quantitative difference between small and large flares was found in thermal soft X-ray emission. Feldman et al. (1996) report an increase of temperature T with the flare soft X-ray emission, defined by the GOES peak flux F_G at 1-8 Å (1.55-12.4 keV). The average relation is approximately

$$F_G(T) = 3.5 \cdot 10^{0.185T-9.0}, \quad (2.1)$$

where the flux is in Wm^{-2} and the temperature in units of 10^6 K. They also find a correlation between emission measure and temperature which has been explained theoretically by Shibata & Yokoyama (1999) based on a balance between magnetic reconnection and conductive cooling. Feldman et al. conclude that if a flare is the collection of subresolution events,

the plasma properties of the events occurring during peak emission of large flares and small flares must be different.

Here we ask whether the characteristics of *hard* X-rays emitted by the non-thermal electrons accelerated in solar flares are different in small and large flares. Except for the rare thermal flares, the energy distribution of hard X-ray flare photons follows a power-law. Its index γ usually starts with a high value ('soft' radiation), reaches a minimum at peak flux and increases at the end (as noticed already by Parks & Winckler (1969)). This 'soft-hard-soft' (SHS) behavior is also found in sub-peaks and has recently been analyzed quantitatively for the first time by Grigis & Benz (2004), henceforth GB04) using RHESSI observations. The SHS evolution of individual flares and subpeaks indicates a change in the acceleration process in the course of a flare. It can be visualized roughly by the non-thermal spectrum in log-log representation moving down and up at high energies with a fixed point in the flux-index plane, at an energy of 6.5 - 12.5 keV (average 9 keV; GB04). Although this 'pivot' point may be virtual (i.e. an extrapolation beyond measured data), its location is a characteristic of the electron acceleration process and the subsequent diffusion in energy.

For all rise and decay phases in several subpeaks of 24 flares, GB04 find the relation

$$\gamma = AF_{35}^{-\alpha}, \quad (2.2)$$

where F_{35} is the fitted non-thermal flux at 35 keV, and $\alpha = 0.197 \pm 0.003$. Does the same relation hold between the flux and spectral index at peak time for flares of different size? Another question is whether the flares of different size behave in the average like the subpeaks of one flare. X-ray data of a large number of flares, small and large, have been registered by the Ramaty High Energy Solar Spectroscopic Imager (RHESSI Lin et al. 2002). Section 2.2 describes how an equal number of flares in each decade of peak GOES flux was selected. In Sect. 2.3, the characteristic values of thermal and non-thermal emissions at peak flux are compared as a function of flare size. The results are discussed and compared to previous work in Sect. 2.4, and conclusions drawn in Sect. 2.5.

2.2 Event selection and data reduction

The RHESSI satellite observes the full Sun from 3 keV to 17 MeV since February 2002. In this study, the high spectral resolution (1 keV) of RHESSI's germanium detectors is utilized to study the hard X-ray flare emission below 300 keV. This energy range is dominated by a thermal part at the lower end, usually superposed by a non-thermal part with a power-law spectrum at higher energies. The high spectral resolution allows for the first time to separate and to analyze the non-thermal component where it comprises most photons in a large number of flares. The same analysis also yields information on the thermal X-ray emission in the 3–20 keV range. It is supplemented by soft X-ray observations from the GOES satellite Garcia (1994).

We selected 100 well observed flares from GOES class B1 to X1 from the time between RHESSI launch and April 5th 2004, using the RHESSI Experimental Data Center (HEDC, Saint-Hilaire et al. 2002) at ETH Zürich. The selection process aimed at having a statistically representative sample of flares over the whole time period and from different active regions.

2.2.1 Data selection

We took all events with an image in HEDC, giving their location on the solar disc, and present in the RHESSI-flare-list of April 5th, 2004. This ensured that only solar events were selected and yielded a list of 6039 flares. As we wanted to arrange the flares according to their GOES class, flares without or with bad GOES data in the corresponding time interval were removed from the list. This second step ended with a list of 5871 flares.

To get a uniform distribution of events in flare size, flares were sorted according to their GOES peak flux (without background subtraction). The flux range B1 to X1 was divided into 10 equally wide bins on a logarithmic scale. For each of the 10 bins, 10 events were randomly chosen. A flare had to fulfill the following criteria to be acceptable:

1. The start of the flare and its peak hard X-ray emission had to be well observed. This should guarantee that we did not miss any

interesting parts and allow a good background selection.

2. The attenuation state had to be constant for a period of 4 minutes centered at hard X-ray peak time.
3. The front decimation weight had to be less or equal to 2, to better study the thermal emission. There was an exception from this rule for GOES classes M5 to X1, because in this bin there were just 8 events. Thus every single flare that fulfilled the first 2 criteria has been taken to have a sample as large as possible.
4. For flares in GOES class B1 to B9, there had to be no attenuation and decimation, because of the weak emission of these flares and the low count rates.
5. There must be no enhanced flux of charged particles in the satellite environment a few minutes before and after peak time.

We additionally discarded small flares occurring during the decay phase of a larger event since in such cases it is not possible to separate the emissions of the two events.

For each of the selected flares we performed a spectral analysis. We chose the longest time interval around flare peak time without gaps and with RHESSI in sunlight, and we created a series of spectra with a time bin with of one RHESSI rotation period (approximately 4 seconds). The energy-bin width was chosen fine enough to resolve the thermal and non-thermal spectra, but not so fine that statistical errors became too large. In our case that meant a binning of 1 keV from 3–50 keV (with exception of the range 6–12 keV for the larger flares (C3–X1), where the binning was 0.3 keV), and a larger binning above 50 keV. With these bin widths, a clear separation between the thermal and non-thermal spectrum is possible. For smaller flares, a wider binning was applied for energies of 20 keV and higher as there is less flare emission above that energy. Only the data from the front segments, without detector 2 and 7, were used (in case the transmitter was active during the chosen time interval, detector 8 was also omitted).

For 7 events, no spectrum files could be produced. One event had the lifetime below 90% at peak time and therefore was not acceptable for spectroscopy. This left us with 92 events.

Selection effect for small flares

The RHESSI flare list reports events automatically flagged by the software when the emission in the 12–25 keV band increases. This energy range contains some non-thermal emission of microflares (Benz & Grigis 2002; Krucker et al. 2002)). However, weak GOES events tend to be lost in the RHESSI background in this energy range. Therefore, the RHESSI flare list misses many soft X-ray events of lower GOES class. We have tried to compensate for it by choosing manually 14 flares from the observing summary light curves that did not have a flare flag. For all of those events, the non-thermal emission was however too small to perform a spectral fitting in such a way that the event could be used meaningfully in the further analysis. Thus there remains a selection effect: for low GOES classes, events with large 12–25 keV flux are preferentially selected. Comparisons between non-thermal emission and thermal emission (GOES class), where this effect may play a role, must be treated with special attention. We will point them out in the discussion (Sect. 2.4). The influence of the selection effect on the relation between the non-thermal parameters is shown in Fig. 2.2.

2.2.2 Background subtraction and peak time selection

For each event we subtracted the background and performed a spectral fitting at the time of maximum emission in the hardest observable peak. As the spectral index changes with time, we chose a fitting time-interval of only 4 s to have a value for the instantaneous spectral index, rather than one averaged over time. The fitting has been performed using the SPEX package (Schwartz 1996; Smith et al. 2002). In total, 3 time intervals have been fitted: One at peak time, and one immediately before and after the peak time interval to compare the fittings and see whether they were plausible. For the later analysis only the spectrum at peak time has been used.

2.2.3 Spectral fitting

SPEX transforms a model photon spectrum into a model count spectrum via the spectral response matrix (SRM) and compares it to the observed count spectrum, iteratively adjusting the model parameters until a local minimum in χ^2 is found.

We used a spectral model that consisted of 2 isothermal components, each given by its temperature T_1 and T_2 as well as its emission measure EM_1 and EM_2 respectively, and a non-thermal component. The non-thermal component consists of a power-law with spectral index γ and flux F_{50} at normalization energy 50 keV, a low energy turnover at energy E_{turn} and a high-energy break at energy E_{br} . The power-law index above E_{br} is named β . The index below E_{turn} is fixed at 1.5. The model is illustrated in Fig. 2.1. It has 9 free parameters, but it was not always necessary to let all of them free. At first, an isothermal component (T_1 , EM_1) was fitted, followed by a power-law with a low-energy turnover (henceforth called 'standard model'). If the non-thermal spectrum showed indications of a break at high energies, the parameters E_{br} and β were also fitted. Some of the larger flares showed strong thermal emission that was fitted with an additional hotter isothermal component (T_2 , EM_2).

Table 2.1: Event list

No.	Date	Time	GOES ¹	GOES ² orig.	γ	F_{35} ³
1	22-Aug-02	01:52	M5.7	M5.9	3.4	$1.1 \cdot 10^1$
2	10-Jun-03	11:06	M5.2	M5.4	2.9	$1.7 \cdot 10^0$
3	20-May-02	10:52	M5.1	M5.3	3.6	$5.9 \cdot 10^{-1}$
4	20-Feb-02	09:58	M4.8	M4.9	3.6	$6.9 \cdot 10^{-1}$
5	15-Apr-02	00:10	M4.0	M4.1	5.8	$6.8 \cdot 10^{-1}$
6	18-Nov-03	08:08	M3.8	M3.9	2.6	$2.3 \cdot 10^0$
7	29-Sep-02	06:36	M3.0	M3.1	3.6	$3.5 \cdot 10^0$
8	13-Jun-03	02:01	M2.8	M3.1	6.9	$7.0 \cdot 10^{-1}$
9	16-Apr-02	13:10	M2.7	M2.8	6.5	$3.2 \cdot 10^{-1}$

¹ Background subtracted GOES-class

² Original GOES-class before background subtraction

³ units: photons s⁻¹cm⁻²keV⁻¹

Table 2.1: (continued)

No.	Date	Time	GOES ¹	GOES ² orig.	γ	F_{35} ³
10	06-Jul-02	03:32	M2.0	M2.1	5.8	$3.6 \cdot 10^{-1}$
11	27-Sep-02	13:08	M1.9	M2.0	3.3	$2.4 \cdot 10^{-1}$
12	20-Oct-02	00:41	M1.8	M1.9	5.3	$3.9 \cdot 10^{-1}$
13	10-Apr-02	19:02	M1.7	M1.8	2.9	$3.8 \cdot 10^0$
14	01-Jun-02	03:53	M1.5	M1.6	2.3	$2.8 \cdot 10^0$
15	21-Aug-02	01:39	M1.4	M1.6	2.7	$1.3 \cdot 10^1$
16	04-Apr-02	10:44	M1.3	M1.5	5.2	$2.6 \cdot 10^{-1}$
17	15-Apr-02	23:10	M1.2	M1.3	4.9	$6.6 \cdot 10^{-1}$
18	21-Feb-02	18:10	C9.9	M1.2	5.3	$4.5 \cdot 10^{-1}$
19	17-Apr-02	00:38	C9.9	M1.1	4.3	$2.5 \cdot 10^{-1}$
20	20-Feb-02	16:23	C9.3	M1.1	3.9	$1.6 \cdot 10^{-1}$
21	23-Aug-02	11:58	C8.4	M1.4	6.8	$1.9 \cdot 10^{-1}$
22	18-Jul-02	23:14	C7.9	C8.6	4.0	$1.0 \cdot 10^0$
23	30-Aug-02	02:40	C7.7	C8.9	4.2	$5.4 \cdot 10^{-1}$
24	24-Oct-02	18:05	C7.4	C7.8	3.0	$5.6 \cdot 10^{-1}$
25	20-Aug-02	22:28	C6.8	C8.4	3.5	$1.9 \cdot 10^0$
26	29-Aug-02	23:32	C6.2	C7.6	5.8	$1.9 \cdot 10^{-1}$
27	16-Sep-02	20:02	C4.6	C5.3	3.8	$2.1 \cdot 10^{-1}$
28	09-Apr-02	06:05	C4.2	C7.8	7.5	$2.0 \cdot 10^{-2}$
29	02-Apr-02	02:28	C3.9	C5.6	6.8	$2.4 \cdot 10^{-2}$
30	23-Aug-02	00:43	C3.6	C5.4	5.4	$1.5 \cdot 10^{-1}$
31	31-Aug-02	14:22	C3.2	C5.1	2.9	$9.8 \cdot 10^{-1}$
32	18-Sep-02	01:12	C2.9	C4.0	5.6	$2.2 \cdot 10^{-2}$
33	29-Aug-02	13:22	C2.8	C5.0	4.6	$3.5 \cdot 10^{-2}$
34	20-Jul-03	14:51	C2.6	C3.8	8.3	$1.4 \cdot 10^{-3}$
35	30-Aug-02	04:29	C2.2	C3.5	4.7	$2.0 \cdot 10^{-1}$
36	28-Feb-02	12:07	C2.0	C4.5	5.5	$3.6 \cdot 10^{-2}$
37	29-Nov-03	18:01	C2.0	C2.7	7.5	$6.8 \cdot 10^{-3}$
38	15-Nov-02	13:47	C1.7	C3.4	6.4	$2.6 \cdot 10^{-2}$
39	02-Oct-02	21:15	C1.4	C2.1	6.6	$9.5 \cdot 10^{-3}$
40	09-Sep-02	21:31	C1.3	C2.2	2.4	$5.0 \cdot 10^{-2}$

Table 2.1: (continued)

No.	Date	Time	GOES ¹	GOES ² orig.	γ	F_{35} ³
41	05-Apr-03	00:34	C1.3	C2.1	5.1	$1.4 \cdot 10^{-2}$
42	24-Feb-02	15:37	C1.1	C2.5	5.1	$1.1 \cdot 10^{-1}$
43	28-May-02	03:12	B8.8	C3.4	8.2	$2.6 \cdot 10^{-3}$
44	27-Nov-02	09:05	B8.7	C1.7	7.3	$9.6 \cdot 10^{-3}$
45	01-Dec-03	15:02	B7.7	C1.4	6.8	$4.7 \cdot 10^{-3}$
46	01-Jul-02	04:44	B5.8	C1.2	5.5	$6.0 \cdot 10^{-3}$
47	28-Mar-02	05:06	B5.4	C1.4	3.3	$2.3 \cdot 10^{-1}$
48	23-Sep-03	11:42	B4.4	B8.1	6.7	$2.8 \cdot 10^{-4}$
49	28-Nov-02	04:36	B3.8	C1.1	2.9	$7.7 \cdot 10^{-1}$
50	11-Aug-02	21:48	B3.6	C1.5	5.0	$6.3 \cdot 10^{-2}$
51	19-Jul-02	08:38	B3.3	C1.0	2.9	$6.3 \cdot 10^{-2}$
52	03-Aug-02	22:22	B3.0	C2.0	6.5	$1.5 \cdot 10^{-2}$
53	22-Apr-03	01:27	B3.0	B7.4	4.3	$2.3 \cdot 10^{-3}$
54	28-Jul-03	03:25	B2.9	B5.3	4.4	$4.9 \cdot 10^{-3}$
55	11-Jan-04	16:09	B2.7	B6.2	6.1	$8.4 \cdot 10^{-4}$
56	25-Oct-02	16:21	B2.5	B7.8	5.8	$2.6 \cdot 10^{-4}$
57	26-Nov-03	22:40	B2.5	B8.7	6.5	$6.9 \cdot 10^{-4}$
58	15-Dec-03	11:36	B2.5	B6.8	6.2	$4.6 \cdot 10^{-3}$
59	08-Mar-03	11:54	B2.3	B7.0	3.9	$6.3 \cdot 10^{-3}$
60	18-Mar-04	00:23	B2.3	B5.5	5.1	$5.3 \cdot 10^{-3}$
61	05-Mar-04	18:25	B2.2	B8.0	5.0	$1.7 \cdot 10^{-2}$
62	11-Apr-03	12:02	B2.0	B3.7	4.8	$8.4 \cdot 10^{-3}$
63	11-Apr-03	10:27	B2.0	B3.5	5.1	$5.5 \cdot 10^{-3}$
64	23-Nov-02	02:45	B1.7	B9.2	5.3	$2.2 \cdot 10^{-2}$
65	12-May-03	17:38	B1.3	B2.4	5.0	$9.7 \cdot 10^{-4}$
66	27-Sep-03	10:30	B1.2	B4.8	4.2	$6.4 \cdot 10^{-3}$
67	02-Dec-02	12:44	B1.1	B5.1	6.7	$3.3 \cdot 10^{-4}$
68	10-Jan-04	01:04	B1.1	B4.1	7.9	$9.1 \cdot 10^{-5}$
69	23-Mar-04	13:12	B1.0	B3.7	5.2	$1.1 \cdot 10^{-3}$
70	14-Apr-03	12:19	A9.7	B2.4	4.4	$8.9 \cdot 10^{-3}$
71	24-Feb-03	20:39	A9.3	B1.9	4.9	$3.3 \cdot 10^{-3}$

¹ Background subtracted GOES-class² Original GOES-class before background subtraction³ units: photons s⁻¹cm⁻²keV⁻¹

Table 2.1: (continued)

No.	Date	Time	GOES ¹	GOES ² orig.	γ	F_{35} ³
72	25-Feb-03	01:43	A9.3	B1.9	6.8	$1.8 \cdot 10^{-4}$
73	24-Feb-03	17:18	A8.5	B1.9	4.7	$2.2 \cdot 10^{-3}$
74	10-Mar-03	13:31	A7.2	B4.2	3.3	$8.9 \cdot 10^{-3}$
75	30-Mar-03	03:50	A6.9	B6.0	4.3	$1.1 \cdot 10^{-2}$
76	12-Apr-03	04:14	A5.6	B1.8	3.0	$3.7 \cdot 10^{-2}$
77	14-Apr-03	06:04	A5.0	B1.7	5.1	$2.0 \cdot 10^{-3}$
78	24-Dec-03	11:01	A4.6	B4.2	5.7	$1.8 \cdot 10^{-3}$
79	14-Apr-03	23:00	A4.4	B1.9	3.9	$3.4 \cdot 10^{-3}$
80	26-May-03	12:25	A4.3	B3.8	5.4	$2.8 \cdot 10^{-3}$
81	17-Apr-03	13:36	A4.2	B2.9	5.6	$1.2 \cdot 10^{-3}$
82	30-Jul-03	08:38	A3.8	B2.0	4.0	$3.7 \cdot 10^{-3}$
83	14-Mar-04	10:09	A2.8	B1.6	3.9	$4.4 \cdot 10^{-3}$
84	12-Apr-03	08:50	A2.8	B1.8	2.3	$2.8 \cdot 10^{-2}$
85	10-Apr-03	13:42	A2.5	B1.7	3.2	$1.1 \cdot 10^{-2}$
86	23-Sep-02	04:48	C1.3	C1.6		
87	09-Sep-02	16:32	B8.0	C2.2		
88	04-May-02	10:21	B4.4	C1.3		
89	17-Nov-02	07:18	B4.0	C1.7		
90	01-Mar-04	02:10	A1.4	B1.7		
91	29-Feb-04	20:09	A5.6	B2.5		
92	28-May-02	02:00	B5.2	C2.1		

All 92 flares are listed in Table 2.1 with a number, date, peak time, GOES flux, spectral index and non-thermal flux. In total, 6 different models were fitted:

1. One thermal part and an unbroken power-law (standard model): This provided the best fitting for 31 flares. Another 37 flares were fitted

¹ Background subtracted GOES-class

² Original GOES-class before background subtraction

³ units: photons s⁻¹cm⁻²keV⁻¹

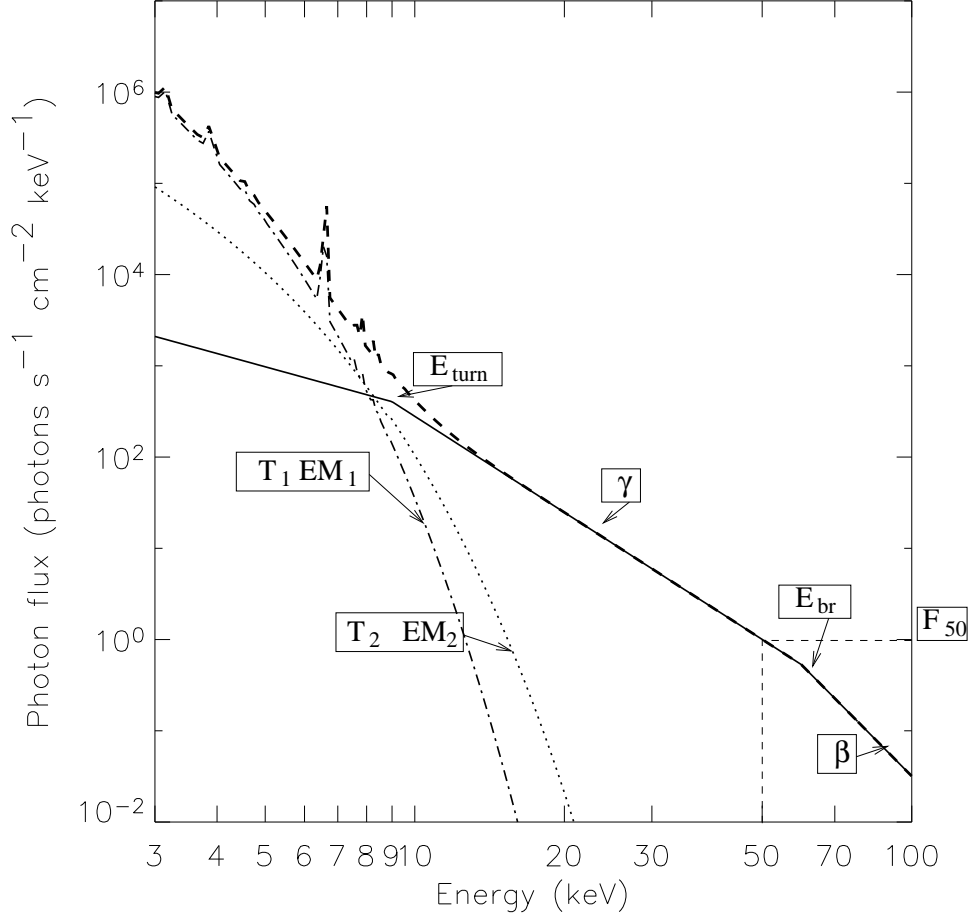


Figure 2.1: Illustration of the fitting model and the 9 free parameters discussed in the text. A non-thermal component (solid line) and two thermal components (dotted and dash-dotted) are shown.

with this model, but were also consistent with two thermal components and no power-law. This point will be discussed later.

2. One thermal part and a broken power-law: For 15 of the larger flares, a broken power-law fitting was applied. Most of these flares had emission beyond 50 keV, some up to 100 keV or more. Three of them can also be fitted with two thermal components.
3. Two thermal parts plus power-law: 2 flares had thermal emission up to around 20 keV which we fitted with two temperatures instead of one.
4. Only thermal: 6 flares show no indications for a power-law part in the

spectrum and were therefore fitted with one thermal part only (flare numbers 86–90 in Table 2.1) and with only two thermal components (no. 91). The largest of them was a C1.3 after background subtraction. These flares were not used in the further analysis.

5. Only broken power-law: Flare no. 92 (Table 2.1) was particularly difficult to fit. The best fitting was a broken power-law only. The spectrogram shows a very impulsive, short emission, even at the lowest energies. If present at all, the thermal emission must have been very small. This flare was not taken into the further analysis.

In conclusion, 85 out of 92 events could be fitted with the standard model or additionally with a break or a second isothermal component.

2.2.4 Flares with more than one fitting model

For many of the flares smaller than background subtracted GOES class C2, fitting a model with only 2 thermal components and no non-thermal emission was also possible. These smaller flares are less intensive than large flares. Therefore the non-thermal emission can be quite weak or even lie below the background level. As the signal-to-noise ratio decreases, different fittings are possible, but not necessarily plausible. The χ^2 of the two different models are often about the same value, making it impossible to determine which model is better. The temperatures range up to 260 MK in B-class flares. Although the thermal energy content would not be unphysically high, the standard model has been taken for each of those flares in the further analysis, as the analogy to large flares is the simplest assumption.

2.3 Results

We present here the results obtained from the fittings, comparing several flare properties to each other.

2.3.1 Non-thermal emission

Spectral index versus non-thermal photon flux

The non-thermal photon flux is modeled by a power-law distribution with spectral index γ . For events with a broken power-law, γ refers to the spectral index below the break energy. For the comparison of the spectral index and the

photon flux we cannot use the total flux above E_{turn} , $F_{\text{tot}} = \int_{E_{\text{turn}}}^{\infty} F(E) dE$, since this quantity depends strongly on E_{turn} which is poorly determined by the observations. Instead we use the flux at a reference energy E_0 . The maximum energy with still observable flare emission varies from about 20 keV to 300 keV, and increases with flare size. Therefore, choosing a high E_0 means extrapolating the flux of small flares into a range where it is not actually observed, whereas choosing a low E_0 means extrapolating the flux of large flares into a range where thermal emission might dominate. The influence of the choice of E_0 on the plot of γ vs. F_{E_0} is described in GB04. We chose $E_0=35$ keV as a typical energy for the presentation of the results. This allows also for comparisons with previous work.

The plot of γ vs. F_{35} for the examined 85 flares with a non-thermal component is shown in Fig. 2.2. Despite the large scatter of the data, a linear correlation in the double logarithmic plot is noticeable. A linear regression has been performed. As suggested by Isobe et al. (1990) for this kind of scattered data, the bisector regression method has been used. The relation can be written as a power-law model

$$\ln \gamma = \ln(A) - \alpha \ln F_{35}, \quad (2.3)$$

with statistical errors $\ln(A) = 1.11 \pm 0.06$ and $\alpha = 0.13 \pm 0.01$, or

$$\gamma = 3.0 F_{35}^{-0.13}. \quad (2.4)$$

Since the data have a fairly large scatter and there are less than 100 data points, it is difficult to determine unambiguously a single best regression model. The ordinary least squares regressions of y vs. x and x vs. y yield a limit for the confidence range of $\alpha = 0.13 \pm 0.07$.

As discussed in Sec. 2.2.4 there was more than one possible fitting model for most of the events smaller than C2 (after background subtraction). Therefore, the set has been divided into events smaller and larger than C2, and an independent regression has been made for both parts. The non-thermal flux of both sets ranges over 4 orders of magnitude and their spectral index ranges from 2.3 up to 8.3. The regression of the low GOES-class flares leads to a relation

$$\gamma = 2.04 F_{35}^{-0.16}, \quad (2.5)$$

with confidence range 0.16 ± 0.05 for the exponent. These flares are indicated with a triangle in Fig. 2.2. When taking only the events larger than C2, the relation becomes

$$\gamma = 3.60 F_{35}^{-0.16}, \quad (2.6)$$

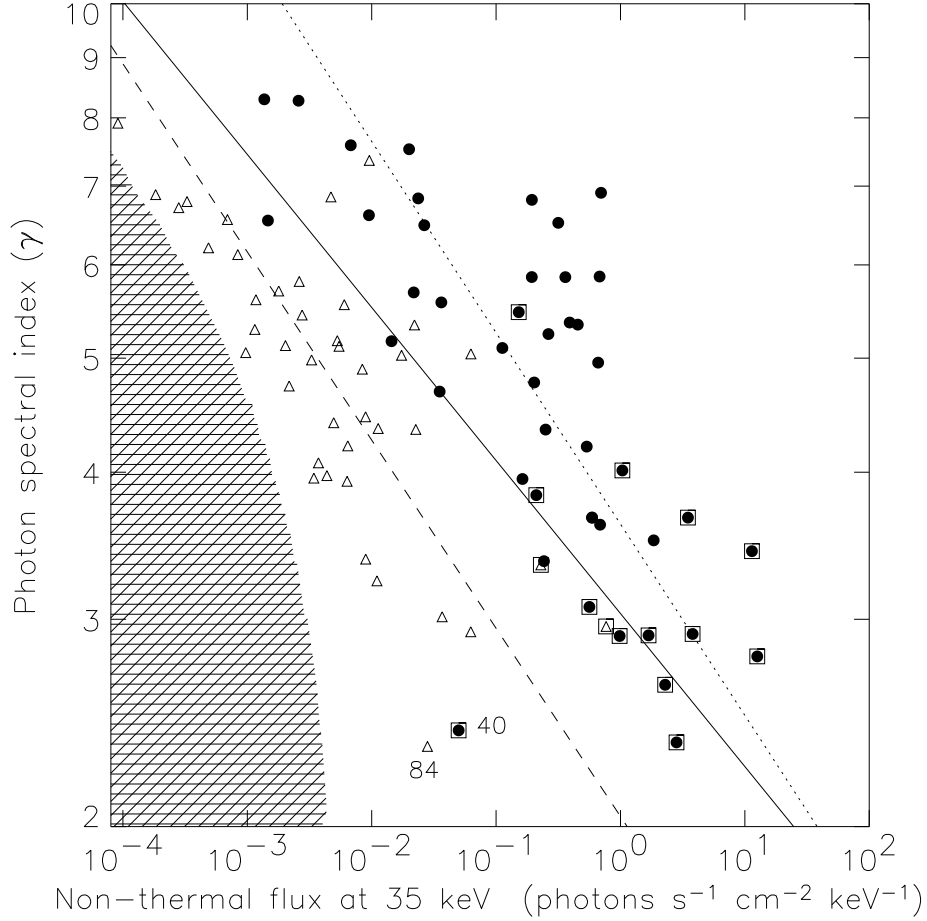


Figure 2.2: Spectral index γ versus RHESSI non-thermal photon flux at 35 keV, F_{35} . The solid line represents the linear bisector regression, given in Eq.(2.4). Flares with GOES class smaller than C2 are indicated with a triangle, those larger than C2 with a circle. The points outlined by a square are the events which were fitted with a broken power-law. The dotted line represents the regression for events larger than C2, and the dashed line represents the regression for events smaller than C2. Events in the shaded region would not appear in the flare list and would not be selected. The numbers refer to the event list in Table 2.1. These events are discussed in section 2.3.4.

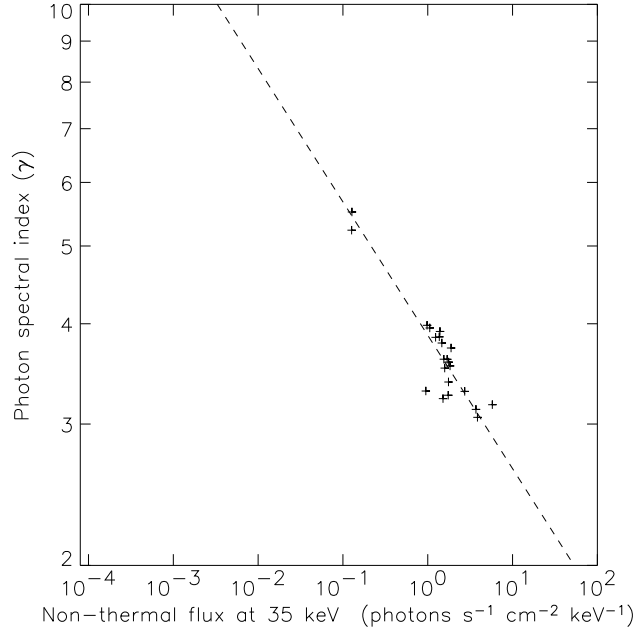


Figure 2.3: Spectral index (γ) versus non-thermal photon flux at 35 keV for several sub-peaks of a single flare. The dashed line represents the regression line (Eq. 2.7).

with confidence range 0.16 ± 0.06 for the exponent. Both sets of flares thus yield the same slope in logarithmic F_{35} vs. γ dependence. For the flares larger than C2 however, the regression line is shifted to higher F_{35} values by about one order of magnitude (compare Fig. 2.2). This leads to a flatter slope, when the regression is performed for the whole data set.

We are interested in the difference between small and large flares and whether their non-thermal parameters have something in common with the parameters of several sub-peaks of one single flare. Therefore, the same plot and regression has been made for sub-peaks of one of the flares that have been analyzed by GB04 (event no. 23 in their list, not present in our list). This plot is shown in Fig. 2.3. The relation is

$$\gamma = 3.89 F_{35}^{-0.17}, \quad (2.7)$$

and the confidence range for the exponent $\alpha = 0.17 \pm 0.01$. The relation between γ and F_{35} is quite similar for several peaks of one flare as for many flares of different size at time of maximum non-thermal emission. Note that the maximum non-thermal sub-peak flux of the inspected flare (GOES M4.9) ranges from 10^{-1} to 10^1 photons $\text{s}^{-1} \text{cm}^{-2} \text{keV}^{-1}$ and therefore represents only

a small section of the flux range of all flares in the presented sample. The observed power-law component (Eq. 2.7) is, however, very close to the relation for only events with GOES class larger than C2.

Observational limits

As mentioned in Sect. 2.2.1 there is a selection effect due to the nature of the flare list (only events with emission above background in the 12–25 keV band are listed). We made an estimate on how the γ vs. F_{35} relation is influenced by this selection effect.

The idea is to simulate count spectra and find limits for F_{35} and γ for which the total number of counts in the 12–25 keV energy range is larger than 3σ of the background. The spectral response matrix (SRM) without attenuators has been used. The average background in counts s^{-1} in the 12–25 keV energy band was estimated from the light curve. Photon spectra have been calculated, assuming a thermal component and an unbroken power-law. The temperature and emission measure were assumed according to the relations given in Eqs. (2.9) and (2.10). The low energy turnover was fixed at 9 keV. The photon spectra have been calculated for several values of spectral index γ from the interval [2,10] for a number of non-thermal fluxes F_{35} from the interval $[10^{-5}, 10^{-2}]$ photons $\text{s}^{-1} \text{cm}^{-2} \text{keV}^{-1}$. Each of these photon spectra has been multiplied by the SRM to get count spectra. For each flux F_{35} and spectral index γ in the above given intervals, the total number of counts in the energy range 12–25 keV has been calculated and compared to the background counts. For every F_{35} there exists a limit in γ where the total simulated counts are less than 3σ of the background counts. These boundaries plotted in the γ vs. F_{35} relation define a region (shaded region in Fig. 2.2) where events do not appear in the flare list.

From the location of the observational limits and the data points on the plot, one can expect the selection effect to be largest for soft events with a small non-thermal flux. If such events are missing in our selection, the regression line would be flatter in reality.

Energy of 'equal photon flux'?

As weaker flares are softer, there must be a region where spectra of weak and strong flares intersect. A 'pivot region' is sometimes found for the SHS evolution of single subpeaks (see Introduction). Similarly, an energy E_{eq} or an energy range may exist where small and large flares have equal non-thermal photon flux F_{eq} .

We have searched for an 'energy of equal photon flux' by calculating the energy distribution of all intersections between the non-thermal power-law fittings. The half width is extremely broad, ranging from 2.1 to 52 keV with a peak at 10.4 keV.

High-energy break

As mentioned before, 15 spectra have been fitted with a high-energy break. These events are indicated with a square in Fig. 2.2. The non-thermal flux F_{35} of all these events is higher than $4 \cdot 10^{-2}$ photons $\text{s}^{-1}\text{cm}^{-2}\text{keV}^{-1}$. Thus high-energy breaks are observed only in large flares.

The break energy does not correlate with the spectral index. However a correlation appears between the spectral index below break energy (γ) and the spectral index above break energy (β) following a relation $\beta = (1.96 \pm 0.20)\gamma - 1.59$. A similar relation has previously been reported by Lin & Schwartz (1987). Further, we observed a correlation between the break energy and the non-thermal photon flux at 35 keV, indicating that flares with smaller non-thermal flux have on the average a lower break energy. Such a comparison has previously been made by Dulk et al. (1992), who found no correlation between break energy and non-thermal flux.

However, we were not able to exclude without doubt selection effects that could lead to these correlations (see also discussion in Sect. 2.4).

2.3.2 Thermal flare properties compared to non-thermal properties

In a next step the soft X-ray flux observed by the GOES satellites was included in the analysis. The GOES flux of all flares at time of maximum emission (GOES peak time) in the 1–8 Å band has been extracted. For a proper analysis, the background was subtracted. The background was chosen in GOES light curves as either linearly interpolated between pre-flare and post-flare background or as constant. Subtracting background changes the GOES class contrary to the usual classification. When referring to the size of a flare, the GOES class according to peak flux without background subtraction is given throughout this work. For comparing physical parameters, however, the background-subtracted values have been used.

First, the non-thermal flux F_{35} has been compared to the maximum GOES flux, F_G . There is a linear correlation in a double logarithmic plot, presented in Fig. 2.4, giving:

$$F_G = 1.8 \cdot 10^{-5} F_{35}^{0.83}, \quad (2.8)$$

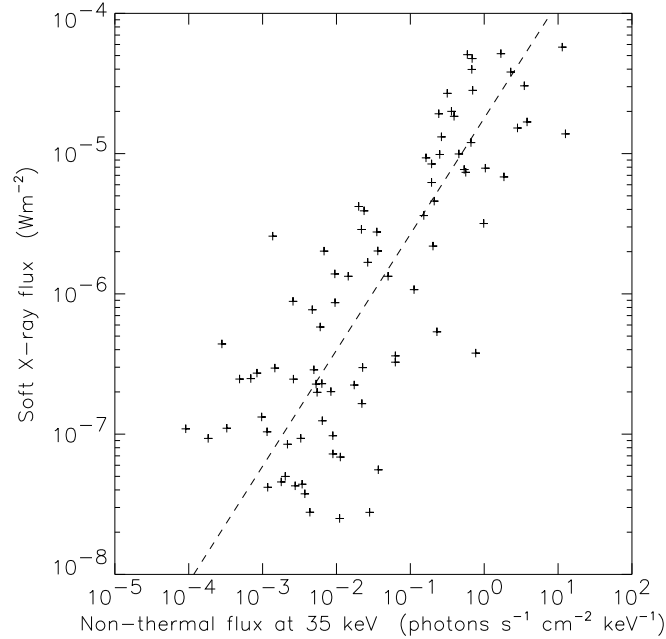


Figure 2.4: Soft X-ray flux F_G versus non-thermal flux F_{35} at 35 keV with regression line, as given in Eq. (2.8).

where the exponent $b = 0.83 \pm 0.19$. F_G is in units of Wm^{-2} and F_{35} in $\text{photons s}^{-1}\text{cm}^{-2}\text{keV}^{-1}$.

As F_{35} vs. γ and F_{35} vs. F_G correlate, one must expect a correlation between F_G and γ . Figure 2.5 illustrates that this is not the case. From the relations $\gamma = AF_{35}^\alpha$ and $F_G = CF_{35}^d$ one can calculate an expected relation $\gamma = AC^{-\alpha/d}F_G^{\alpha/d}$, giving $\gamma = 0.53F_G^{-0.16}$, represented by the dashed line. As expected, the flares with small F_{35} are in the upper left corner and the ones with large F_{35} in the bottom right. However, the scatter in γ is so large that the correlation is statistically not significant.

We compared also the temperature T_1 and emission measure EM_1 of the thermal plasma derived from RHESSI data, to the non-thermal X-ray flux at 35 keV. Figure 2.6 indicates a correlation between temperature and non-thermal flux with a relation

$$T_1 = 1.46 \ln F_{35} + 21.57, \quad (2.9)$$

where T_1 is in units of 10^6 K and F_{35} in $\text{photons s}^{-1}\text{cm}^{-2}\text{keV}^{-1}$.

A higher non-thermal flux is therefore associated with a higher temperature. A similar observation holds for the relation between F_{35} and the emission

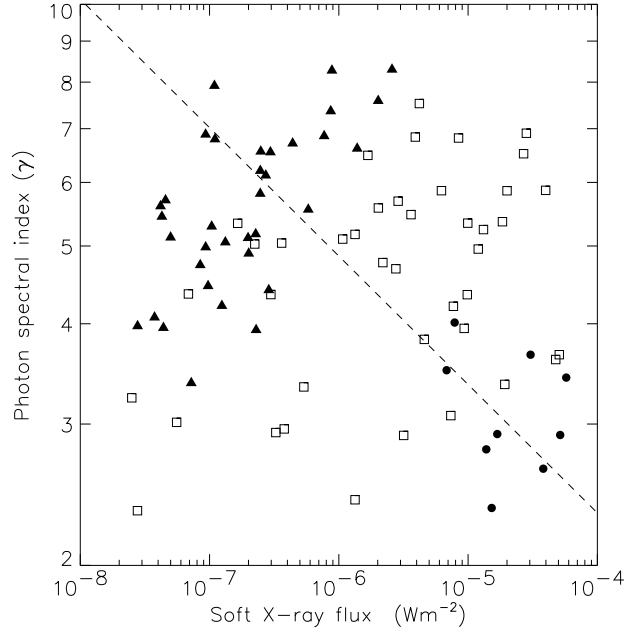


Figure 2.5: Spectral index γ versus soft X-ray flux F_G . The data points have been labeled with 3 different symbols according to 3 flux intervals in F_{35} (units: photons $\text{s}^{-1}\text{cm}^{-2}\text{keV}^{-1}$). Triangles: F_{35} in the interval $[10^{-5}, 10^{-2}]$; squares: F_{35} in the interval $[10^{-2}, 10^0]$; circles: F_{35} in the interval $[10^0, 10^2]$. The dashed line is the expected trend-line from the correlations of γ vs. F_{35} , and F_G vs. F_{35} .

measure (Fig. 2.7).

$$EM_1 = 5 \cdot 10^{48} F_{35}^{0.91}, \quad (2.10)$$

with EM_1 in cm^{-3} .

2.3.3 Thermal flare plasma

Similar to the investigations by Feldman et al. (1996), we also compared the temperature T_1 at hard X-ray peak time to the maximum soft X-ray flux F_G . We note a correlation in Fig. 2.8, giving

$$F_G = 3.5 \cdot 10^{0.33T_1 - 12}, \quad (2.11)$$

where F_G is in Wm^{-2} , plotted in a logarithmic scale, and T_1 is in units of 10^6 K, plotted in linear scale. Due to the large scatter, the power factor p in Eq. (2.11) has a confidence range of $p = 0.33 \pm 0.29$. The Feldman et al. result

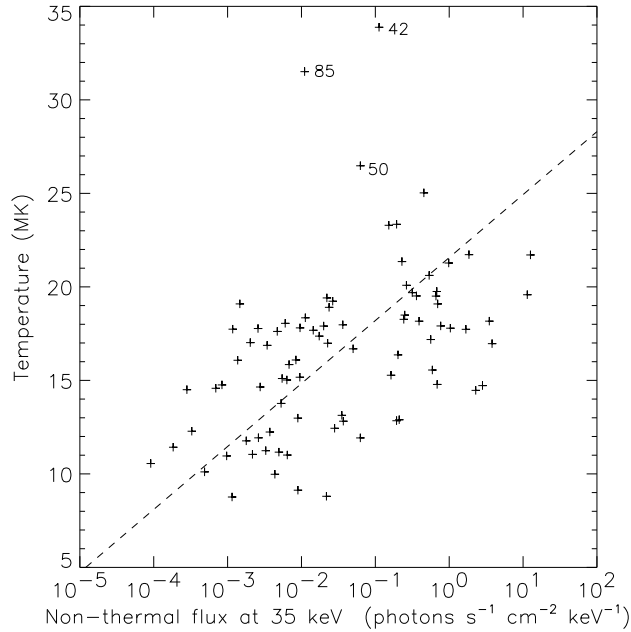


Figure 2.6: RHESSI temperature T_1 versus non-thermal flux at 35 keV with linear bisector regression line (Eq. 2.9). The numbers refer to the event list in Table 2.1.

($F(T) = 3.5 \cdot 10^{0.185T-9.0}$) differs considerably, as is illustrated in Fig. 2.8. It is though still within the estimated range for the regression parameters. Contrary to Feldman et al., we used background subtracted GOES flux. The background-subtraction from the GOES data has the biggest influence on the smaller flares, altering the flux to smaller values and extending the flux range one order of magnitude. Using the original, not background subtracted GOES data, we get $F_G = 1.7 \cdot 10^{0.25T_1-10}$.

Comparison of temperatures

From the flux ratio in the 2 GOES wavelength bands, one can calculate an isothermal temperature T_G at the time of maximum soft X-ray flux, using Mewe spectral models (Mewe et al. 1985). As the minimum energies of the two bands are 1.5 keV and 3.1 keV respectively, GOES measurements are dominated by photons at lower energy than used to determine the temperature from RHESSI data (≥ 4 keV). A comparison of the two measurements is also a check on the applied methods: flux ratio (GOES, at soft X-ray peak time) versus spectral fitting (RHESSI, at hard X-ray peak time). Figure 2.9 indicates that the temperature derived from RHESSI data is often higher. A

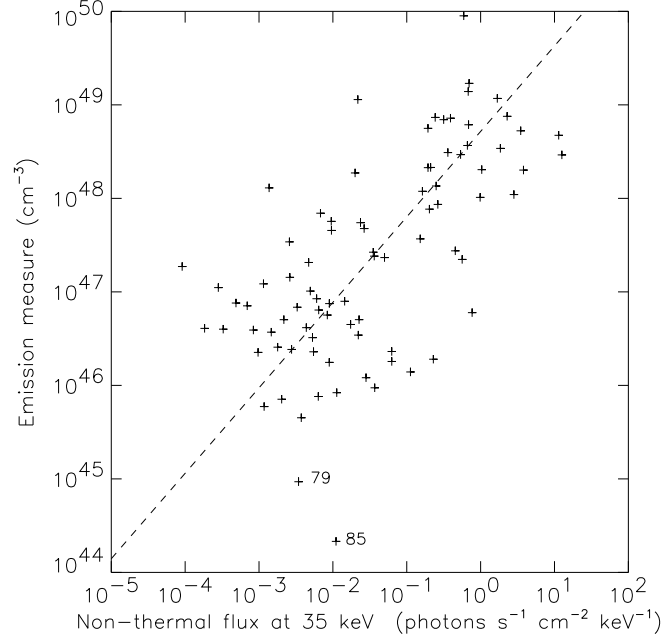


Figure 2.7: Emission measure EM_1 versus non-thermal flux at 35 keV. The dashed line indicates the linear bisector regression line (Eq. 2.10). The numbers refer to the event list in Table 2.1.

linear bisector regression yields a relation $T_1 = 1.31T_G + 1.47$ (in MK), but is influenced by the three outliers. Without the outliers, the relation would be $T_1 = 1.12T_G + 3.12$.

The emission measure derived from the GOES data is higher than that from the RHESSI data for 82 out of 85 events. The ratio EM_1/EM_G increases for larger events. On the average, $EM_1 \approx 0.1EM_G$. Most likely, the RHESSI measurements emphasize the hotter part of a non-isothermal temperature distribution in the soft X-ray source. Part of these trends could also be accounted for by the different times of measurements, as the hard X-ray peak usually occurs earlier in the course of a flare than the soft X-ray peak. Taking the GOES temperature at the same time as the RHESSI temperature leads indeed to a relation with less pronounced trend: $T_1 = 1.13T_G + 3.17$, but the RHESSI temperature is still higher than the GOES temperature in most cases (Fig. 2.9).

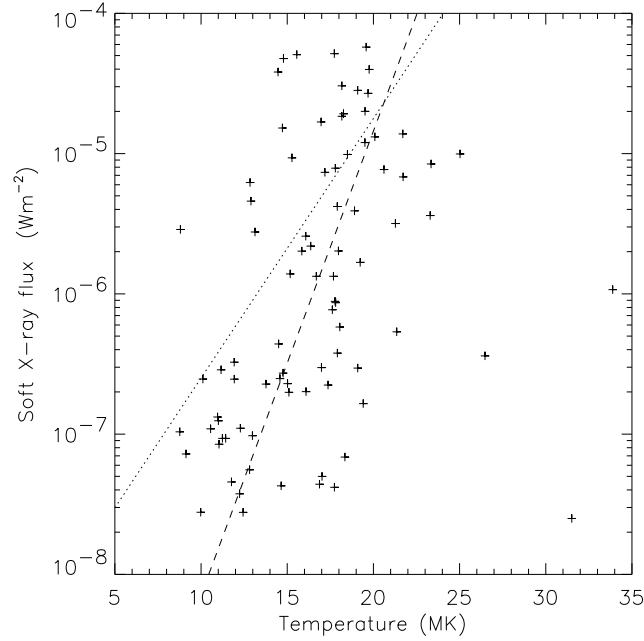


Figure 2.8: Maximum soft X-ray flux versus temperature. The dashed line gives the linear bisector regression to the data (Eq. 2.11). The dotted line is the trend line calculated from the Feldman et al. result (Eq. 2.1).

2.3.4 Inspection of exceptional flares

In most of the presented plots there are a few events far from the overall trend line. The most striking ones have been numbered according to Table 2.1 and are shortly discussed here.

No. 40 and 84 have very hard spectral indices, no. 84 has the hardest γ in our data set. Its spectrogram shows short, impulsive emission up to over 30 keV.

No. 42, 50 and 85 have very high temperatures. The spectrograms of all three events indicate a very short, impulsive, non-thermal peak with emission over 30 keV.

No. 79 has a small emission measure of only $9.3 \cdot 10^{44} \text{ cm}^{-3}$. The temperature of 16.9 MK is rather high for a flare of this size. Again, the flare is very short and impulsive.

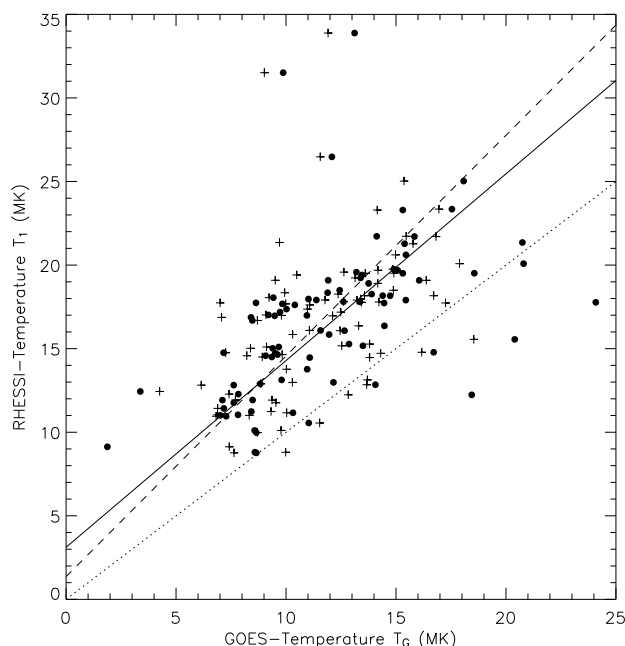


Figure 2.9: Temperature measured by RHESSI (T_1) compared to GOES temperature (T_G). The dotted line indicates the diagonal line. Crosses indicate the GOES temperature at GOES peak time, the dashed line gives the corresponding regression line. Dots give the GOES temperature measured at the same time as the RHESSI temperature with the solid line as regression line.

The common characteristic of all these flares is the short duration of the non-thermal emission.

2.4 Discussion

The high spectral resolution of RHESSI's germanium detectors permits the separation of a non-thermal and one or two thermal components in most X-ray spectra of solar flares over a large range of flare sizes. The selection was made according to the usual definition of flare size in terms of peak soft X-ray flux (labeled B1 to M6) as measured by the GOES 1 - 8 Å channel. It remains nearly uniform in soft X-ray peak flux after background subtraction but extends one more order of magnitude to smaller flares (A1 to M6).

The analysis of the non-thermal emission shows a clear relation between the spectral index γ and the power-law normalization F_{35} at peak time. The correlation between γ and F_{35} can be expressed by a power-law. We note

that the quantitative relation is not identical to the relation found for the SHS behavior in subpeaks of events. The spectral index γ depends less on F_{35} , and the power-law exponent α is smaller (Eq. 2.4). The two exponents α for the temporal evolution of single flares and the peak values of many flares can be brought closer together when we accept that the flares smaller in soft X-rays (and GOES class) are generally deficient in F_{35} , relative to the F_{35} vs. γ relation found by GB04. Soft events with small hard X-ray flux are missing by selection. This could lead to a flatter relation in reality.

Further, it may well be possible that the power-law relation does not hold below $F_{35} \approx 10^{-5}$ photons $\text{s}^{-1} \text{cm}^{-2} \text{keV}^{-1}$, but flattens toward a constant value of γ .

The selection according to thermal flare properties aims also at a large range of non-thermal X-ray fluxes. They range from 10^{-4} to 10 photons $\text{s}^{-1} \text{cm}^{-2} \text{keV}^{-1}$ at 35 keV (F_{35} , see Fig. 2.2), with a relatively uniform distribution between 10^{-3} and 1 photons $\text{s}^{-1} \text{cm}^{-2} \text{keV}^{-1}$. The non-thermal flux distribution depends on the reference energy. At lower reference energy, in the range of the 'equal photon flux', the distribution becomes narrower.

A selection effect comes in when the comparison includes parameters of the thermal plasma, since among small flares events with high non-thermal flux have been preferentially selected. The relations shown in Figs. 2.4 and 2.5 may be affected by selection. In Fig. 2.4 small soft X-ray events with low F_{35} are missing, particularly in the interval $[10^{-5}, 10^{-3}] F_{35}$ and $[10^{-8}, 10^{-7}] F_G$. Thus the regression line may be slightly flatter and the exponent in Eq. (2.8) smaller. The trend for larger scatter in F_{35} for smaller flares may thus be even larger than visible in Fig. 2.4. In Fig. 2.5 small soft X-ray events with large γ (upper left corner) are missing. This may contribute to the absence of significant correlation between γ and soft X-ray flux. Note, however, that the three intervals of non-thermal flux line up along the expected correlation line with a large scatter below and above the line. Nevertheless, it remains a fact that one cannot predict the spectral index at peak non-thermal emission from the soft X-ray flux.

Different selection effects have already been mentioned in relation with the break energy of the non-thermal spectrum at high energies, visible only in large flares (high F_{35}) and low γ . We further note that using the spectral index above the break energy, β and its corresponding flux normalization at 35 keV worsens the correlation.

It may be added here also that the low-energy turnover E_{turn} seemingly correlates with F_{35} and even better with F_G . The latter and the fact that E_{turn} is usually close to the energy with equal thermal and non-thermal contributions

strongly point to a spurious effect (see also Saint-Hilaire & Benz Saint-Hilaire & Benz (2005)). It does not influence significantly the relations discussed above.

The temperature changes only slightly (from about 5 MK to 30 MK) over 4 magnitudes of F_{GOES} but there is a linear dependence between F_{GOES} and EM_1 . Therefore, the similarity of Figs. 5 and 8 is not surprising. In fact, the two exponents in Eqs. (2.8) and (2.10) are identical within the statistical uncertainty. However, it is surprising that the correlation does not improve from F_{G} vs. F_{35} to EM_1 vs. F_{35} , as EM_1 is determined simultaneously and at the peak of F_{35} and does not contain the temperature, whereas F_{G} is determined at the peak of the soft X-ray emission later in the flare. F_{G} correlates well with EM_1

$$F_{\text{G}} = 3.6 \cdot 10^{-50} EM_1^{0.92}, \quad (2.12)$$

with EM_1 in cm^{-3} and F_{G} in Wm^{-2} , and $b = 0.92 \pm 0.09$. The exponent b is not significantly below unity. Such a trend may arise from the reduced efficiency for thermal emission at high temperatures of large flares, or may be due to larger energy losses because of longer duration.

The correlation between the temperature and soft X-ray emission of the thermal plasma (Fig. 2.8) is steeper than previously reported by Feldman et al. (1996) see Eq. (2.1)). Part of the difference can be accounted for by our subtraction of the background, increasing the range of peak fluxes. On the other hand, Feldman et al. used temperatures from the Yohkoh BCS detectors. These detectors saturate at high fluxes. Therefore the correlation found by Feldman et al. may be even flatter. As already mentioned in Sect. 2.3.3 RHESSI might measure the hotter part of a non-isothermal plasma, whereas GOES sees a cooler part.

Finally, none of the investigations on the flare position on the disk showed a significant effect. The distributions of γ , F_{35} , and E_{br} are independent of radial distance from the center of the disk. Events with position offset larger than 950 arcsec from the sun center have been looked at separately. They show no significant pattern on the γ vs. F_{35} plot. This excludes an influence of the varying albedo of the X-ray emission scattered by the chromosphere on the above results.

2.5 Summary and Conclusions

Flares observed by RHESSI were selected from a wide range of GOES flare size. The selection was nearly uniform from B1 to M6 (corresponding to flares

between A1 to M6 after background subtraction). Out of 92 flares with a well defined spectrum at peak time, 85 events can be fitted by a thermal and a non-thermal component. Only 6 events (7%) had only thermal emission, one had only a non-thermal component. The fitted flux at 35 keV at the peak time of the non-thermal emission in 85 flares ranges over more than 5 orders of magnitude (Fig. 2.2). This greatly exceeds the range that has been analyzed in the temporal SHS evolution of a single subpeak (Fig. 2.3) and even in all combined subpeaks in the literature (GB04). A power-law index could be reliably determined from a minimum value of 2.3 up to a maximum of 8.3.

The main conclusion based on this study is that the spectral index γ at peak non-thermal emission of flares, as well as at subpeaks of a single flare correlate. Thus flares with small non-thermal flux are softer on the average. This makes them even more difficult to detect in high-energy X-ray emission. Eventually, the non-thermal emission becomes indistinguishable from thermal emission, although it represents possibly a larger amount of energy.

We have studied further the relations between non-thermal flux, spectral index, soft X-ray flux, temperature, and emission measure with the following results:

- The spectral index, γ , and the peak non-thermal flux at 35 keV, F_{35} , correlate linearly in a double logarithmic plot, similar to the time evolution of γ and F_{35} during one single flare or subpeak.
- Small soft X-ray emitting flares have a lower F_{35} by nearly an order of magnitude from the relation derived earlier. They also show a larger spread in F_{35} .
- Soft X-ray flux and non-thermal flux at 35 keV are correlated, indicating that flares with larger non-thermal emission have larger thermal emission.
- Although soft X-ray flux and non-thermal flux are correlated, as well as spectral index and non-thermal flux, there is no significant correlation between spectral index and soft X-ray flux (GOES class). Probable reasons are the large scatter in γ and a selection effect.
- Temperature and emission measure of the thermal plasma both correlate with non-thermal flux, indicating that flares with large non-thermal flux have a higher temperature and emission measure.
- A comparison of soft X-ray flux and temperature yields a correlation also seen in previous work, but with slightly different relation due partially to background subtraction.

That the temperature is higher in large flares is the property of the thermal flare plasma, thought to be heated by precipitating particles, thus a secondary product of energy release. It may be explained by the repeated impact of electrons accelerated in elementary flares, the larger the flare, the more such impacts and the hotter the target. The γ vs. F_{35} relation, however, concerns the non-thermal electron population thought to be a primary flare product. As it applies to different flares and not only to the temporal evolution in a flare, it cannot be a secondary phenomenon. Thus it is an intrinsic feature of the acceleration process. Its quantitative relation must be accounted for by a realistic acceleration theory.

Lower F_{35} being associated with larger γ affect the frequency distribution of flare energies. If the energy or peak flux of non-thermal electrons is determined well above the mean energy of 'equal photon flux' (10.4 keV), flares with low non-thermal flux are lost in the background. For RHESSI observations, this affects the selection for GOES classes smaller than about C2 (Fig. 2.2). The frequencies of hard X-ray flares are reported to have power-law distributions (eg. Hudson 1991). If soft small flares have been missed, the published power-law indices must be considered as lower limits.

Chapter 3

Relations between concurrent hard X-ray sources in solar flares *

M. Battaglia¹ and A. O. Benz¹

Abstract

Context. Solar flares release a large fraction of their energy into non-thermal electrons, but it is not clear where and how. Bremsstrahlung X-rays are observed from the corona and chromosphere.

Aims. We aim to characterize the acceleration process by the coronal source and its leakage toward the footpoints in the chromosphere. The relations between the sources reflect the geometry and constrict the configuration of the flare.

Methods. We studied solar flares of GOES class larger than M1 with three or more hard X-ray sources observed simultaneously in the course of the flare. The events were observed with the X-ray satellite RHESSI from February 2002 until July 2005. We used imaging spectroscopy methods to determine the spectral evolution of each source in each event. The images of all of the five events show two sources visible only at high energies (footpoints) and one source only visible at low energies (coronal or looptop source, in two cases situated over the limb).

Results. We find soft-hard-soft behavior in both, coronal source and footpoints. The coronal source is nearly always softer than the footpoints. The footpoint spectra differ significantly only in one event out of five.

Conclusions. The observations are consistent with acceleration in the coronal source and an intricate connection between the corona and chromosphere.

* This chapter is published in *Astronomy & Astrophysics* **456**, 751 (2006)

¹ Institute of Astronomy, ETH Zurich, CH-8092 Zurich, Switzerland

3.1 Introduction

The current understanding of solar flares leaves open fundamental questions such as: where is flare energy released, how are particles accelerated? A large part of the energy released in a solar flare is converted into energetic electrons emitting hard X-rays. Therefore, observations in X-ray wavelengths give quantitative measures of heating and particle acceleration in the flare. X-ray observations by Hoyng et al. (1981) showed hard X-ray (HXR) sources at both ends of a loop structure, commonly called footpoints. They are thick target bremsstrahlung emission produced by precipitating electrons, accelerated somewhere in the loop. Footpoints can also be seen in $H\alpha$ and EUV (eg. Gallagher et al. 2000; Fletcher et al. 2004), indicating the precipitation of flare particles and the reaction of the thermal plasma. In an event observed by *Yohkoh*, Masuda et al. (1994) first noted a third HXR source situated above the looptop (looptop or coronal source). Alexander & Metcalf (1997) analyzed this event carefully, concluding that the loop top source can be best described by a thermal component and a non-thermal component which is harder than the footpoint spectrum. Petrosian et al. (2002) made an extended study of looptop sources and footpoints in *Yohkoh*-events. They find that the spectral index of the looptop source is softer than the footpoints on the average by about 1. The accuracy of their spectra however, was limited by the energy resolution of the *Yohkoh* detectors.

An important observation about the time behavior of the HXR flux has already been made in the late 1960s by Parks & Winckler (1969) and Kane & Anderson (1970). They found that the hardness of a spectrum changes in time and that there exists a correlation between the HXR flux and the hardness of the spectrum (soft-hard-soft or SHS). These observations were later confirmed by several authors, (eg. Benz 1977; Brown & Loran 1985; Lin & Schwartz 1987; Fletcher & Hudson 2002; Hudson & Fárník 2002). Beside the SHS pattern, a soft-hard-harder (SHH) pattern has also been observed in some events (Frost & Dennis 1971; Cliver et al. 1986; Kiplinger 1995). A quantitative study of 24 solar flares observed by RHESSI on this subject has been made by Grigis & Benz (2004). They find that elementary flare bursts also show SHS. Battaglia et al. (2005) made a study of flares of different size, finding that events with smaller HXR flux are softer on the average and that the relation between HXR flux and spectral index at peak time of events of different size is the same as the one from several peaks of one event.

Is the SHS-behavior a feature of the acceleration mechanism as previously claimed? Or is it a transport effect produced by collisions or return

currents? A further possibility could be a change in the dominating X-ray source from the coronal source (soft) to the footpoints (hard) and back to the coronal source again (soft). Thus, is the SHS-behavior nothing but a coronal-footpoint-coronal effect? The previous studies have been made using full sun spectra. To investigate the cause of the SHS, the spectra of each source must be analyzed separately. The Ramaty High Energy Solar Spectroscopic Imager (RHESSI Lin et al. 2002) provides the possibility of making high resolution imaging spectroscopy at different locations on the sun. One can therefore study each source separately in events with several contemporaneous HXR-sources. The high energy resolution yields detailed spectra, allowing a reliable differentiation between thermal and non-thermal emission. Emslie et al. (2003) made an analysis of a very large event with 4 HXR-sources observed by RHESSI. They find a coronal source with a strong thermal component and two (at times three) footpoints in regions with opposite magnetic polarity. They report that the spectral indices of the footpoints differ notably and accredit this to collisional losses by different column densities in the loop connecting the footpoints to the coronal source.

The purpose of this work is a systematic study of the relation between coronal source and footpoints in time and spectra for several well observed events. The events were carefully selected, not necessarily the largest ones, but those with informative data concerning both, thermal and non-thermal source parameters. The RHESSI data has been searched for well separated, bright events without strong pileup, situated near the limb. We present here the results for the best observed events of the first 40 months since launch.

3.2 Observations, Event Selection and Spectroscopy

The X-ray satellite RHESSI has been observing the full sun since February 2002. Modulation of the X-ray flux by rotating grids provides image information for any region on the sun (Hurford et al. 2002). High resolution germanium detectors (energy resolution ~ 1 keV) allow detailed studies of X-ray flare-spectra (Smith et al. 2002). In Sect. 3.2.1 we describe how events were selected. The image processing and spectral analysis methods are presented in Sect. 3.2.2 along with some investigations of the best choice of imaging algorithm, source regions etc.

Table 3.1: List of analyzed events. The times give the range during which the analysis was made (times with strong emission from all three sources).

Date	Time	GOES class
4-Dec-2002	22:42-22:53	M2.7
24-Oct-2003	02:42-03:00	M7.7
1-Nov-2003	22:24-22:40	M3.3
13-Jul-2005	14:12-14:25	M5.1
30-Jul-2005	06:28-06:36	X1.3

3.2.1 Event selection

The selection was made using imaging spectroscopy quicklooks provided by the RHESSI Experimental Data Center (HEDC Saint-Hilaire et al. 2002). Events are required to have 3 sources observed simultaneously during at least 1 minute in the course of the flare. The sources may not all be visible in the same image of a particular energy range. The search was restricted to events larger than GOES class M1 in order to have large enough count rates. Further, the three sources ought to be well separated to avoid contamination of spectra in imaging spectroscopy by other sources. For this reason, we required a minimum offset of 700 arcsec from sun center to exclude events with projection of the coronal source onto the footpoints. Events with strong particle precipitation and detector livetime (uncorrected monitor rates) below 90% were discarded. This lead to a final sample of 5 flares. Table 3.1 gives an overview of the selected events.

Images of the events at 34-38 keV (representative for emission by non-thermal electrons) are presented in Fig. 3.1. The 60 and 80 % contours at energies 10-12 keV (dominated by thermal emission) are overplotted. The regions of interest for the spectrum calculation are given in grey. The fragmented shape of the coronal source of the Oct. 24th 2003 event can be partly accounted for by over-resolution, as the source is slightly more compact in images without detector 3.

3.2.2 Imaging spectroscopy

In this section we discuss some technical aspects of the analysis concerning imaging spectroscopy as well as some issues that have to be considered like

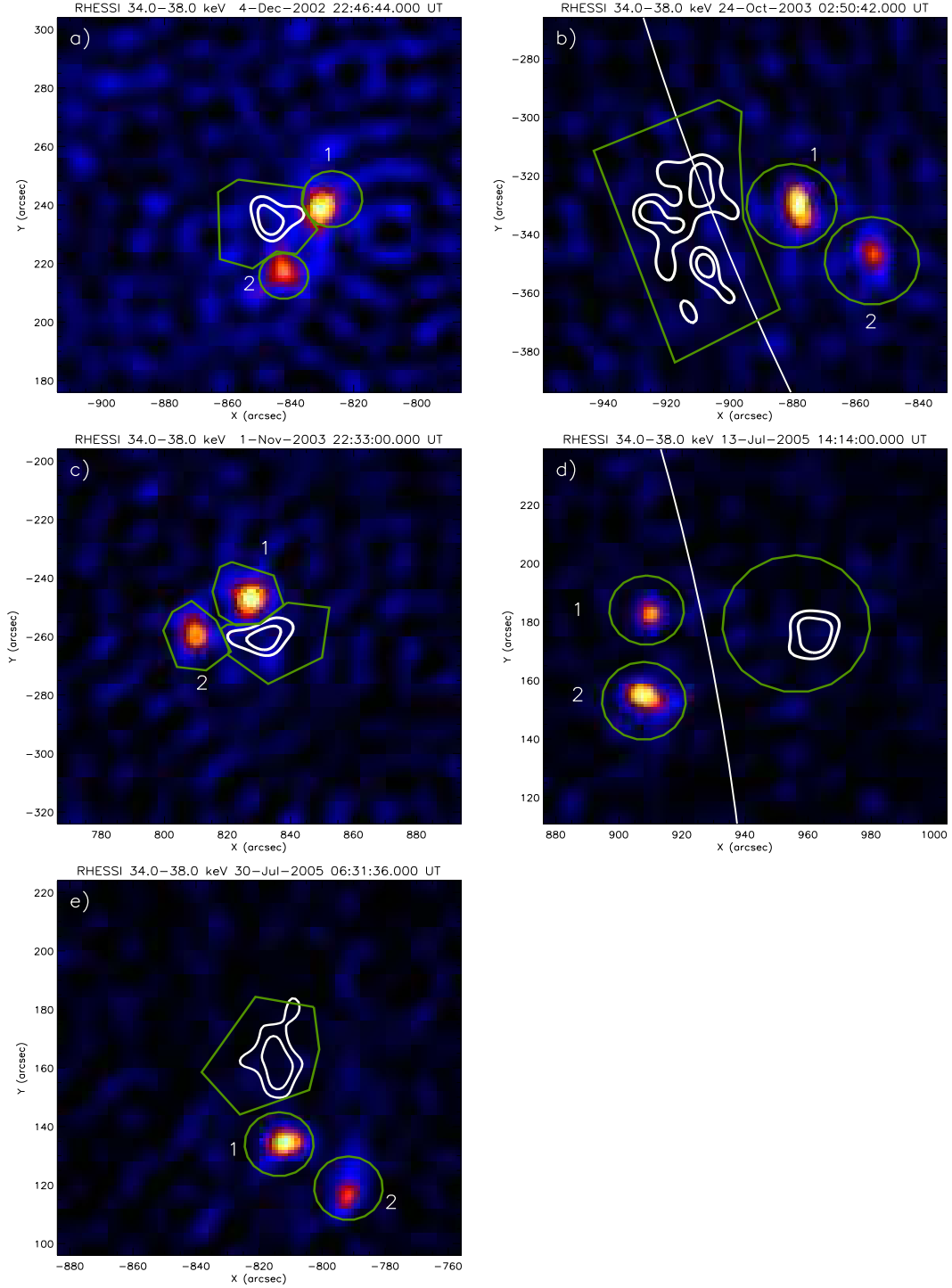


Figure 3.1: Clean images (using detectors 3-8) of each event in the 34-38 keV energy range. The 60 and 80 % contours at energies 10-12 keV (white) and the regions of interest (grey) are given. The footpoints have been arbitrarily numbered (1 & 2). The solar limb is indicated where in the field of view.

source separation and pileup.

Imaging algorithm

Clean, Forward-Fitting and Pixon algorithms (Hurford et al. 2002) have been tested for image reconstruction. Clean was used for the actual imaging spectroscopy for the following reasons. Forward-Fitting works fine as long as the sources in an image are equally strong, but has difficulties as soon as there are background regions that are almost as strong as a source. With the defined time and energy bins for imaging spectroscopy, this frequently occurs in high or the lowest energy bands, at any time interval, in which case Forward-Fitting produces spurious results. Pixon yields generally a better spatial separation of the sources than Clean. However, it needs more fine-tuning of the input imaging parameters to be as stable as Clean for low signal to noise ratios. In an extended series of tests, Clean turned out to be the most efficient and reliable algorithm for the automatic image generation of long time series for imaging spectroscopy.

Therefore, the Clean algorithm was applied, using detectors 3-8. Detector 2 over-resolves the sources, just increasing noise. The angular resolution without detector 3 becomes too small to separate the sources properly for all events except the one of July 13th 2005. The time bins were chosen from 12 s to 120 s, depending on the source intensities, to get good images and enough counts for reliable spectra. A pseudo-logarithmic energy binning was used.

Computation of spectra

The imaging spectroscopy tools implemented in OSPEX (a further development of SPEX (Schwartz 1996; Smith et al. 2002) have been used for the determination of the regions of interest (ROI) and for the calculation of the spectra. ROIs can be delimited by polygons or circles around the sources, as selected by the user. Ideally, one would select a ROI as contour in percentage of the maximum of a source. As sources move in time and often have different sizes in different energy-bands, this could not be done reasonably. Therefore, ROIs were selected as circles or polygons in each time interval, having the same size in all energies. The ROIs for the footpoints were defined at energies larger than 40 keV such as to include all of the source emission. The ROIs of the coronal source was selected at an energy around 10 keV likewise. The effects of this method of ROI selection are discussed in the last paragraph of this section and shown in Fig. 3.3.

The attained spectra were fitted with a non-thermal power law at high

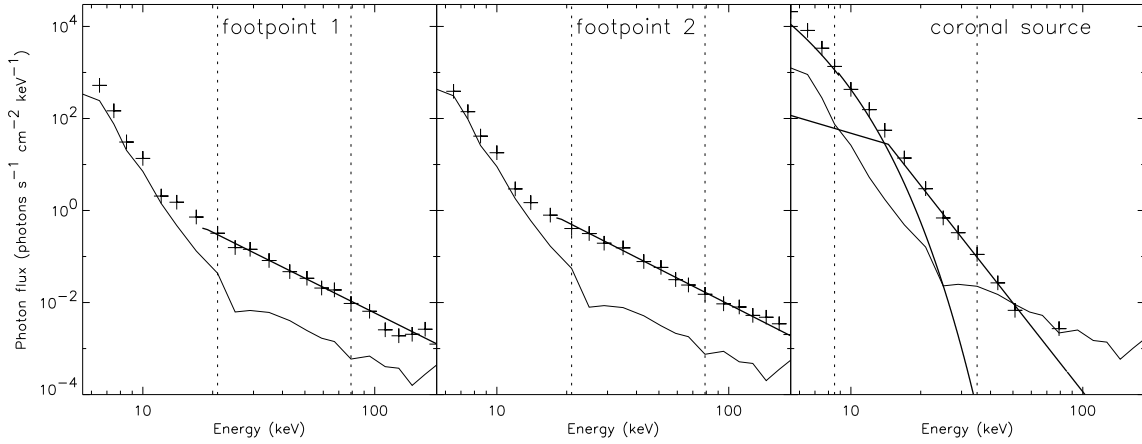


Figure 3.2: Spectra of footpoints and coronal source for the time interval 14:16:48-14:17:36 of the event of July 13th 2005. The energy range for the spectral fitting is indicated by the dotted lines. The thin solid line gives an estimate for the noise level (see Sect. 3.2.2).

energies and a thermal component at low energies, where this was possible. Some of the footpoints did not have any flare emission at lower energies i.e. no measurable thermal emission. In this case only a power law was fitted to the energy range in which the flare emission was stronger than the noise level.

Figure 3.2 shows the spectra of the footpoints (fp 1 & 2, left and middle) and the coronal source (cs, right) for the time interval between 14:16:48-14:17:36 of the July 13th 2005 event. The fitted power-law and thermal components are also presented in Fig. 3.2. For each time interval and each source, we made an estimate of the noise level in the Clean images. A spectrum from a large part in the image that had not been assigned to a source has been calculated and normalized for the area of the individual source ROIs. The result is indicated by the thin lines in Fig. 3.2. This method will probably overestimate the actual noise, but can be used as a rough guide for the determination of the trustworthy energy intervals for the fitting (indicated by the dashed lines in Fig. 3.2).

The influences of the source delimitation and detector selection have been studied extensively. For the event of July 13th 2005, tests have been made with differently defined ROIs, and with images with and without detector 3. Finally, a series of images with natural instead of uniform detector-weighting has been compared. Natural weighting gives the same weight to each sub-collimator, opposed to uniform weighting where the collimators are weighted inversely proportional to their resolution, therefore giving the finer grids more

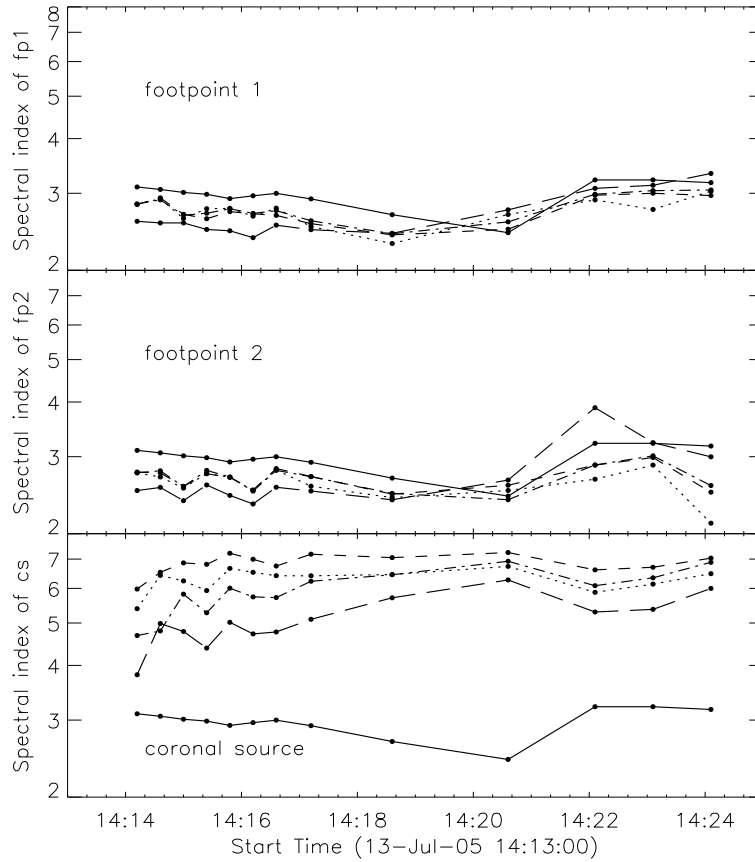


Figure 3.3: Time evolution of spectral index γ of footpoints (*top* and *middle*) and coronal source (*bottom*) for different choices of detectors and regions of interest. *Solid*: full sun; *dotted*: with detector 3; *dot-dashed*: without detector 3, same ROIs as dotted; *dashed*: without detector 3, different ROIs; *long dashes*: images with natural weighting of detectors.

weight. Figure 3.3 shows the time evolution of the spectral index γ , fitted to spectra calculated for different choices of regions, detectors and weighting. The time evolution of the spectral index of full-sun spectra in the same time bins has been given for comparison. Four different cases were studied. Images with detector 3, different ROIs around the same sources, and images without detector three using the same ROIs as in the case with detector 3, as well as images with natural detector weighting. From the time evolution of γ one can see that the differences are small for the footpoints. The quantitative differences for the coronal source are somewhat larger. They may be used for an estimate on the error range of the spectral fittings. Note further that the non-thermal component of the full-sun spectrum is mostly due to foot-

point emission. The coronal source causes a small shift toward softer spectral indices, as expected.

The qualitative behavior of the time evolution and the conclusions drawn from it do not change for the different approaches.

Source separation

The major problem encountered in the event selection was the sufficient separation of the sources. Many nice events had to be discarded because footpoints and coronal source overlap. The separation can be improved to a certain extent by optimizing parameters in the image reconstruction, but in the end one is limited by the flare morphology. Usually the footpoints are distinct and well defined. If any of the ROI's defined as described in section 3.2.2 overlapped, the event was not selected. In the event of Nov. 1st 2003 (Fig. 3.1c) the ROIs come close, as the coronal source is embedded in a loop, visible at 10 keV, that extends nearly all the way to the footpoints. In this situation, the spectrum of the non-thermal component of the coronal source may be influenced by the emission of the footpoints. A similar case is the event of Dec. 4th 2002 (Fig. 3.1a). The source separation in the other three events seems clearly big enough to exclude an influence on each other.

Pileup

Although the flares in our sample are not the largest ones and events with detector livetime (uncorrected monitor rates) below 90% had been discarded in the selection, one still has to consider the possibility of pileup (Smith et al. 2002) in certain time intervals. It does not play a substantial role in the footpoints as they are observed and fitted above the energies where pileup is worst. However, the non-thermal part of the coronal source is observed at energies where pileup might cause problems. We tested the importance of pileup in our events, using the `hsi_pileup_check` routine. This routine calculates the corrected (counter) livetime, the effective pileup counts and the relation between corrected and uncorrected count spectra. Further, we examined images for a "ghost"-source at the position of the coronal source at higher energies. Further, we compared the time evolution of pileup flux to the time evolution of the coronal source flux at the same energy (25 keV for attenuator state 1). The event of July 30th 2005 has attenuator state 3 throughout the observed time interval and shows no sign of significant pileup. In some of the other events (all attenuator state 1), pileup is a concern. For

Table 3.2: Mean difference in spectral index γ between footpoints and between coronal source and footpoints for all events in which it could be determined. Pivot energy E^{piv} for all sources and all events (where determinable). Temperatures derived from full sun spectra.

Date	$\gamma_{\text{fp1}} - \gamma_{\text{fp2}}$	$\gamma_{\text{cs}} - \gamma_{\text{fp1}}$	$\gamma_{\text{cs}} - \gamma_{\text{fp2}}$	
4-Dec-2002	-0.53 ± 0.20	1.22 ± 0.20	0.68 ± 0.15	
24-Oct-2003	0.33 ± 0.04	2.43 ± 0.22	3.07 ± 0.27	
1-Nov-2003	-0.095 ± 0.093	0.72 ± 0.16	0.59 ± 0.24	
13-Jul-2005	0.13 ± 0.07	3.55 ± 0.13	3.68 ± 0.14	
30-Jul-2005	0.13 ± 0.07	1.15 ± 0.38	1.12 ± 0.41	
Date	$E_{\text{fp1}}^{\text{piv}}$	$E_{\text{fp2}}^{\text{piv}}$	$E_{\text{cs}}^{\text{piv}}$	Temperature (MK)
4-Dec-2002	13.74 ± 0.41	14.97 ± 0.63	18.12 ± 0.25	18.30 ± 1.68
24-Oct-2003	-	-	22.74 ± 2.99	22.51 ± 0.05
1-Nov-2003	14.68 ± 1.14	14.00 ± 1.33	15.90 ± 2.36	20.65 ± 1.99
13-Jul-2005	-	-	-	24.95 ± 1.07
30-Jul-2005	-	-	23.92 ± 2.37	24.85 ± 0.31

some times during the event of Nov. 1st and the end of Oct. 24th 2003, more than about 50 % of the observed coronal HXR emission in the range between 20 and 30 keV has to be accounted for by pileup. These times were not used in the further analysis (missing data in Fig. 3.4).

3.3 Results

3.3.1 Soft-Hard-Soft (SHS)

First we present the study of the SHS-behavior of individual sources.

For 4 events, the RHESSI full-sun count lightcurves in the energy-bands 3-12 keV, 25-50 keV and 50-100 keV are shown in Fig 3.4. The time evolution of the fitted non-thermal flux at 35 keV (F_{35}) and the spectral index γ are plotted for each source. The variation in flux of the July 30th 2005 event (not shown in Fig. 3.4). F_{35} of the footpoints correlates well with the total count flux in the 25-50 and 50-100 keV energy bands, indicating that the spectral fits are plausible.

In all previous observations of SHS-behavior (see 3.1) the full sun spectrum

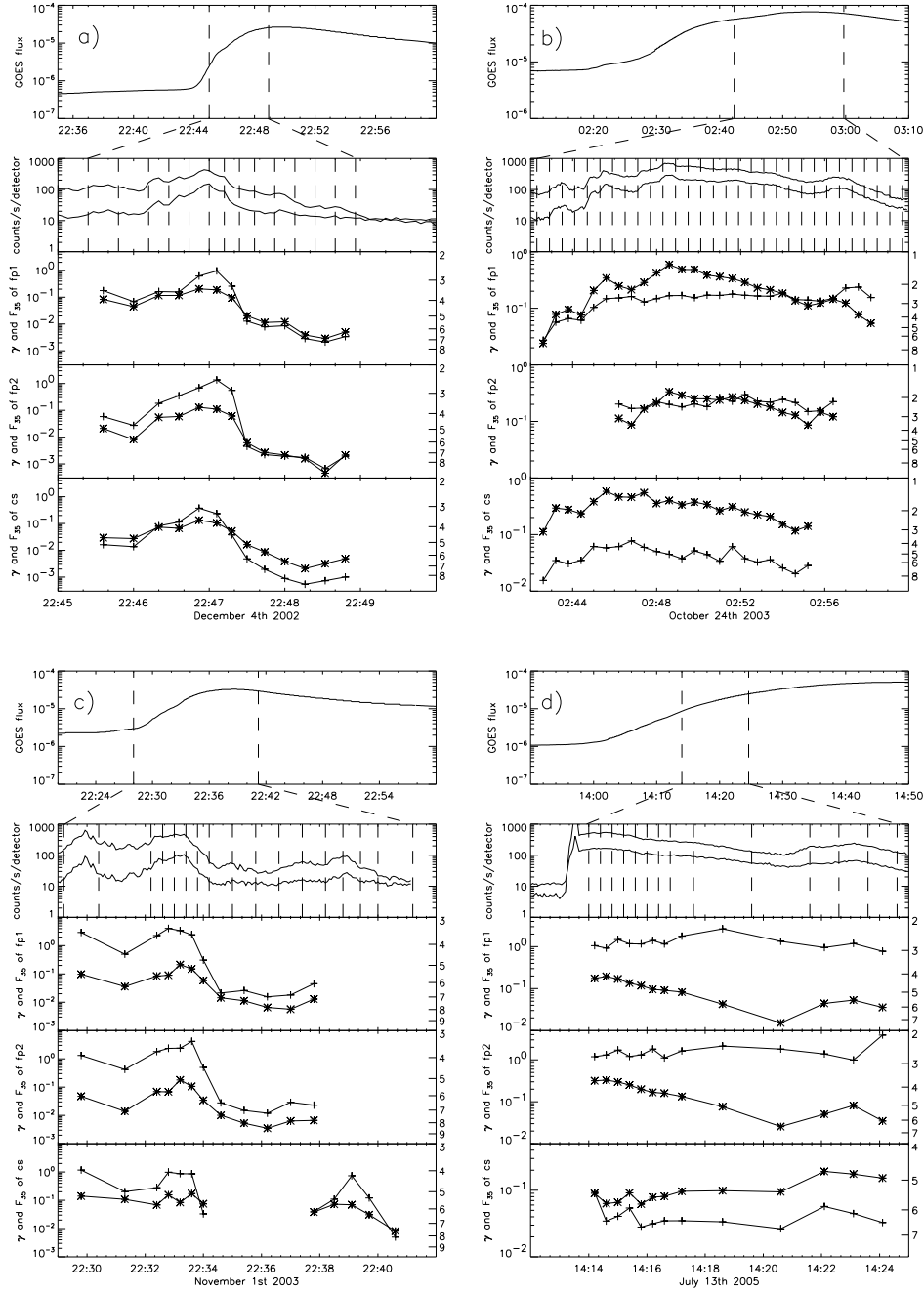


Figure 3.4: *Top:* GOES low-channel lightcurve. The dashed lines mark the analyzed time intervals. *Lower four panels:* RHESSI full sun lightcurves in energy-bands 25-50 keV and 50-100 keV, overplotted is the time binning used for imaging spectroscopy (dashed lines); time evolution of spectral index (γ , crosses) and non-thermal flux at 35 keV (F_{35} [photons $s^{-1}cm^{-2}keV^{-1}$], stars) for footpoints 1& 2 and coronal source (bottom panel). The times between 22:34:30 and 22:37 of the Nov. 1st 2003 event had to be neglected for the coronal source because of pileup.

has been analyzed. As previous measurements were made at relatively high energies to avoid a contribution of the thermal component, they predominantly refer to the footpoints. For the first time, it has become possible to study the temporal evolution of the non-thermal component of the coronal source.

In all events the coronal source varies clearly according to SHS (Fig. 3.4). Three out of five events also show a more or less pronounced SHS-behavior in the footpoints, although there are times when the pattern is not very clear, or flux and spectral hardness anti-correlate. The events of Nov. 1st 2003 and Dec. 4th 2002 show a clear SHS-behavior in all sources. For Oct. 24th 2003, the variation in the flux is small without strong peaks. The event of July 13th 2005 is peculiar. There is an anti-correlation between flux (both, total count flux as well as fitted flux) and spectral hardness in the footpoints.

Pivot point

The first notion of an invariable point in solar flare spectra was made by Gan (1998). This point was termed pivot point and analyzed quantitatively for the first time by Grigis & Benz (2004; 2005). The SHS-behavior, indicating spectral hardening at large fluxes, suggests that the non-thermal spectra at different times intersect at a fixed point in energy and flux. Grigis & Benz (2004) noted that the intersections of all spectra in an event are within a relatively small range of energies. Its average was termed pivot energy. We applied the fitting method they describe in Grigis & Benz (2005) to determine the pivot energy for each source. An example is shown in Fig. 3.5. The results are given in Table 3.2. The physical significance of the pivot energy is not clear. However, it may be useful to describe the SHS-behavior quantitatively

A pivot point could not be found for every source. If the variation in the flux and spectral index is small, the power-law lines are nearly parallel in log-log, and the pivot point is not well defined or does not exist. For one of the two cases where all pivot points could be determined, the pivot energy of the coronal source is higher by 3-5 keV than the pivot energies of the footpoints (see Table 2). In the other case, the three pivot energies are equal within errors. In the two cases where only the pivot energies of the coronal sources were found, the values even exceed 20 keV. All pivot energies for both, coronal source and footpoints given in Table 2 are higher than the mean value of 9 keV found by Grigis & Benz (2004) for full sun spectra. The main contribution of non-thermal emission in full sun spectra originates from the footpoints. The pivot energies of the footpoints reported in Table 2 are outside the range of the half-power distribution of 6.5-12.5 keV reported by Grigis & Benz. However,

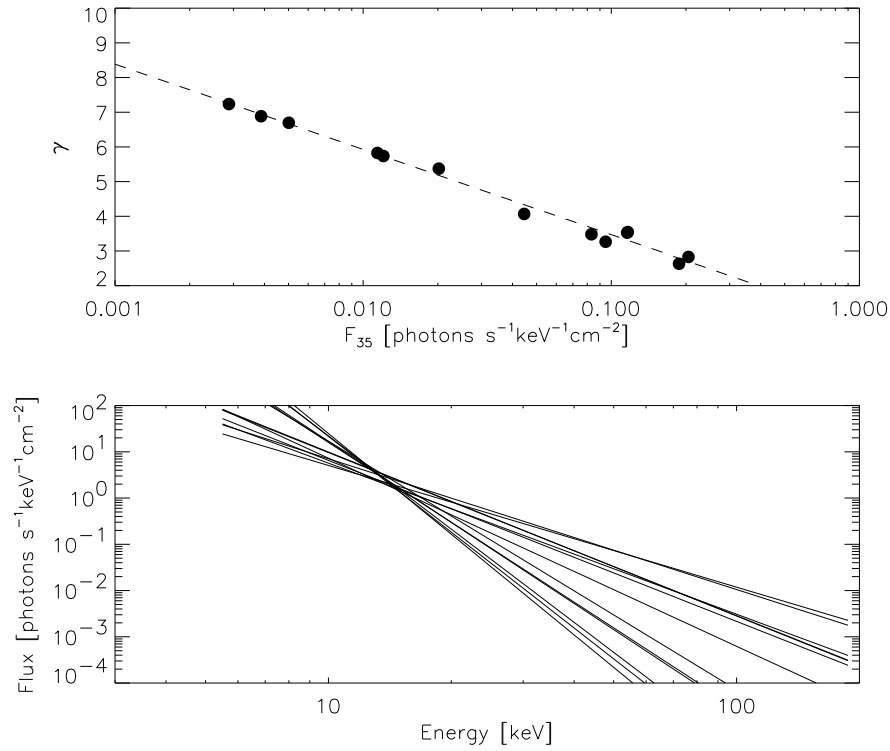


Figure 3.5: Example for the determination of the pivot point (for footpoint no.1 of Dec. 4th 2002). *Top:* flux and spectral index of all time intervals. The locations for the flux and spectral index in the best fitting pivot point model is shown *dashed*. *Bottom:* non-thermal power-law components for all time intervals overplotted. The crossing point agrees with the pivot point found by the above fit.

the deviation is statistically not significant.

3.3.2 Difference in spectra between sources of the same event

Non-thermal spectra in the 20-50 keV range can usually be well approximated by a power law (Fig. 3.2). The flux at a given energy and the spectral index thus characterize the spectrum of a source. In this subsection the differences between spectral indices of the coronal source and the footpoints, and between the two footpoints of each event are investigated. The mean differences in γ time-averaged over the event are given in Table 3.2.

Relation of coronal γ to footpoint γ

The coronal source is softer than both footpoints in all events at nearly all times (Fig. 4). The smallest mean difference of 0.59 ± 0.24 was found for the event of Nov. 1st 2003 for which there is a possibility of source overlap. The maximum mean difference is 3.68 ± 0.14 for the event of July 13th 2005. Table 3.2 points out that $\gamma_{cs} - \gamma_{fp}$ in the 3 well separated events is remarkably larger than in the two more compact events. Note in particular, that the difference between coronal source and footpoints often differs significantly from 2, the value expected from the difference between thick and thin target sources. Nevertheless, the average over all mean differences is 1.82 with a standard deviation of 1.52. The weighted average and mean error are 1.98 ± 0.42 . This finding does not agree with previous reports (Petrosian et al. 2002) based on *Yohkoh* data. A possible explanation for the larger value is our selection of spatially separated sources, avoiding overlap between them.

Differences between footpoints

Emslie et al. (2003) reported differences of 0.3-0.4 between the spectral indices of the two stronger footpoints in their event. For the flares analyzed here, a significant difference is found in only one out of five events, the Oct. 24th 2003 flare. For all other events, the mean difference in γ_{fp} is zero within the statistical uncertainty.

Figure 3.6 shows the distributions of the differences in the spectral indices of the non-thermal emission as measured in all time bins and all events. The difference between coronal source and footpoint spectral index is almost always larger than zero (Fig. 3.6, left). The question of the transition from footpoints to coronal source will be addressed in section 3.3. The differences between the footpoints are given in absolute values, as the footpoint numbering is arbitrary. As expected from the observations of the individual events (Fig. 4), the distribution peaks at zero.

Do the differences in spectral index change in the course of the flare? Figure 3.7 displays the variations through the peak (at 02:48:30) and in the decay phase. The difference between the footpoints' spectral indices does not vary within the statistical error as given by the OSPEX routine. However, the $\gamma_{cs} - \gamma_{fp}$ increases from peak to decay. This is caused by a considerable softening of the coronal source in this time interval (Fig. 4b).

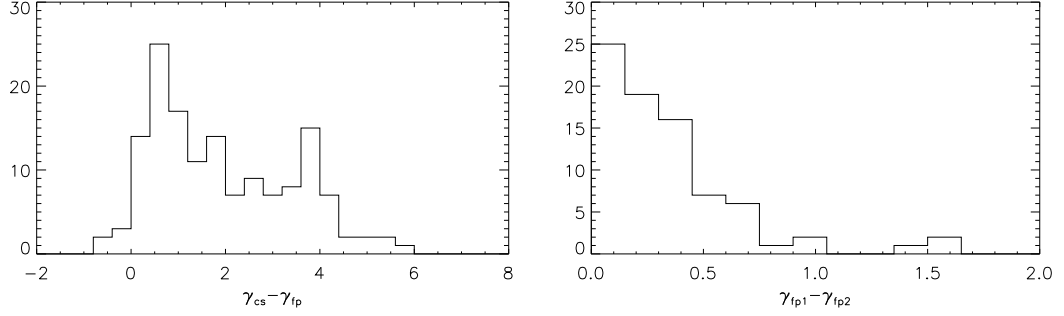


Figure 3.6: Distributions of the differences in spectral index (γ) between coronal source and both footpoints of all events at all time bins (*left*) and between footpoints only (*right*). For the differences between footpoints, absolute values are shown.

Relation between intensity and area of footpoints in the Oct. 24th 2003 event

We compared the total flux of non-thermal photons in the 25-50 keV range and within the 50 % contour for the two footpoints of the Oct. 24th 2003 event for the times where they were best observed.

We determined the footpoint flux from cleaned images using detectors 3-8 and with a pixel size of 0.5 in the 25-50 keV range within the 50% contour ($F_{50\%}$) and define the intensity $f_{50\%}$ as ratio of flux divided by the area ($A_{50\%}$) of the contour,

$$I_{50\%} = \frac{F_{50\%}}{A_{50\%}} ,$$

where the area of the clean beam has been subtracted. Figure 3.8 shows the time evolution of $F_{50\%}$, the area $A_{50\%}$ and the intensity $I_{50\%}$.

The total flux $F_{50\%}$ correlates with the full sun count flux. Further, it correlates with the fitted flux F_{35} (comp. Fig. 3.4), validating the applied methods. The softer footpoint, no. 1, is always brighter than footpoint no. 2. and is larger in area. The harder footpoint (no. 2) has the higher intensity for most of the observed time.

Thermal emission of footpoints

The coronal source dominates at low energies in all selected events. Images at low energies often do not show strong emission at the position of the footpoints. Sometimes no fit to the thermal component of the footpoints was possible. As demonstrated in Fig. 3.2, the noise level at low energies (few keV up to 10 keV) reaches about a tenth of the emission of the coronal source.

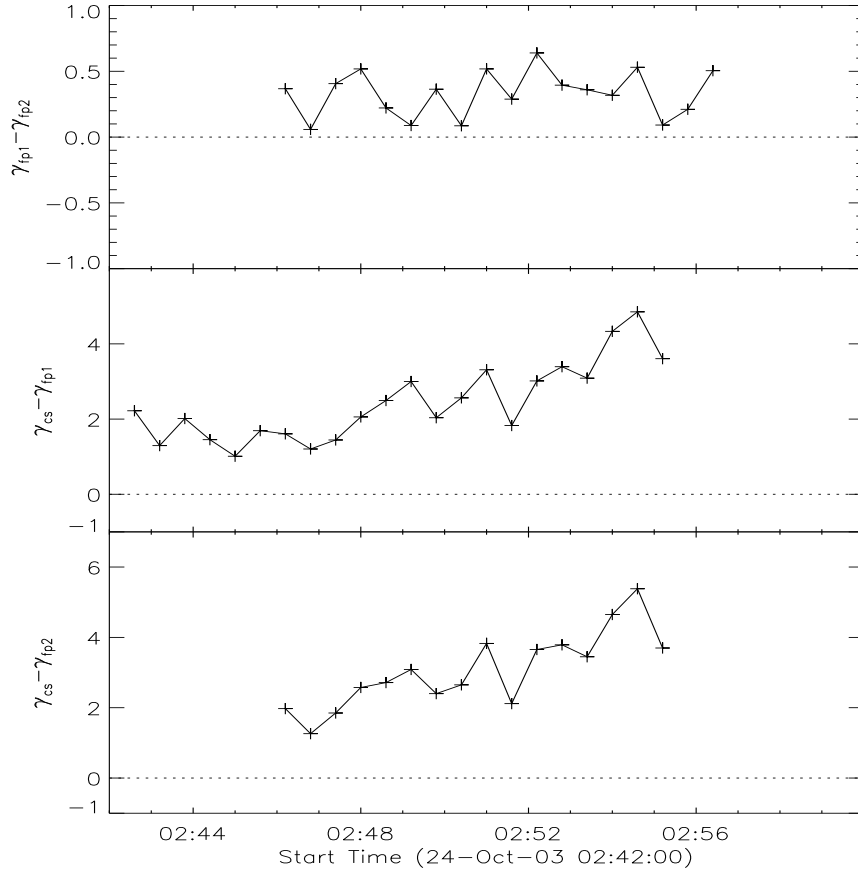


Figure 3.7: Time evolution of the difference between spectral indices of the three sources for the event of Oct. 24th 2003

A rough overview on all times of all events yields the following statistics on the thermal emission of the footpoints:

- One footpoint with measurable thermal emission during more than 50 % of the time (fp no. 1 of the Dec. 4th 2002 event).
- Two footpoints with no measurable thermal emission at all times (fp no.2 of the July 30th 2005 event and fp no. 2 of Oct. 24th 2003).
- All other footpoints show thermal emission in the spectrum for 20 % of the time on the average.

A formal fitting has been performed at the defined regions of interest for the undetected thermal footpoint emission in Fig. 3.2. The result corresponds to the uncertainty level and yields an upper limit for the thermal footpoint emission. The relations between the emission measure of the coronal source

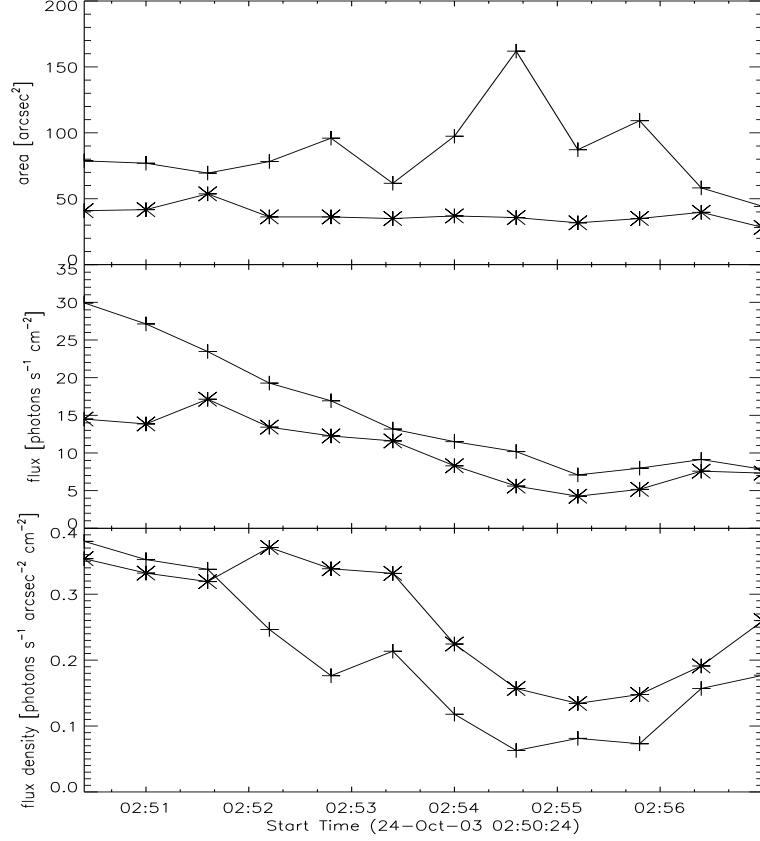


Figure 3.8: Time evolution of area of 50 % contour in the 25 - 50 keV image, flux within contour in photons s⁻¹ cm⁻² and the intensity (flux/area) of footpoints of Oct. 24th 2003 event. *Crosses* show footpoint no.1, *asterisks* indicate footpoint no.2 as numbered in Fig. 1.

and the footpoints are

$$\frac{EM_{fp1}}{EM_{cs}} < 0.2$$

and

$$\frac{EM_{fp2}}{EM_{cs}} < 0.1 \quad .$$

The fact that almost all of the footpoints studied here have a thermal spectrum at some time and the well-known fact that flare observations at EUV wavelengths show thermal emission from the footpoints suggest that there may well be thermal emission from footpoints all the time. In soft X-ray observations by *Yohkoh/SXT*, such emission has been reported e.g. by McTiernan et al. (1993) and Hudson et al. (1994). However, RHESSI can only observe it if the

emission measure is at least 10 % of the coronal source and at a temperature of several million Kelvin. Therefore, the thermal emission measured in full sun spectra is predominantly emission of the coronal source. Table 3.2 gives the average temperatures as fitted to full sun spectra. They are representative for the temperature of the coronal source.

3.4 Discussion

3.4.1 Coronal source shows SHS-behavior

Although previously reported in the literature, the existence of a non-thermal component in the coronal source is not trivial. As the thermal component is strong and any non-thermal emission very soft, the latter is just an extension at a much lower flux (see Fig. 3.2c). We have tested the possibility of flux pileup contributing to the range of energies where the non-thermal component was fitted (section 3.2.2). These tests show that the observed HXR tail cannot be caused just by pileup but that there is significant HXR source emission. We cannot exclude in all cases, however, that the extension cannot be fitted equally well with a second thermal component at a much higher temperature. In cases like Fig. 3.2c, the fit with two thermal components has a higher χ -square and is therefore less likely. We will thus continue to refer to the high-energy extension as non-thermal.

It is a remarkable result that for 5 out of 5 events, the time-evolution of the spectral index γ of the coronal sources shows SHS-behavior. The event of July 13th 2005 is noteworthy, showing SHS-behavior in the coronal source, but not in the footpoints (Fig.3.4d). The SHS-behavior of the coronal source would not be expected if SHS was just a transport effect such as Coulomb collisions or an electric field. Filtering of low energy electrons in the loop by collisions would not have an effect on the coronal source from where the particles may have originated. An induced electric field due to the return current $E = \eta j^{ret}$ (where η is the electric resistivity), reflecting low energy particles from the loop back upwards would even lead to a softer spectrum in the coronal source, i.e. an anti-correlation between flux and spectral hardness.

Although the notion of a pivot point was introduced by Grigis & Benz (2004) as a convenient and quantitative characterization of the SHS-behavior, Table 3.2 suggests a possible physical significance of the pivot energy: E_{cs}^{piv} seems to increase with the temperature of the coronal source. The significance needs to be confirmed by a larger sample. Another hint on a possible physical relevance is the value of the pivot energy. In the flares in which it could be

determined, the pivot energy of the coronal source is at the energy (within the error range) where the spectra of the thermal and non-thermal components intersect (Fig. 3.2c) or higher. Table 3.2 also shows that the pivot energy is an order of magnitude higher than the mean thermal energy. A deviation from a Maxwellian energy distribution or from isothermal homogeneity would be necessary to interpret the pivot energy as the starting point for the non-thermal acceleration. We do not consider it impossible, but highly speculative.

3.4.2 Soft-hard-soft behavior of the full sun

The soft-hard-soft (sometimes soft-hard-harder) behavior of solar flares has been extensively studied in full sun observations (see 3.1). As the coronal source usually dominates in the early phase of an event and remains luminous longest, but at peak time the non-thermal part of full-sun spectra is dominated by the footpoints (e.g. Fig. 3.3), the reported SHS results of full sun observations need to be tested for the possibility of spatial changes dominating temporal changes.

We have compared the time evolution of the non-thermal flux F_{35} of the coronal source and of the combined footpoints to investigate the influence of a change in predominance from the coronal source emission to footpoint emission and back to coronal emission (coronal-footpoint-coronal) on the SHS feature. Figure 3.9 shows the only event where an indication of such an effect could be found. The footpoint emission is weaker than the coronal source in the beginning, exceeds the coronal emission when the spectral index is hardest and decreases below the level of coronal emission afterwards. The (negative) spectral index of the full sun correlates with both the flux of footpoints and the flux of the coronal source. It continues to correlate with the coronal source when the footpoints vanish. We conclude that a coronal-footpoint-coronal effect may enhance the SHS feature in full sun observations, but does not cause it. Therefore, the SHS-behavior must be a property of the sources themselves.

3.4.3 Differences in spectra

Difference between coronal source and footpoints

Assuming an electron power-law distribution for the electron energy E of the form

$$F(E) = AE^{-\delta} \quad (3.1)$$

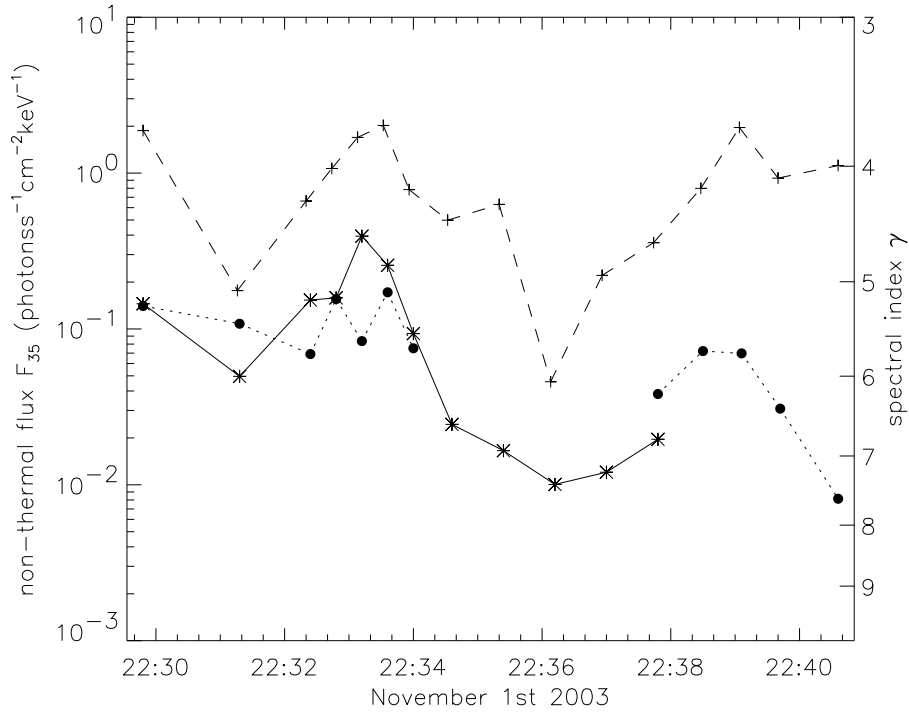


Figure 3.9: Non-thermal flux F_{35} fitted to the spectrum of the coronal source (dotted line) compared to summed flux of both footpoints (solid line) of the event of Nov. 1st 2003. The *dashed* line gives the spectral index of the full sun spectra.

producing thin-target bremsstrahlung-emission in the coronal source, the observed photon-spectrum at photon energies ε is

$$I_{thin}(\varepsilon) \sim \varepsilon^{-(\delta+1)} \quad (3.2)$$

with spectral index $\gamma_{thin} = \delta + 1$. Reaching the chromosphere, the accelerated electrons will be fully stopped, producing thick-target bremsstrahlung with a photon-spectrum

$$I_{thick}(\varepsilon) \sim \varepsilon^{-(\delta-1)} \quad (3.3)$$

having a spectral index $\gamma_{thick} = \delta - 1$ (Tandberg-Hanssen & Emslie 1988). In such a simple scenario one would therefore expect a difference in the photon spectral index $\gamma_{thin} - \gamma_{thick} = 2$ between the coronal source and the footpoints. Indeed we find always a difference between the spectral index of the coronal source and the footpoints. In 2 events out of 5, the difference is considerably larger than 2. This result excludes a scenario in which the same electron beam

first produces thin target emission in the corona, then thick target emission in the chromosphere. Different particle populations seem to be involved or a filter mechanism may operate causing low-energetic electrons to preferentially lose energy before they reach the chromosphere and therefore hardening the spectrum. Candidates for such a transport effect are collisions and the electric field of the return current.

The 3 events in which the difference is smaller than two include those two with small source separation. The similarities in the spectra can therefore be partly accounted for by a situation that is between the assumed ideal thick and thick targets. This may be the case when electrons substantially lose energy before reaching the chromosphere.

Difference between footpoints

The difference between the footpoint spectral indices is only significant in one event out of five (Oct. 24th 2003). The larger and more luminous footpoint is softer. The opposite is the case in the flare of July 23rd 2003, analyzed by Emslie et al. (2004).

3.5 Conclusions

A selection of five RHESSI events with three concurrent X-ray sources (coronal source and two footpoints) has been studied regarding the spectral relations between the sources. All spectra can be fitted with a non-thermal component having a power-law photon distribution. Although no low-energy soft X-ray observations are available for comparison, we believe that they probably are examples for Masuda-type sources (Masuda et al. 1994), but our looptop sources are generally softer than the one found by Masuda. Therefore, such events are easier to detect with RHESSI than they were with *Yohkoh* and are more frequent than inferred previously. In addition, all coronal sources and some of the footpoints at times show a thermal component. The major results are:

- All coronal sources evolve according to the same time evolution in spectral hardness. The higher the flux, the harder (smaller γ) the non-thermal component. This soft-hard-soft pattern correlates with the non-thermal flux without measurable delay. Transport effects such as collisions or an induced electric field cannot cause SHS in the coronal source.

- As the emission of the footpoints often dominates at 35 keV, it is not surprising that the pattern, previously reported for full sun observations, is also found in the footpoints of three out of 5 events. Imaging spectroscopy suggests that SHS is a feature of all sources, and thus possibly of the accelerator itself.
- SHS in full sun observations cannot be explained by a change of the dominant source (softer coronal source present at all times plus a hard footpoint source with time-varying intensity). If SHS was caused by such an effect, neither source would display it individually.
- The difference in spectral index between non-thermal coronal and footpoint emission is not 2, as would be the case if the difference was simply caused by thin and thick target bremsstrahlung, respectively. Smaller differences in γ may be explained by an intermediate situation between the two extremes. The plasma of the coronal source could act as thick target for low energetic electrons and as thin target for higher electron energies. The cases with $\gamma > 2$ require a filter effect in the propagation preferentially reducing the distribution at lower energies. Such a filter may be collisions or an electric field.
- The pivot energy, characterizing the SHS-behavior of the non-thermal emission, is at the energy where the distribution of the thermal and non-thermal components balance in half of the cases. In the other half, the pivot energy is higher than this point.
- The pivot energy at the footpoints is significantly lower in all cases (16 – 23 keV for the coronal source vs. 14 – 15 keV for the footpoints). Such a difference suggests a filter acting during particle propagation to the footpoints, reducing lower energies more than higher energies.
- In one out of 5 events the two footpoints have significantly different spectral indices, $\Delta\gamma = 0.33 \pm 0.04$. The difference is constant during the event, although the spectral indices vary in time. Again, an energy filter during propagation seems to be at work, differing in one flare for the two legs of the loop.
- The photon flux at energies below about 15 keV is dominated by thermal emission. Most of this emission originates from the coronal source. If its temperature correlates with the pivot energy it may hint at a physical significance of the pivot energy for the acceleration process, but needs further investigation.

- As pointed out before from *Yohkoh/SXT* observations, the thermal emission from the coronal source often significantly exceeds the thermal emission of the footpoints, which is detectable in some events and at some times.

This analysis has shown that the non-thermal X-ray emission in coronal sources cannot only be detected by RHESSI, but can also be studied in time. As the coronal source is directly related to flare energy release, this opens the possibility of further investigating the enigmatic acceleration process of electrons. The temporal and spectral relation of the coronal source to the footpoints suggests an intricate connection between corona and chromosphere. While a comprehensive interpretation of our results in terms of particle propagation and thermal conduction is beyond the scope of this study, the idea that flare energy release and particle acceleration are closely related to the coronal source is supported by our results.

Chapter 4

Exploring the connection between coronal and footpoint sources in a thin-thick target solar flare model*

M. Battaglia¹, and A. O. Benz¹

Abstract

Context. Hard X-ray emission of coronal sources in solar flares has been observed and studied since its discovery in Yohkoh observations. Several models have been proposed to explain the physical mechanisms causing this emission and the relations between those sources and simultaneously observed footpoint sources.

Aims. We investigate and test one of the models (intermediate thin-thick target model) developed on the basis of Yohkoh observations. The model makes precise predictions on the shape of coronal and footpoint spectra and the relations between them, that can be tested with new instruments such as RHESSI.

Methods. RHESSI observations of well observed events are studied in imaging and spectroscopy and compared to the predictions from the intermediate thin-thick target model.

Results. The results indicate that such a simple model cannot account for the observed relations between the non-thermal spectra of coronal and footpoint sources. Including non-collisional energy loss of the electrons in the flare loop due to an electric field can solve most of the inconsistencies.

* This chapter is published in *Astronomy & Astrophysics* **466**, 713 (2007)

¹ Institute of Astronomy, ETH Zurich, CH-8092 Zurich, Switzerland

4.1 Introduction

How well do we understand the physics behind solar flares? Solar flares release a large portion of their energy within seconds to minutes. A significant part of this energy goes into accelerated electrons and ions which then precipitate to the chromosphere along the field lines of a magnetic loop. The chromosphere acts as a thick target on the precipitating particles, leading to characteristic hard X-ray (HXR) emission. The first observations of such footpoint sources were made by Hoyng et al. (1981). Masuda et al. (1994) found another HXR source near the top of flare loops in Yohkoh observations. Feldman et al. (1994) analyzed such coronal sources with Yohkoh BCS and SXT. Due to the normally low coronal densities one would expect a thin target emission from this coronal source. However, the observations by Feldman et al. (1994) yield quite high column densities ($10^{20}\text{cm}^{-2} < N < 7 \cdot 10^{20}\text{cm}^{-2}$) in the coronal source that would act as a partly thick target on electrons below a certain energy. On the basis of the observations by Masuda et al. (1994) and Feldman et al. (1994), Wheatland & Melrose (1995) developed a simple model that has been used and investigated further (eg. Metcalf & Alexander 1999; Fletcher & Martens 1998). The model consists of four basic elements; a particle accelerator on top of a magnetic loop, a coronal source visible in SXR and HXR, collision-less propagation of particles along the magnetic loop and HXR-footpoints in the chromosphere. The coronal source acts as an intermediate thin-thick target on electrons depending on energy (thick target for lower energetic electrons, thin target on higher energies). We will therefore refer to this model as intermediate thin-thick target, or ITTT model.

For large enough column depths or steep enough electron spectra, almost all electrons would be stopped in the loop and no footpoints could be observed. Such events were observed with Yohkoh and later with RHESSI. Veronig & Brown (2004) analyzed flares with faint footpoint emission but a dense loop acting as a thick target on electrons of energies up to 60 keV.

Due to its high spectral and spatial resolution, RHESSI (Lin et al. 2002) provides the means to perform imaging spectroscopy on events with multiple sources. Battaglia & Benz (2006) showed that it is possible to study the non-thermal X-ray emission of coronal sources and footpoints and the relations between them in detail.

Therefore, the ITTT model and its predictions can be tested using RHESSI data of well observed events. It is the simplest model that can explain the Yohkoh data. Can it also explain RHESSI data?

4.2 Theoretical model

The ITTT model features a dense coronal source into which a beam of electrons with a power-law energy distribution is injected. Some high energy electrons then leave the dense region, precipitating down to the chromosphere. The coronal region acts as a thick target on particles with energy lower than a critical energy E_c and as thin target on electrons with energy larger than the critical energy. This results in a characteristic HXR spectrum as well as SXR emission due to collisional heating of the coronal region. The altered electron beam reaches the chromosphere, causing thick target emission in the footpoints of the magnetic loop. The predicted photon spectra are shown in Fig. 4.1. The coronal spectrum consists of two power-law components with a break at E_c . The footpoint spectrum has a break at the same energy as the coronal spectrum and is a power-law at high energies.

The model predicts the following properties:

1. The coronal and footpoint spectra intersect at the critical energy ($E_c = E_{intersect}$).
2. There is a break at E_c in the individual spectra of coronal source and footpoints, but not in the sum of the two spectra.
3. The spectral indices below and above the break in the coronal source have a difference of $\gamma_2^{cs} - \gamma_1^{cs} = 2$.
4. The spectral index of the coronal source below the break is equal to the spectral index of the footpoints above the break ($\gamma_1^{cs} = \gamma_2^{fp}$).
5. The difference between the spectral indices of the coronal source and the footpoints at high energies is $\gamma_2^{cs} - \gamma_2^{fp} = 2$.
6. Coronal source and footpoints have the same intensity at E_c .
7. SXR and HXR emission in the coronal source are spatially coincident.

4.3 Observations

4.3.1 Event selection and spectral analysis

We analyzed the five events described in Battaglia & Benz (2006) in an interval of 3 RHESSI spin-periods (about 12 s) around the time of maximum HXR-emission. The events are listed in Table 4.1.

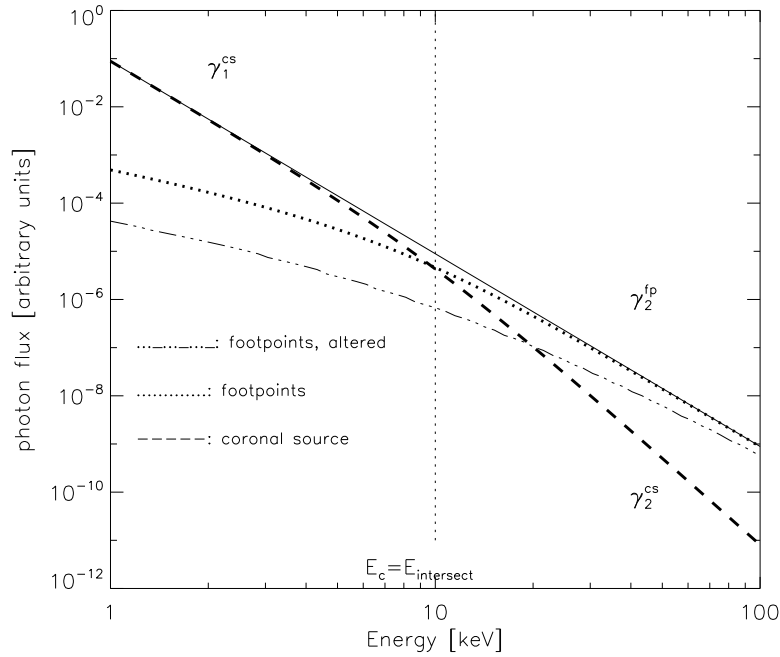


Figure 4.1: Schematic photon spectra for electron distribution with power-law spectral index $\delta = 5$ and critical energy $E_c = 10$ keV. The dashed line gives the spectrum of the coronal source with the spectral indices $\gamma_1^{cs} = \gamma_2^{fp} = \delta - 1$ and $\gamma_2^{cs} = \delta + 1$. The dotted line indicates the combined spectrum of the two footpoints. The footpoint spectrum is a power-law with spectral index $\gamma_2^{fp} = \delta - 1$ at high energies. The solid line is the total of coronal source and footpoints (pure thick target). The dash-dotted line gives the footpoint spectrum from an electron population that has been altered in the loop (see Discussion).

Imaging spectroscopy applying the Clean algorithm for image reproduction was used to produce spectra of coronal sources and footpoints. Reasons for favoring Clean over Pixon are discussed in Battaglia & Benz (2006). To compare the observations with the model, the footpoints were treated as one region and only a total spectrum over both footpoints has been computed. The coronal sources have been fitted with a thermal component and a non-thermal power-law, the footpoints only with a non-thermal component. Varying the starting fit parameters and the fit energy range provided a validation for the stability of the fit and an estimate of the range of spectral index values. The spectra and fits are shown in Fig. 4.2.

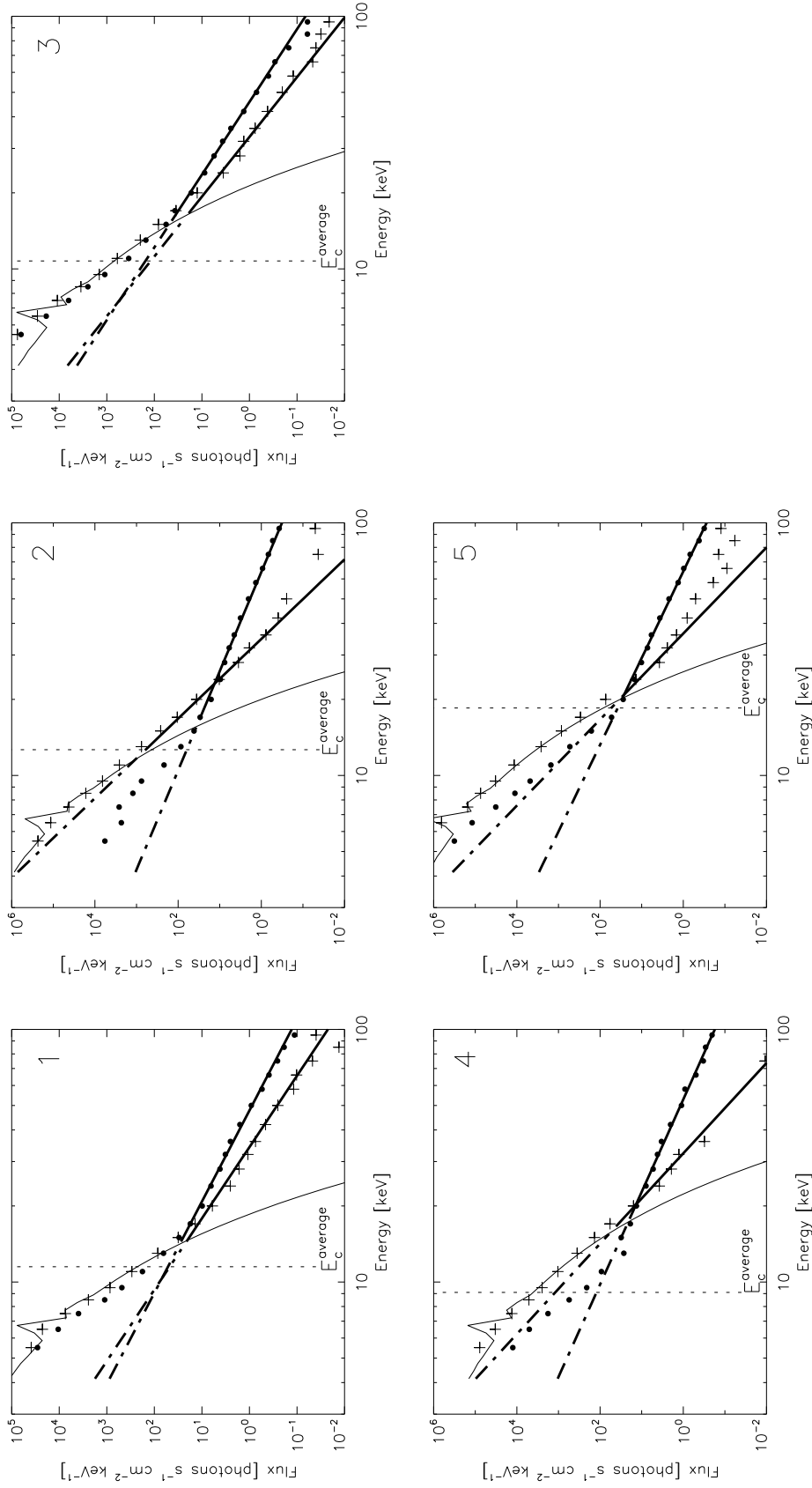


Figure 4.2: Coronal (*crosses*) and footpoint (*dots*) spectra of the five analyzed events. The thin solid line indicates the thermal fit to the coronal source. The thick solid lines give the power-law fits to coronal source and footpoints. Their extension to low energies (not observed) is given as a dot-dashed line. The dotted line indicates the average critical energy.

Table 4.1: Eventlist. The time indicates the peak time in the 50 - 100 keV energy band.

No.	Date	Time	GOES class
1	4-Dec-2002	22:47:02	M2.7
2	24-Oct-2003	02:48:42	M7.7
3	1-Nov-2003	22:33:14	M3.3
4	13-Jul-2005	14:14:30	M5.1
5	30-Jul-2005	06:32:06	X1.3

4.3.2 Density and critical energy

In the ITTT model, the critical electron energy for the transition between thick and thin target for a given column density N_0 is given by equating the source size to half of the mean free path,

$$E_c = \sqrt{2KN_0} \quad (4.1)$$

with the constant $K = 2\pi e^4 \ln \Lambda$. The Coulomb logarithm $\ln \Lambda$ is about 20 for the electron densities and temperatures in the presented sample. The column depth the electron beam passes in the coronal source was computed using RHESSI and GOES data, following the treatment in Wheatland & Melrose (1995). For a source volume V , a total source diameter of $V^{1/3}$ is assumed. An electron beam injected in the middle of the source would then travel half this distance, giving a column depth of:

$$N_o = \frac{n_e V^{1/3}}{2} = \sqrt{EM} \cdot \frac{A^{-1/4}}{2} \quad (4.2)$$

where the electron density $n_e = \sqrt{EM/V}$ using the observed emission measure EM and the volume $V = A^{3/2}$. The area A was measured from the 50% contour of the coronal source in RHESSI Clean images at energy 10 - 12 keV, taking into account the Clean-Beam size and effects of the pixel size on the contour determination.

The emission measure was computed from spectral fits to RHESSI full sun spectra and the spectrum of the coronal source only. As noted by Battaglia & Benz (2006), the thermal footpoint emission generally is very faint in RHESSI observations. Therefore, the thermal emission measured in full sun spectra is predominantly coronal emission. However, the spectral fittings deviate

slightly, the temperature being lower and the emission measure higher for the imaging spectroscopy fit. We therefore use both as a range of possible column densities.

Additionally, we computed the GOES emission measure and temperature for comparison. The range of all RHESSI and GOES emission measures then gives an estimate of the accuracy for the column densities and critical energies (Table 4.2).

4.3.3 Position of coronal source at different energies

The ITTT model predicts spatial coincidence of the coronal emission for all energies. To check for this, Clean images at different energies were made and the centroid of the 50% emission of the coronal source was computed in order to get the position. At energies higher than 20 keV, the footpoint emission starts to dominate, making an accurate determination of the coronal source-position difficult. We determined the centroid positions for the energy range 6-12 keV (thermal) and 16-22 keV (partially non-thermal).

4.4 Results

The main numerical results are given in Table 4.2. We find column densities between $2.1 \cdot 10^{19} < N_0 < 1.2 \cdot 10^{20} \text{ cm}^{-2}$. This yields a range of E_c from 7.7 keV - 21 keV, significantly lower than the values calculated by Wheatland & Melrose for Yohkoh events ($15 \text{ keV} < E_c < 40 \text{ keV}$). The comparison of the data with the predictions from the ITTT model is not always possible due to the presence of the thermal component. Especially, the estimated critical energy is within the range dominated by the thermal component in all events. Comparing the data with the predictions from the ITTT model gives the following results, following the numbering in Sect. 4.2:

1. The power-law fits of the non-thermal coronal and footpoint spectra intersect at energies $E_{\text{intersect}} = 7.6 - 23.1 \text{ keV}$. In 3 events, this energy is within or just outside the estimate for the critical energy derived from eqns. (4.1) and (4.2). Therefore $E_c \approx E_{\text{intersect}}$. In two events (no. 2 and 4), $E_{\text{intersect}}$ is significantly higher than the computed E_c ($E_{\text{intersect}} > E_c$).
2. In the events with $E_c \approx E_{\text{intersect}}$ the estimated break energies and intersection energies are in the energy range dominated by the thermal

Table 4.2: Summary of observed parameters to be compared with the theory. The power-law spectrum of the coronal source can only be observed at energies higher than the thermal emission, therefore no value for the part below the break could be determined.

Event	1	2	3	4	5
γ_1^{cs}	-	(6.3 \pm 0.1)	-	-	-
γ_2^{cs}	3.5 \pm 0.7	6.3 \pm 0.1	4.2 \pm 0.4	5.6 \pm 0.2	5.9 \pm 1.0
γ_2^{fp}	2.8 \pm 0.2	2.5 \pm 0.1	3.5 \pm 0.1	2.7 \pm 0.2	2.9 \pm 0.1
$\gamma_2^{cs} - \gamma_2^{fp}$	0.7 \pm 0.7	3.8 \pm 0.1	0.7 \pm 0.4	2.9 \pm 0.3	3 \pm 1.0
N_0 (cm $^{-2}$)	(2.5-4.9) $\cdot 10^{19}$	(2.8-6.1) $\cdot 10^{19}$	(2.1-4.3) $\cdot 10^{19}$	(2.6-3.0) $\cdot 10^{19}$	(7.1-12) $\cdot 10^{19}$
E_c (keV)	9.5-13.5	10.3-15	8.9-12.6	7.7-10.5	16.2-20.8
$E_{intersect}$ (keV)	10.3	23.1	7.6	20.2	20.9

emission of the coronal source. A break in the coronal spectrum can therefore not be detected, but might still exist. In events nos. 2 and 4, where $E_{intersect} > E_c$, the intersection point of the power-law spectra is observed, but without a break, contradicting the prediction.

3. In event 2, the intersection energy is well outside the thermal emission but $\gamma_2^{cs} - \gamma_1^{cs} \neq 2$ in the coronal source, contrary to the prediction.
4. In event 2, $\gamma_1^{cs} > \gamma_2^{fp}$, not equal as expected from the model.
5. $\gamma_2^{cs} - \gamma_2^{fp} > 2$ in three events and $\gamma_2^{cs} - \gamma_2^{fp} < 2$ in two events.
6. In three events, E_c and $E_{intersect}$ of the non-thermal fits are within the thermal emission of the coronal source. In event 2, $E_{intersect}$ is observed with the coronal source being brighter than the footpoints at E_c .
7. No significant positional differences between energies 6 - 12 keV and 16 - 22 keV have been found (see Fig. 4.3). Due to the increasing footpoint brightness at higher energies, an accurate determination of the coronal source centroid above 22 keV is not possible.

4.4.1 Energy input into the corona

Wheatland & Melrose (1995) proposed that the collisional energy necessary to produce the non-thermal bremsstrahlung emission in the coronal source is

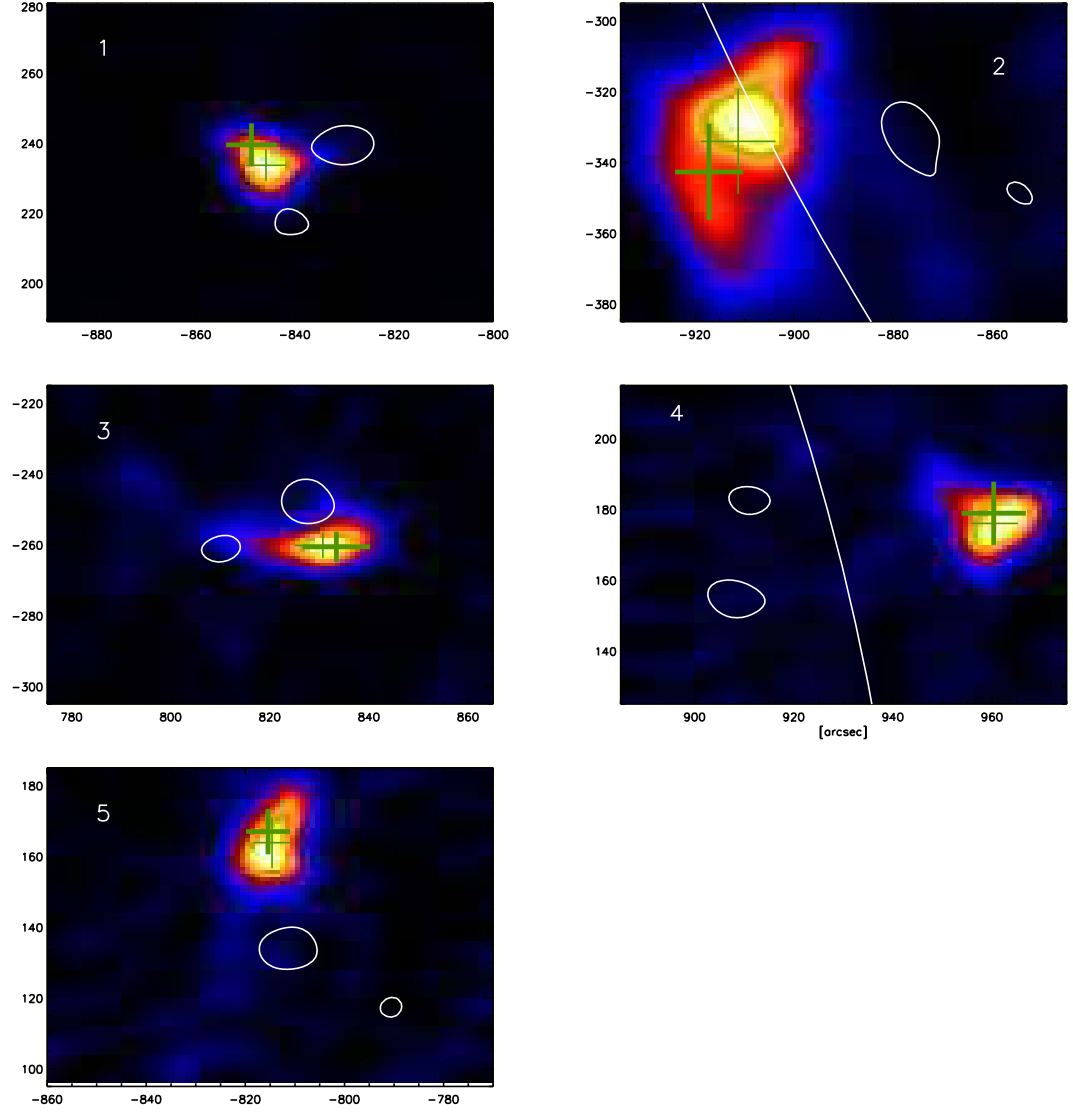


Figure 4.3: Images of all events at energies 10 - 12 keV. The 50% contours of the maximum of the footpoints are given (black). The white crosses indicate the position of the 50% centroid at energies 6 - 12 keV (thin) and 16 - 22 keV (thick) with error bars.

sufficient to account for the observed heating of the coronal source. They referred to standard flare values (flux, duration, electron spectral index) to estimate the non-thermal energies. With the observations presented here the energy input into the individual coronal source can be determined.

We compute the change in thermal energy ΔE_{th} in the coronal source between two times in the flare. The thermal energy is calculated according to $E_{therm} = 3k_B T \sqrt{EM \cdot V}$ with a filling factor of unity.

The non-thermal energy input in the coronal source is computed from the non-thermal coronal spectrum. As cutoff energy, we used the intersection point of the thermal and non-thermal emission. Saint-Hilaire & Benz (2005) found that the average relation between photon-turnover and electron-cutoff is $E_{cutoff}^{electron} = E_{turnover}^{photon} \cdot 1.7$. This gives an upper limit for the electron cutoff energy and therefore a lower limit for the total energy input.

Comparing the two lower limits, we find that the average non-thermal energy input is at least of the same order as the change in thermal energy i.e. $\Delta E_{non-th} \geq \Delta E_{th}$ in agreement with the prediction of the ITTT model. For a lower electron cut-off energy, the non-thermal energy input could be up to an order of magnitude higher.

4.5 Discussion

The ITTT model as presented by Wheatland & Melrose (1995) predicts a critical electron energy E_c marking the transition between thin- and thick target emission. This energy is likewise the intersection energy $E_{intersect}$ between the non-thermal spectra of the coronal and footpoint sources. How can it then be explained in the frame of the ITTT model that in events 2 and 4 the estimated E_c is significantly lower than the observed $E_{intersect}$?

E_c as calculated here may be a lower limit. Including collisional deflections of the electrons within the coronal target rather than just energy-loss, the electron paths would become longer and the critical energy for thin target emission higher. This would increase E_c and could bring it up towards the observed $E_{intersect}$. In that case however, one would expect to observe a break at $E_{intersect}$. This is not the case. Further, the difference $\gamma_{cs}^2 - \gamma_{fp}^2$ is higher than 2 in both of these events, making this explanation even less likely.

An attractive possibility to interpret both, the absence of a break and the larger difference in spectral index is non-collisional energy loss of the electrons in the loop due to the electric field caused by the return current. This would result in a harder and fainter footpoint spectrum, shifting $E_{intersect}$ to energies higher than E_c . The expected footpoint spectrum in the case of electrons

losing 15 keV of energy in the loop is indicated in Fig. 4.1.

The remaining discrepancy then is the difference in spectral index $\gamma_{cs}^2 - \gamma_{fp}^2$ being smaller than two in events 1 and 3. Such a difference could result where the targets cannot be clearly separated into thin and thick, for example if the sources are close as is the case in those events. Part of the emission selected for the footpoints could originate from the coronal source, giving a mixed thin-thick target spectrum for the footpoints. More observations are necessary to confirm this explanation.

An estimate of the non-thermal energy input into the coronal source compared to the change of the thermal energy content in the coronal source shows that collisions as manifest in hard X-ray emission may account for the observed heating of the coronal source. Depending on the electron cut-off energy, the amount of energy deposited in the target might even exceed the observed thermal energy. However, we did not consider cooling of the coronal source due to thermal conduction or radiation. Such effects could lead to a thermal energy input larger than observed.

4.6 Conclusions

We showed that a simple thin-thick target model as the one proposed by Wheatland & Melrose (1995) cannot explain all observations made with RHESSI. Modifications of the model are necessary, the simplest being the consideration of the electric field due to the return current. In the absence of a balancing ion flux, such a return current is predicted from basic physics in view of footpoint sources.

Chapter 5

Observational evidence for return currents in solar flare loops^{*}

M. Battaglia¹ and A. O. Benz¹

Abstract

Context. The common flare scenario comprises an acceleration site in the corona and particle transport to the chromosphere. Using satellites available to date it has become possible to distinguish between the two processes of acceleration and transport, and study the particle propagation in flare loops in detail, as well as complete comparisons with theoretical predictions.

Aims. We complete a quantitative comparison between flare hard X-ray spectra observed by RHESSI and theoretical predictions. This enables acceleration to be distinguished from transport and the nature of transport effects to be explored.

Methods. Data acquired by the RHESSI satellite were analyzed using full sun spectroscopy as well as imaging spectroscopy methods. Coronal source and footpoint spectra of well observed limb events were analyzed and quantitatively compared to theoretical predictions. New concepts are introduced to existing models to resolve discrepancies between observations and predictions.

Results. The standard thin-thick target solar flare model cannot explain the observations of all events. In the events presented here, propagation effects in the form of non-collisional energy loss are of importance to explain the observations. We demonstrate that those energy losses can be interpreted in terms of an electric field in the flare loop. One event seems consistent with particle propagation or acceleration in lower than average density in the coronal

^{*} This chapter is published in *Astronomy & Astrophysics* **487**, 337 (2008)

¹ Institute of Astronomy, ETH Zurich, CH-8092 Zurich, Switzerland

source.

Conclusions. We find observational evidence for an electric field in flare loops caused by return currents.

5.1 Introduction

Solar flares have been studied in detail both observationally and theoretically ever since their discovery by Carrington (1859). Although increasingly more sophisticated instrumentation provides ever more detailed data, we still lack the basic understanding of many processes at work in a solar flare.

The common flare picture as deduced from hard X-ray (HXR) observations features an HXR source in the corona (coronal or loop-top source, Frost & Dennis 1971; Hudson 1978), and two or more HXR sources (footpoints) in the chromosphere (Hoyng et al. 1981). These sources are thought to be due to bremsstrahlung emission produced by fast electrons accelerated somewhere above the loop. If we assume that a single particle beam creates both coronal and footpoint emission, the most basic model would involve thin target emission at the top of the coronal loop and thick target emission from the footpoints, which both produce characteristic spectra. Wheatland & Melrose (1995) developed a more sophisticated model (intermediate thin-thick target or ITTT model) to fit observations by Yohkoh. They based their model on observations by Feldman et al. (1994), who found high column densities at the loop top, which might act as a thick target below a certain electron energy. In the ITTT model, the shape of the coronal and footpoint non-thermal spectra and the relation between them, observed by Yohkoh, can be explained. The column density in the coronal source determines a critical energy level for the electrons. Electrons that have an energy below this critical energy are stopped in the coronal region. Consequently, the distribution of electron energies measured at the footpoints is depleted in low energy electrons. If the column density is high, the coronal source may act as a thick target to electrons of energies as high as 60 keV, which would leave almost no footpoint emission. Observational evidence for such coronal thick targets were found in RHESSI observations (eg. Veronig & Brown 2004).

Less extreme cases, flares with one or more footpoints, have frequently been observed by RHESSI. To study the spectral time evolution of individual sources, five well-observed events were analyzed by Battaglia & Benz (2006) who focused on the differences between the spectral indices of coronal and footpoint spectra. They found that in two of those events, the differences at specific times as well as the time-averaged difference was significantly larger

than two, ruling out a simple thin-thick target interpretation. In Battaglia & Benz (2007), the spectra of the five events were compared with the predictions of the ITTT model. The authors exploited the order of magnitude improvement in spectral resolution of RHESSI over the 4-point Yohkoh spectra and showed that most RHESSI observations could not be explained by the ITTT model.

Battaglia & Benz (2007) proposed that by considering non-collisional energy loss inside the loop this inconsistency could be resolved. A possible mechanism that causes non-collisional energy loss is an electric field. Accelerating electrons out of the coronal source region drives a return current to maintain charge neutrality in the whole loop. For finite conductivity, Ohm's law implies that an electric field must be present. The beam electrons lose energy because of work expended in moving inside the electric potential. This produces a change in the shape of the electron spectrum at the footpoints. The formation and evolution of these return currents were studied by various authors (e.g. Knight & Sturrock 1977; Spicer & Sudan 1984; Larosa & Emislie 1989; van den Oord 1990). Zharkova & Gordovskyy (2006) proposed that return currents could explain the high energy break observed in flare HXR spectra. Most studies have, however, been theoretical proposals or numerical simulations, based on standard flare values, that do not attempt to explain or reproduce true solar flare observations.

Battaglia & Benz (2007) compared RHESSI spectra to the ITTT-model of Wheatland & Melrose (1995), demonstrating that the qualitative shape and relations between coronal and footpoint-spectrum often do not agree with the model predictions. In this study, we take an additional step by completing a quantitative analysis of the relation linking coronal and footpoint spectra in the context of the thin-thick target model; we demonstrate that, in some cases, electric fields related to return currents can indeed explain the relation between coronal and footpoint spectra.

In Sect. 5.2 we summarize the basic physical concepts applied in the paper. Section 5.3 provides a brief overview of the analyzed events and a description of the spectral analysis. In Sect. 5.4, we describe our calculation of the energy loss required to reproduce the observed footpoint spectrum, constrained by the coronal emission. Our results are presented in Sect. 5.5. In Sect. 5.6, we link those results to the concept of return currents.

5.2 Thin and Thick target emission

Two types of bremsstrahlung emission are distinguished. If the electrons pass a target without losing a significant amount of energy, the corresponding emission is referred to as thin target (Datlowe & Lin 1973). This situation is expected to occur in coronal regions when electrons pass through a target of insufficient column density to stop them. If the electrons are fully stopped inside the target, the resultant emission is called thick target emission (Brown 1971). This is the case for the dense chromospheric material at the footpoints.

For an input power-law electron distribution of the shape $F(E) = A_E E^{-\delta}$, the non-relativistic bremsstrahlung theory predicts power-law photon spectra

$$I(\epsilon) \propto \epsilon^{-\gamma} \quad \text{where} \quad \begin{cases} \gamma = \delta + 1 & \text{in the thin target case} \\ \gamma = \delta - 1 & \text{in the thick target case} \end{cases}$$

The observable distinction between the two emission mechanisms is a difference $\Delta\gamma$ of value 2 in their observed photon spectral indices.

Assuming a final column density in the coronal source, the coronal source spectrum is a thick target at low energies and a thin target at high energies with a break at some critical energy. The footpoint spectrum is depleted at low energies, as low energy electrons do not reach the chromosphere. An illustration of this can be found in Wheatland & Melrose (1995) or Battaglia & Benz (2007).

In the events that we analyze here, a thermal component is present in all observations. Observation of the non-thermal emission is therefore only possible at photon energies higher than 15 keV. For these energies we can assume that the coronal source is a pure thin target and the footpoints are a pure thick target.

5.3 Event description and spectral analysis

The two events that we analyze were described in detail by Battaglia & Benz (2006; 2007). They were selected because of the significant differences between the footpoint and coronal non-thermal spectral index. The first event occurred on 24 October 2003 around 02:00 UT (GOES M7.7), the second on 13 July 2005 around 14:15 UT (GOES M5.1). Both events occurred close to the limb but were not occulted; two footpoints were therefore fully observed in both cases. RHESSI light curves from the time of main emission are shown in

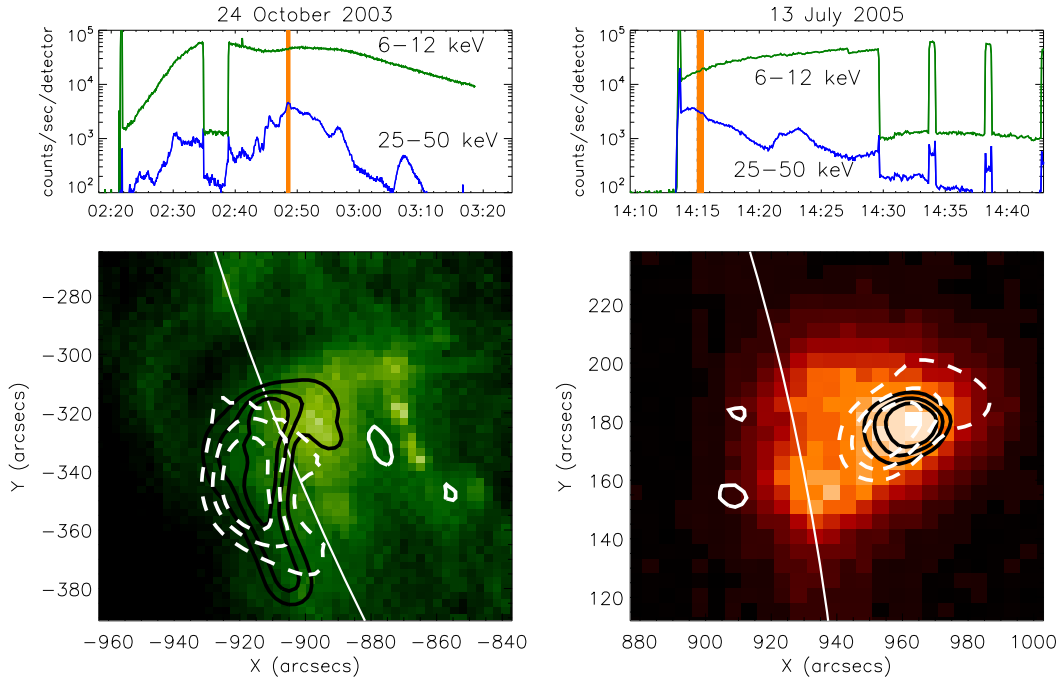


Figure 5.1: *Top:* RHESSI light curves in the 6-12 and 25-50 keV energy band. The analyzed time interval is indicated by the *vertical bar*. *Bottom:* SOHO/EIT image at 24 October 2003 02:47:31 (*left*), GOES SXI image at 13 July 2005 14:19:04 (*right*). The 30 %, 50 % and 70 % contours from RHESSI Pixon images of the coronal source at 12-16 keV (*solid contours*) and 20-24 keV (*dashed contours*, mainly non-thermal emission) are overlaid along with the 50% contour of the footpoint sources at 25-50 keV.

Fig. 5.1. An EIT image of the 24 October 2003 event and a GOES SXI image for the event of 13 July 2005 are presented for orientation. The contours of the coronal source and the footpoints from RHESSI images are overlaid.

5.3.1 Spectral fitting and analysis

The two events were analyzed using imaging spectroscopy with the PIXON algorithm (Metcalf et al. 1996; Hurford et al. 2002). Images were made in a 30 second time interval during which the flux was sufficiently high for good images but pile-up was low. The image times are given in Table 5.1 and shown in Fig. 5.1. The spectra of the footpoints and the coronal source were measured and fitted. The regions of interest from which the spectra were computed were chosen to be a circle around the coronal source and a polygon

around the footpoints to include all of the emission at all energies. The effects of this method of region selection are discussed in Battaglia et al. (2005). As a simplification, the footpoints were treated as one region and the spectrum was fitted with a single power-law. In the presence of the footpoints, the non-thermal emission in coronal sources is difficult to observe. Therefore, two methods of fitting the coronal source were used. First, a thermal component was fitted to the spectrum at low energies and a single power-law to the energies higher than about 25 keV. As a second method, the full sun thermal spectrum was fitted. As shown in Battaglia et al. (2005), the thermal emission observed in full sun spectra is mostly coronal emission. We therefore used the thermal full sun fit as an approximation to the coronal thermal component and completed a power-law fit at the higher energies, while the thermal emission was fixed. This supports the idea that non-thermal emission exists in the coronal source and provides an estimate of the accuracy of the non-thermal coronal fit. The energy ranges for the fits were 8-36 keV for the coronal source and 24-80 keV for the footpoints. All fit parameters are provided in Table 5.1.

In the thin-thick target model an electron beam is assumed to be injected into the center of the coronal source. The column depth that the electrons travel through in the corona is then $\Delta N = n_e \cdot l$, where the path length l is half the coronal source length. From RHESSI images in the 10-12 keV band, the source area A was measured to be the 50% contour of the maximum emission. We approximate the source volume to be $V = A^{3/2}$ and the path length to be $l = \sqrt{A}/2$. Using the observed emission measure EM, the particle density is computed to be $n_e = \sqrt{EM/V}$ which corresponds to a column depth of $\Delta N = \sqrt{EMA^{-1/4}}/2$ expressed in observable terms. A volume filling factor of 1 was assumed for the computation of the density, which will be improved in Sect. 5.5.2. The emission measures were taken from the spectral fits to the coronal source and to full sun spectra. Additionally, temperatures and emission measures observed by GOES were included. This provides a range for the emission measures, temperatures, and column depths, and an estimate of their uncertainty.

5.4 Method

Starting from the assumption that the observed coronal spectrum at high photon energies is caused by thin target emission, we compute the electron distribution and therefore the expected footpoint photon spectrum. This is completed via the following steps.

1. We assume that the observed coronal photon spectrum can be fitted by a power law:

$$F_{obs}^{cs}(\epsilon) = A_{\epsilon}^{cs} \epsilon^{-\gamma^{cs}}, \quad (5.1)$$

where A_{ϵ}^{cs} is the normalization and γ^{cs} the photon spectral index.

2. Using thin target emission, the injected electron spectrum $F(E)$ is then proportional to

$$F(E) = A_E E^{-\delta} \sim \frac{A_{\epsilon}^{cs}}{\Delta N} E^{-\gamma^{cs}+1} \quad (5.2)$$

where ΔN is the column depth the electrons travel through inside the coronal target (Datlowe & Lin 1973).

3. The expected thick target emission $F_{exp}^{fp}(\epsilon)$ caused by this electron distribution in the footpoints can be computed as follows (Brown 1971):

$$F_{exp}^{fp}(\epsilon) = A_{\epsilon,exp}^{fp} \epsilon^{-\gamma_{exp}^{fp}} \sim \frac{A_{\epsilon}^{cs}}{\Delta N} \epsilon^{-(\gamma^{cs}-2)} \quad (5.3)$$

The superscripts fp and cs denote the footpoint and coronal source values, respectively.

4. The normalization and spectral index of $F_{exp}^{fp}(\epsilon)$ is compared to the observed footpoint spectrum $F_{obs}^{fp}(\epsilon)$.

In thin-thick target models, the difference in spectral index $\Delta\gamma = |\gamma^{cs} - \gamma^{fp}|$ is 2. As the observed difference is larger than 2 in the selected events, a mechanism has to be found that causes the electron spectrum to harden while the beam passes down the loop. We present a mechanism that assumes an electric field which causes electrons to lose the energy \mathcal{E}_{loss} independently of the initial electron energy. The resulting spectrum is flatter, although not strictly a power-law function anymore (Fig. 5.2a). The deviation becomes substantial below $2 \mathcal{E}_{loss}$.

The necessary energy loss is determined as follows:

1. We start with the coronal electron distribution as found from Point 2 in the above list.
2. By assuming a thin target, the electron distribution leaves the coronal source and propagates down the loop. A constant energy loss \mathcal{E}_{loss} is subtracted from the electron energies as the energy loss is independent of the electron energy.

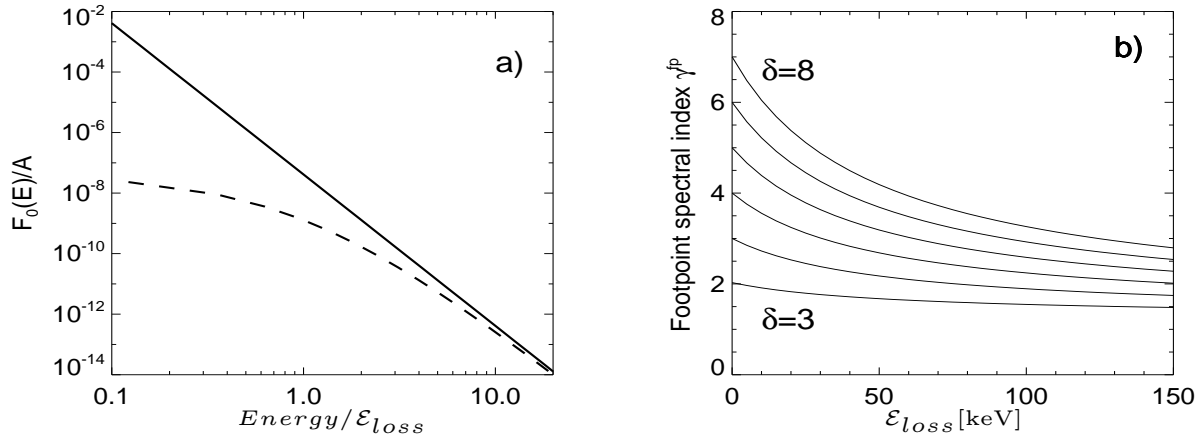


Figure 5.2: a) Normalized electron power-law spectrum (*solid*) and altered spectrum due to a constant energy loss of 30 keV (*dashed*). b) Relation between loss energy \mathcal{E}_{loss} and fitted thick target photon power-law spectral index γ^{fp} for initial electron spectral index $\delta = 3, 4, 5, 6, 7, 8$ in the accelerator.

3. We compute the expected thick target photon spectrum $F_{exp}^{fp}(\epsilon)$ from this altered electron spectrum.
4. A power law is fitted to $F_{exp}^{fp}(\epsilon)$. The fitted energy range is 30-80 keV. This is the range for which footpoint emission is typically observed.

The relation between the energy loss experienced and the corresponding photon spectral index of the best-fit power law function depends on the initial electron spectral index δ and the energy loss \mathcal{E}_{loss} . It is equivalent to the elementary charge times the electric potential between the coronal source and the footpoints. If the initial electron spectral index is 8 for instance, the thick target photon spectral index without energy loss is 7. With increasing energy loss, this value decreases rapidly. The effect is less pronounced when the initial electron spectrum is harder. This is shown in Fig. 5.2b for several values of δ and \mathcal{E}_{loss} . Using the curves in this figure, we can easily determine the energy loss that causes an electron spectrum of spectral index δ to result in a fitted photon spectral index γ^{fp} .

5.5 Results

5.5.1 Observed spectra

Figure 5.3 shows the observed spectra overlaid with the spectral fits. As indicated in Sect. 5.3.1, the thermal fits differ slightly from each-other. The

Table 5.1: Overview of main event properties and fit parameters

Time interval	24 October 2003 02:48:20-02:48:50			13 July 2005 14:15:00-14:15:30		
Area [cm ²] / Volume [cm ³]	7.9 · 10 ¹⁸ / 2.2 · 10 ²⁸			1.7 · 10 ¹⁸ / 2.2 · 10 ²⁷		
	full sun	imspec GOES		full sun	imspec GOES	
Temperature [MK] ^a	21.6	23.2	15.4	23.8	22.3	18.1
Emission measure [10 ⁴⁹ cm ⁻³]	0.98	0.44	3.4	0.22	0.22	0.47
Electron density [10 ¹⁰ cm ⁻³]	2.1	1.4	3.9	3.2	3.2	4.6
Column density [10 ¹⁹ cm ⁻²]	2.9	2.0	5.5	2.1	2.1	3.0
γ^b	footpoints cs fit 1 cs fit2			footpoints cs fit 1 cs fit 2		
F_{50} [photons cm ⁻² s ⁻¹ keV ⁻¹]	2.6	6.2	6.1	2.9	5.1	5.6
	2.0	0.07	0.07	0.88	0.06	0.05

^a Thermal parameters for three different measuring methods (RHESSI full sun fit, RHESSI imaging spectroscopy, GOES).

See also comment in Sect 5.5.1.

^b Two different values (cs fit 1, cs fit 2) for the non-thermal coronal fit, distinguishing the two fitting methods used (compare Sect 5.3.1).

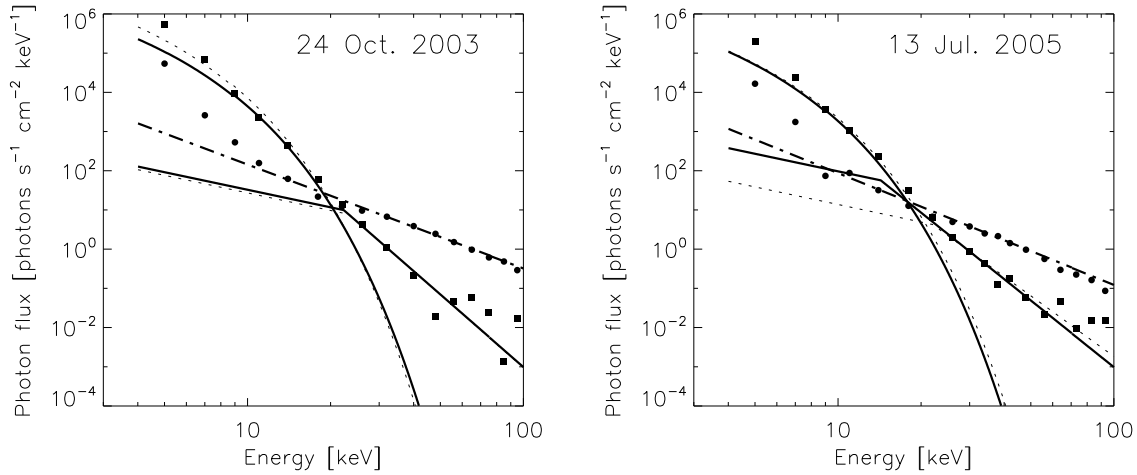


Figure 5.3: Coronal and footpoint source spectra overlaid with the according fits. *Dots* are the measured footpoint spectrum, the *dashed-dotted* line indicates the fit to this spectrum in the range 30-80 keV. *Squares* indicate the observed coronal source spectrum. The *solid* lines provide the thermal and non-thermal fits as found from imaging spectroscopy. The *dotted* lines give the thermal fit to the full sun spectrum and the resulting non-thermal fit in imaging spectroscopy.

main reason why the fits do not agree is the wider energy binning adopted by imaging spectroscopy. With this binning, the atomic lines are not resolved, contrary to full sun spectroscopy.

Using the different fitting methods as an estimate of the uncertainty, an average difference in spectral index of $\Delta\gamma = 3.55 \pm 0.07$ for the event of 24 October 2003 and $\Delta\gamma = 2.45 \pm 0.35$ for the event of 13 July 2005 is found between the coronal source and footpoints.

5.5.2 Expected footpoint emission and energy loss

As described in Sect. 5.4, we computed the electron distribution from the coronal source photon spectrum and the expected thick target emission (footpoint spectrum) caused by this electron distribution. Figure 5.4 shows the measured spectra, the expected footpoint spectrum from a pure thick target, and the footpoint spectrum when introducing energy loss.

To compute the electron flux, the coronal column density is required. As given in Table 5.1, three different values of the column density were estimated. Using those, we are able to reproduce a range of possible electron spectra

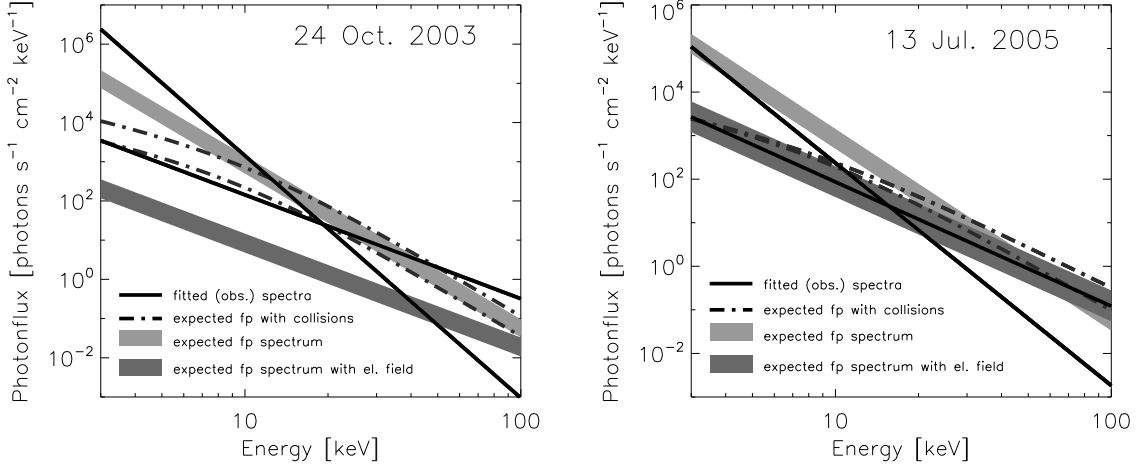


Figure 5.4: Observed (fitted) power-laws of the non-thermal coronal source and footpoints (*solid*). The *light-gray* area indicates the range of expected footpoint spectra without energy loss. The *dark-gray* area marks the range of expected footpoint spectra when energy loss is applied to the electrons to find the same spectral index as the observed footpoint spectrum. The *dash-dotted* lines give the expected spectra at the footpoints if the only transport effect was Coulomb collisions of the beam electrons (cf. Sect. 5.7.4).

(Table 5.2) and, therefore footpoint spectra. The confidence range of the footpoint spectra is indicated by a light gray (green) area in Fig. 5.4.

The derived energy loss depends on the fitted coronal and footpoint spectra. For the two different coronal fitting methods, a range of loss energies $\mathcal{E}_{loss} = [58.0, 59.4]$ keV is found for the event of 24 October 2003 and $\mathcal{E}_{loss} = [8.7, 26]$ keV for the event of 13 July 2005. The normalization of the new spectrum depends on the initial electron distribution. The initial electron distribution is computed according to Eq. (5.2). It depends on the column depth. If the column depth is lower, more electrons are needed to produce the same X-ray intensity. The resulting range of possible spectra is shaded in dark-gray in Fig. 5.4. As shown in the figure, the footpoint spectrum with energy loss reproduces well the observed footpoint spectrum for the event of 13 July 2005.

During the event of 24 October 2003, the predicted footpoint spectrum is, however, an order of magnitude less intense than observed. In the context of the ITTT model, this implies that the electron flux density emanating from the coronal region is higher than predicted. The discrepancy may be explained by density inhomogeneities in the coronal source resulting in a smaller effective

column density. The electron flux is underestimated if the non-thermal X-ray emission originates in regions that are less dense than average. In the following we therefore assume that the coronal source has an inhomogeneous density; this is represented by dense regions with filling factor smaller than 1 for thermal emission and, for the non-thermal coronal source in the 24 October 2003 event, a density that is lower by an order of magnitude. The observations do not allow to determine the filling factor. As can be seen from Fig. 5.1, the coronal source in the event of 13 July 2005 is very compact, while the source in the event of 24 October 2003 is more extended, showing isolated intense regions. This supports the assumption that the density is inhomogeneous in the 24 October 2003 coronal source and the true column density in the X-ray emitting plasma might be smaller than deduced from the measurements. Since $F_{exp}^{fp}(\epsilon)$ is proportional to $1/\Delta N$, an effective column density of an order of magnitude less than the observed could produce the observed footpoint spectrum. In the computations presented in Sect. 5.6, we assume an effective column density $\Delta N_{eff} = \Delta N/14$ for the event of 24 October 2003.

5.6 Return current and electric field

In the above analysis, we assumed that the electrons experienced a constant energy loss while streaming down the loop. We now demonstrate that this energy loss could be caused by an electric potential in the loop that drives a return current. There was much controversy surrounding the precise physical mechanism that generates the return current (eg. Knight & Sturrock 1977; Spicer & Sudan 1984; van den Oord 1990). The basic scenario is the following: We assume that the electrons are accelerated in the coronal source region. When a beam of accelerated electrons, which is not balanced by an equal beam of ions, leaves this region, a return current prohibits charge build-up and the induction of a beam-associated magnetic field. In the return current, thermal electrons move towards the coronal source. Since their velocity is relatively small, they collide with background ions and cause resistivity. Ohm's law then implies the presence of an electric field in the downward direction. The return current density j_{ret} can be derived from the equation of motion for the background electrons (Benz 2002).

$$\left(\frac{\partial}{\partial t} + \nu_{e,i}\right) \mathbf{j}_{ret} = \frac{(\omega_p^e)^2}{4\pi} \mathbf{E}_{ind} + \frac{e}{mc} [\mathbf{j}_{ret} \times (\mathbf{B}_0 + \mathbf{B}_{ind})], \quad (5.4)$$

where B_0 is the guiding magnetic field and B_{ind} the field induced by the beam. We neglect the last term on the right side of Eq. 5.4 by assuming that the beam

and return currents are anti-parallel, oriented along the guiding magnetic field, and that the perpendicular component of B_{ind} vanishes. We then obtain

$$\left(\frac{\partial}{\partial t} + \nu_{e,i}\right) \mathbf{j}_{ret} = \frac{(\omega_p^e)^2}{4\pi} \mathbf{E}_{ind}. \quad (5.5)$$

Since we consider a fixed time interval that is far longer than the collision time, we assume a steady state, neglecting the time derivative of the return current. The equation then takes the form of the classical Ohm's law:

$$\mathbf{j}_{ret} = \frac{(\omega_p^e)^2}{4\pi\nu_{e,i}} \mathbf{E}_{ind} = \sigma \mathbf{E}_{ind}. \quad (5.6)$$

We estimate whether the energy loss computed in Sect. 5.5 is caused by this electric field. From the observations, we estimated the electron loss energy \mathcal{E}_{loss} that the electrons experience in the loop (Sect. 5.5.2). Assuming this loss is caused by the induced electric field E_{ind} and across the distance s from the coronal source to the footpoints (i.e. half the loop length), we compute the electric field to be

$$E_{ind} = \frac{\mathcal{E}_{loss}}{e \cdot s}. \quad (5.7)$$

Using Spitzer conductivity (Spitzer 1965), the term for the return current is related to the observed loss energy by:

$$j_{ret} = 6.9 \cdot 10^6 T_{loop}^{3/2} \frac{\mathcal{E}_{loss}}{e \cdot s} \quad [\text{statamp/cm}^2], \quad (5.8)$$

where T_{loop} is the temperature in the loop.

On the other hand, the beam current density can be written as

$$j_{beam} = \frac{F_{tot}(E)}{A_{fp}} \cdot e \quad [\text{statamp/cm}^2], \quad (5.9)$$

where A_{fp} is the total footpoint area. The total electron flux per second $F_{tot}(E)$ is computed from the observed electron spectrum as follows: Let the electron spectrum be $F(E) = A_e E^{-\delta}$. The total flux of streaming electrons per second above a cutoff energy E_{cut} is then:

$$F_{tot}(E) = \int_{E_{cut}}^{\infty} F(E) dE = \frac{A_e}{\delta - 1} E_{cut}^{-(\delta-1)}. \quad (5.10)$$

In a steady state, the relation

$$j_{beam} = j_{ret} \quad (5.11)$$

is valid.

Comparing the beam current as described in Eq. (5.9) with the return current from the observed energy loss according to Eq. (5.8), we test whether the assumption of Spitzer conductivity holds.

5.6.1 Results

Table 5.2 presents the relevant physical parameters necessary for the derivation of the beam- and return currents. For Spitzer conductivity, the loop temperature T_{loop} is required. It is expected to have a value between the coronal source temperature and the footpoint temperature (see Table 5.2). As a first assumption, a mean temperature of $T_{loop} = 15$ MK is chosen. The loop length is evaluated from RHESSI images, approximating the distance between the sources from the centroid positions and assuming a symmetrical loop structure. This provides a typical half loop length of $4 \cdot 10^9$ cm. The footpoint area is measured from the 50% contour in RHESSI images in the 25-50 keV energy range, yielding a total footpoint area of $\approx (6 - 7) \cdot 10^{17}$ cm². The beam current density depends critically on the electron cut off energy E_{cut} . We use a value of 20 keV. This gives an approximate lower limit to the total amount of streaming electrons.

Using the presented observations, Eq.(5.9) and by assuming Spitzer conductivity (Eq. 5.8), the return current results to be of an order of magnitude higher than the beam current. This contradicts the assumptions of a steady state, and is also unphysical.

5.7 Discussion

5.7.1 Instability

In Sect. 5.6.1, we assumed Spitzer conductivity when computing the return current which produced the unphysical result of $j_{ret} > j_{beam}$. Using Eq. (5.8), the loop temperature required to maintain equality between the return current and beam current ($j_{ret} = j_{beam}$) can be computed. In the 24 October 2003 event, the loop temperature T_{loop} would need to be smaller than 10 MK; in the 13 July 2005 event, T_{loop} should be less than 3.9 MK. Such low loop temperatures are highly unlikely.

However, it is possible that the return current is unstable to wave growth. For an extended discussion of instabilities in parallel electric currents, see

Table 5.2: Values used for the computation of the beam and return currents and computed currents.

Event	24 October 2003	13 July 2005
Assumed loop temperature T_{loop} [MK]	15	15
1/2 Loop length s [cm]	$3.2 \cdot 10^9$	$4.3 \cdot 10^9$
Electron flux $F(E)$ [s^{-1} keV $^{-1}$]	$6.33 \cdot 10^{41} E^{-5.2}$	$1.7 \cdot 10^{40} E^{-4.1}$
	$-1.5 \cdot 10^{42} E^{-5.2}$	$-8.4 \cdot 10^{40} E^{-4.6}$
Electron cutoff energy [keV]	20	20
Total footpoint area [cm 2]	$7.2 \cdot 10^{17}$	$6.2 \cdot 10^{17}$
E_{loss} [keV]	58-59.4	8.7-26
Electric field strength [statvolt/cm]	$(6 - 6.3) \cdot 10^{-8}$	$(6.7 - 20.3) \cdot 10^{-9}$
j_{ret} [statamp/cm 2]	$(2.4 - 2.5) \cdot 10^{10}$	$(2.7 - 8.1) \cdot 10^9$
j_{beam} [statamp/cm 2]	$(5.1 - 14.4) \cdot 10^9$	$(1.9 - 3.6) \cdot 10^8$

e.g. Benz (2002). Instability causes an enhanced effective collision frequency of electrons in the return current and therefore a lower effective conductivity. The ion cyclotron instability develops if the drift velocity of the beam particles V_d exceeds the thermal ion velocity v_{th}^{ion} as follows:

$$V_d \geq 15 \frac{T_i}{T_e} v_{th}^{ion} \quad (5.12)$$

with $v_{th}^{ion} = \sqrt{\frac{k_B T_i}{m_i}}$ and T_e and T_i being the electron and ion temperatures, respectively.

We assume a steady state for which $j_{beam} = j_{ret} = n_e e V_d$, where V_d is the mean drift velocity of the electrons constituting the return current. We therefore express V_d as

$$V_d = \frac{j_{beam}}{n_e e} \quad (5.13)$$

and substitute this expression and that for v_{th}^{ion} in Eq. (5.12). Assuming $T_e = T_i = T_{loop}$ and solving Eq. (5.12) for T_{loop} the instability condition holds

$$T_{loop} \leq 2.3 \cdot 10^8 \left(\frac{j_{beam}}{n_e} \right)^2 \quad [\text{K}]. \quad (5.14)$$

Since the loop temperature and density are not known exactly, this relation is illustrated in Fig. 5.5 for several values of n_e and T_{loop} typical in flare loops. For the values of j_{beam} found for the observations of the two events, we find that instability occurs in the 24 October 2003 event for all values of n_e and T_{loop} in Fig. 5.5. For the 13 July 2005 flare, three distinct regions in the

diagram can be found. The solid line indicates the relation of Eq. (5.14). Below this line, the return current is unstable. At high densities and low temperatures (lower right), the return current is stable and $j_{beam} = j_{ret}$ with Spitzer conductivity. The range of beam currents j_{beam} deduced from the data allows for loop temperatures < 3.9 MK. In the upper right quadrangle, Spitzer conductivity would imply $j_{ret} > j_{beam}$, which is unphysical. If the loop was in this parameter range, the current instability would be most likely saturated and $T_e > T_i$. This would shift the instability threshold in Fig. 5.5 to the right. Further, a loop in the state presented by the uppermost part of the figure (temperature above 10 MK, high density) would be detectable by the RHESSI satellite even in the presence of the coronal source. Since no loop emission is observed, we conclude that the loop is either less dense, cooler or both. The values in the upper right quadrangle are therefore unlikely.

5.7.2 Low energy electron cutoff

In the above computations, a value of 20 keV for the electron cutoff energy E_{cut} was assumed. This value is within the range for which the thermal and non-thermal components of the spectrum intersect. Values around 20 keV or higher are also supported by detailed studies of the exact determination of low-energy cutoffs (eg. Saint-Hilaire & Benz 2005; Veronig et al. 2005; Sui et al. 2007). What if the cutoff energy were substantially lower than 20 keV? A cutoff energy as low as 10 keV would increase the total electron flux and therefore the beam current by an order of magnitude, leading to $j_{ret} \approx j_{beam}$ for Spitzer conductivity. Conductivity could then not be reduced significantly by wave turbulence, and instability would be marginal. If the low energy cutoff were even lower than 10 keV, we would find that $j_{ret} < j_{beam}$. This could not be explained in terms of the model used here.

5.7.3 Source inhomogeneity and filling factor

In the above paragraphs, it was demonstrated that the energy loss for the electrons due to an electric field could resolve the inconsistency in the difference between footpoint and coronal source spectral indices (Sect. 5.5). For the event of the 24 October 2003, this produces footpoint emission that is lower than the observed emission (Fig. 5.4). Images show that the coronal source in this event is not compact, but extended with brighter and darker regions. It is therefore possible that the standard density estimate, which favors high density regions, produces higher densities than average and that the effective column density of the regions, where the largest part of the non-thermal emission

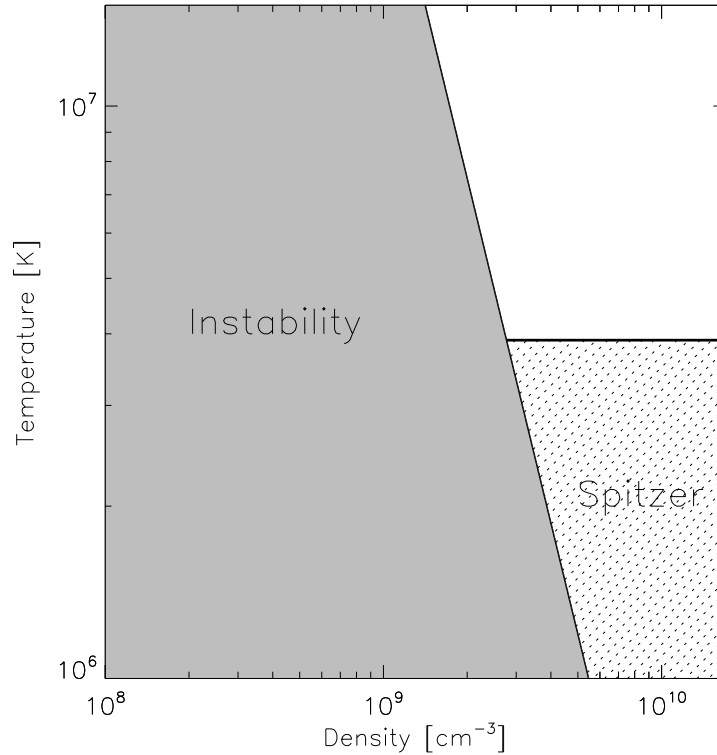


Figure 5.5: Region of instability in the density/temperature space for the event of 13 July 2005. The *grey* region indicates the densities and temperatures T_{loop} for which the return current is unstable (Eq. 5.12). In the lower right part, the return current is stable and $j_{beam} = j_{ret}$ with Spitzer conductivity. The current in the event of 24 October 2003 is unstable for all values of density and temperature in the Figure.

originates, is lower. This would provide a higher expected footpoint emission, in closer agreement with observations.

As mentioned in Sect. 5.3.1, a filling factor of 1 was used for the computation of the column density. A filling factor smaller than 1 would lead to even higher densities of the SXR emitting plasma. However, this would not affect the lower effective column density of the regions, where the HXR emission originates when assuming source inhomogeneity.

5.7.4 Collisions and other possible scenarios

While return currents may not be the only means of attaining non-collisional energy loss, they are the most obvious and best studied. However, other sce-

narios are conceivable, which could produce a harder footpoint spectrum (or a softer coronal spectrum). In the model presented here, collisional energy loss of beam electrons is neglected. This is a valid assumption for the following reasons: If collisions of the beam electrons in the loop were to play an important role, significant HXR emission should originate in the loop. Within the dynamical range limitations of RHESSI, this is not the case. However, GOES SXI and SOHO/EIT images imply that the loop is filled with hot material. To study possible effects of collisions, we compared the change in the electron spectrum and the resulting footpoint spectrum for collisional energy loss and energy loss due to the electric field. The change in the electron spectrum due to collisions depends on the column depth through which the beam passes and was computed by Leach & Petrosian (1981) and Brown & McClymont (1975). We assume a column depth derived from the density in the loop times half the loop length. Assuming the same density as in the coronal source, we derive an upper limit to the collisional effects. The expected footpoint spectrum from purely collisional losses is indicated in Fig. 5.4 as dash-dotted lines. Collisions affect the low energetic electrons most where a significant change in the spectrum is found. At the higher energies observed in this study, the spectrum does not change significantly. The neglect of collisional effects is therefore justified. Brown & Mallik (2008) showed that in certain cases, emission from non-thermal recombination can be important, generating a coronal spectrum that is steeper than expected by the thin-target model. This could also produce a difference in the spectral index that is larger than two. Acceleration over an extended region (as proposed by Xu et al. 2008) could alter the electron distribution at the footpoints. If the distribution was harder at the edge of the region, a spectral index difference larger than 2 would result. A thorough comparison of such models with observations may be the scope of future work.

5.8 Conclusions

The spectral relations between coronal and footpoint HXR-sources provide information about electron transport processes in the coronal loop between the coronal source and the footpoints. Most models neglect these processes in the prediction of the shape and quantitative differences between the source spectra. As shown by Battaglia & Benz (2007), the observations of some solar flares do not fit the predictions of such models, in particular the intermediate thin-thick target model by Wheatland & Melrose (1995): there is a discrepancy concerning the difference in coronal and footpoint spectral indices, which is

expected to be 2.

We have analyzed the two out of five events that display a spectral index difference larger than two in more detail. Such a behavior can be attributed to energy loss during transport that is not proportional to electron energy, but \mathcal{E}_{loss}/E is larger at low energies. Such an energy loss causes the footpoint spectrum to flatten, which increases the difference in spectral indices. Two loss mechanisms come to mind immediately: Coulomb collisions and an electric potential. Figure 4 demonstrates that the assumption of an electric potential reproduces the observations more accurately.

In one of the two events, there remains a discrepancy between the observed and expected footpoint emission, such that the electron flux at the footpoints is larger than predicted. This flux was estimated from the observed non-thermal HXR (photon) flux and the observed thermal emission of the coronal source. We attribute the discrepancy to propagation or acceleration in low density plasma, which also heats the adjacent high-density regions.

The energy loss can therefore be explained by an electric field in the loop associated to the return current, which builds up as a reaction to the electrons streaming down the loop and the associated beam current. In a steady state ($j_{beam} = j_{ret}$), the return current is unstable to wave growth in one event for all realistic temperature and density parameters in the loop. The kinetic current instability drives a wave turbulence that enhances the electric resistivity by many orders of magnitude. This anomalous resistivity in turn significantly enhances the electric field. In the event of 13 July 2005, the return current may be stable if the loop density is high and the temperature is low, and Spitzer conductivity is applied. Both cases (out of five) present strong evidence for a return current in flares for the first time.

Transport effects by return currents constitute a considerable energy input by Ohmic heating into the loop outside the acceleration region. It may be observable in EUV. Comprehensive MHD modeling including the coronal source, the footpoints, and the region in-between, may be the goal of future theoretical work.

Chapter 6

Observations of conduction driven evaporation in the early rise phase of solar flares^{*}

M. Battaglia¹, L. Fletcher² and A. O. Benz¹

Abstract

Context. The classical flare picture features a beam of electrons hitting the chromosphere. The electrons are stopped in the dense plasma, emitting bremsstrahlung in hard X-rays. The ambient material is heated by the deposited energy and expands into the magnetic flare loops, a process termed chromospheric evaporation. In this view hard X-ray emission from the chromosphere is succeeded by soft-X-ray emission from the hot plasma in the flare loop. However, observations of events exist which display a purely thermal coronal source at the beginning of the flare, while the hard X-ray emission only appears minutes later. Such pre-flare clearly contradicts the classical flare picture.

Aims. For the first time, the pre-flare phase of such solar flares is studied in detail. The aim is to understand the early rise phase of these events. We want to explain the time evolution of the observed emission by means of alternative energy transport mechanisms such as heat conduction.

Methods. RHESSI events displaying pronounced pre-flare emission were analyzed in imaging and spectroscopy. The time evolution of images and full sun spectra was investigated and compared to the theoretical expectations from

^{*} This chapter has been submitted for publication in *Astronomy & Astrophysics*

¹ Institute of Astronomy, ETH Zurich, CH-8092 Zurich, Switzerland

² Department of Physics and Astronomy, University of Glasgow, Glasgow G12 8QQ, UK

conduction driven chromospheric evaporation.

Results. During the first one to two minutes of each event, purely thermal emission is observed, while RHESSI images present one X-ray source at thermal energies. After this earliest phase, a small non-thermal tail to higher energies appears in the spectra, becoming more and more pronounced. However, images still only display one X-ray source, indicating that this non-thermal emission is coronal. At a later stage, the typical high energy power-law spectrum becomes pronounced, while images display two additional X-ray sources at non-thermal energies. In the earliest, thermal, phase of the events, the emission measure and density in the corona increase steadily. This indicates that material is added to the coronal region. The most plausible explanation is evaporated material from the chromosphere. Energy provided by a heat flux is capable of driving chromospheric evaporation. We show that the often used classical Spitzer treatment of the conductive flux is not applicable. The conductive flux is saturated. During the preflare-phase, the temperature of the coronal source remains constant or increases. Continuous heating in the corona is necessary to explain this observation.

Conclusions. The observations of the pre-flare phase of four solar flares are consistent with chromospheric evaporation driven by a saturated heat flux. Additionally, continuous heating in the corona is necessary to sustain the observed temperature.

6.1 Introduction

The question of energy conversion during the impulsive phase of a solar flare has converged over the course of the past three decades on a picture featuring an acceleration site in the corona, where particles accelerated to high energies then precipitate along magnetic field lines to the chromosphere. In the chromosphere they lose their energy in the dense plasma, leading to chromospheric heating, as well as the characteristic hard X-ray ‘footpoint’ emission. In addition to radiating and conducting its excess energy away, the heated chromospheric plasma finds a new equilibrium by expanding up the loop, in a process termed ‘chromospheric evaporation’. The observational evidence for a relationship between flare heating and non-thermal electrons in the impulsive phase is reasonably strong. In this paper we use imaging and spectroscopy from the RHESSI satellite (Lin et al. 2002), as well as information from the GOES satellites to investigate flare heating before the flare impulsive phase, apparently in the absence of non-thermal electrons.

Evaporation is usually proposed as the cause of flare extreme ultraviolet

let (EUV) and soft X-ray (SXR) emission (though see Feldman 1990; Acton et al. 1992, who dispute this on several grounds). In the evaporation model, the thermal X-ray emission is a direct effect of the energy deposition in the chromosphere by the electron beam, so that the time-integrated non-thermal hard-X-ray (HXR) flux in a given energy range is proportional to the SXR flux. This was first proposed by Neupert (1968) and since then, the so-called ‘Neupert effect’ has been studied at length by various authors (e.g. Dennis & Zarro 1993; McTiernan et al. 1999; Veronig et al. 2005). Overall the expected proportionality between the time-derivative of the SXRs and the instantaneous HXRs is supported observationally, particularly for impulsive flares, though there is a significant scatter interpreted as due to energy losses from low-temperature radiation, conduction and mass motion. There are also some significant exceptions from this rule - for example, McTiernan et al. (1999) find that the Neupert relationship manifested in about half of the 33 flares they studied. This suggests additional energy input, not related to non-thermal electrons, in the non-Neupert flares. Various authors have also observed impulsive SXR footpoint emission tracking the HXR intensity, rather than its integral (e.g. Hudson et al. 1994). Finally, pre-flare SXR sources, occurring in advance of any HXR emission present a further instance in which thermal emission may also be completely unrelated to non-thermal electrons. This paper concerns the observation and interpretation of such sources.

It has been known for some time that flare-related activity commences prior to the flare impulsive phase. There is a distinction to be drawn between pre-flare activity, which refers to the very earliest stages of the flare before the impulsive phase radiation is detectable, and ‘flare precursor’ events, which are small-scale brightenings in UV to HXR wavelengths happening some tens of minutes before the flare. The first to use the term “pre-flare” and complete a statistical study on flare precursors in X-rays were Bumba & Křivský (1959), who inferred the X-ray behavior via ionospheric disturbances. With the arrival of the *Yohkoh* satellite (Ogawara et al. 1991), the nature of the pre-flare phase was studied in more detail, particularly the relationship between the non-thermal and thermal emissions. It was noted relatively early that high temperature thermal sources were present in the corona substantially before the impulsive phase flare onset (Acton et al. 1992), a result which is clearly at odds with the assumption that electron beams drive evaporation. Comprehensive statistics including an analysis of the spatial relations between pre-flares and the consequent flares has been conducted by Fárník et al. (1996) and Fárník & Savy (1998) based on observations with the *Yohkoh* Soft X-ray Telescope (SXT, Tsuneta et al. 1991). Their definition of pre-flare activity

is a rise in the *Yohkoh* emission above background, five minutes to an hour before the main peak. In the spatially-resolved SXT images it is clear that in several of their sample there is substantial coronal soft X-ray emission occurring several minutes before the start of the impulsive phase (Fárník & Savy 1998). In a study of 10 *Yohkoh* flares, Alexander et al. (1998) also identify line broadening observed with *Yohkoh* Bragg Crystal Spectrometer (Culhane et al. 1991) several minutes before the onset of the impulsive phase, and Harra et al. (2001) show that in one such event the temperature, intensity, and non-thermal line width are changing significantly, well before the start of the hard X-rays. Taken together, the *Yohkoh* observations provide strong evidence for pre-flare coronal activity unrelated to evaporation driven by electron beams.

The Ramaty High Energy Solar Spectroscopic Imager (RHESSI, Lin et al. 2002) offers new opportunities to study pre-flare sources in detail. RHESSI is a HXR telescope, with spectral coverage extending down in energy to the thermal range at ~ 3 -20 keV. Its high spectral resolution (of about 1 keV at energies up to 100 keV) permits spectroscopic diagnostics not available previously, coupled with high spatial resolution (as low as $1''$, depending on the flare) in user-defined energy channels. This offers new temperature and emission measure diagnostics for very hot plasmas (around 10 MK and above) as well as for non-thermal electrons, if present. The RHESSI observations presented here display an increase of low energy X-ray emission, which can be fitted with a thermal spectrum, up to minutes before the rise of the HXR emission. The morphology of these events shows only one source, visible at energies in the thermal regime, while the footpoints only appear at the onset of the HXR emission. We will argue that this indicates that another mechanism of energy transport to the chromosphere may be important, such as heat conduction. One of the consequences of energy transport to the chromosphere is chromospheric evaporation.

The main observational arguments for chromospheric evaporation in flares are (1) that the density of the coronal plasma observed to be emitting in SXR during flares is one or two orders of magnitude greater than is generally measured in the quiet corona (eg. Aschwanden & Acton 2001; Krucker & Lin 2008), requiring a source for the additional material and (2) the presence of upflowing plasma detected via blueshifts in high temperature spectrum lines (Antonucci et al. 1982), in particularly those observations made with imaging spectrometers such as the Coronal Diagnostic Spectrometer (CDS, Harrison et al. 1995) on the Solar and Heliospheric Observatory (SOHO, Domingo et al. 1995). Such flows have been observed in the flare impulsive phase by Milligan et al. (2006a;b) and in the gradual phase by Czaykowska et al. (1999). Evapo-

rative flows have been described as being either ‘gentle’ or ‘explosive’, with the latter occurring when the rate of chromospheric plasma heating greatly exceeds the rate at which it can cool by radiation, conduction or expansion, primarily determined by the ratio between the heating timescale and the hydrodynamic expansion timescale (Fisher et al. 1985). The relatively slow heating rate by conduction from a heated corona makes it a likely source of gentle evaporation. Antiochos & Sturrock (1978) developed an analytic model of conductive driven evaporation in the decay phase of flares, though report that the ‘evaporation’ represented the hydrodynamic redistribution of material already at coronal temperatures, rather than chromospheric material being heated and expanding into the corona. Karpen & Devore (1987) carried out numerical simulations exploring the effects of non-local and saturated heat flux in addition to classical Spitzer heat flux. Observational evidence for such “gentle” evaporation was found by Zarro & Lemen (1988) in observations from the Solar Maximum Mission, and the flows observed by Milligan et al. (2006a) and Czaykowska et al. (1999; 2001) were also found to be consistent with conductive evaporation, due to both their relatively low speeds and absence of significant HXR radiation. We investigate whether this process is relevant also in the pre-flare phase.

In this study, we present the first comprehensive RHESSI-led study of the pre-flare phase of solar flares. The paper is structured in the following way: Section 6.2 describes the flare selection process. In Sect. 6.3 the time evolution of the selected flares is analyzed in spectra and images. A theoretical model to explain the observed time evolution is presented in Sect. 6.4, followed by a Discussion and Conclusions.

6.2 Flare selection

In this study, events with pre-flare activity will be analyzed. The main prerequisite of such a flare is increasing emission in SXR well before the onset of the HXR emission. Therefore, only events the beginning of which was fully observed were considered. The selection criteria are summarized here:

- Offset of more than 700" from disk center to limit projection effects in the study of the flare morphology;
- GOES class larger than M1 to ensure good count rates for imaging;
- The beginning of the event had to be observed with RHESSI;

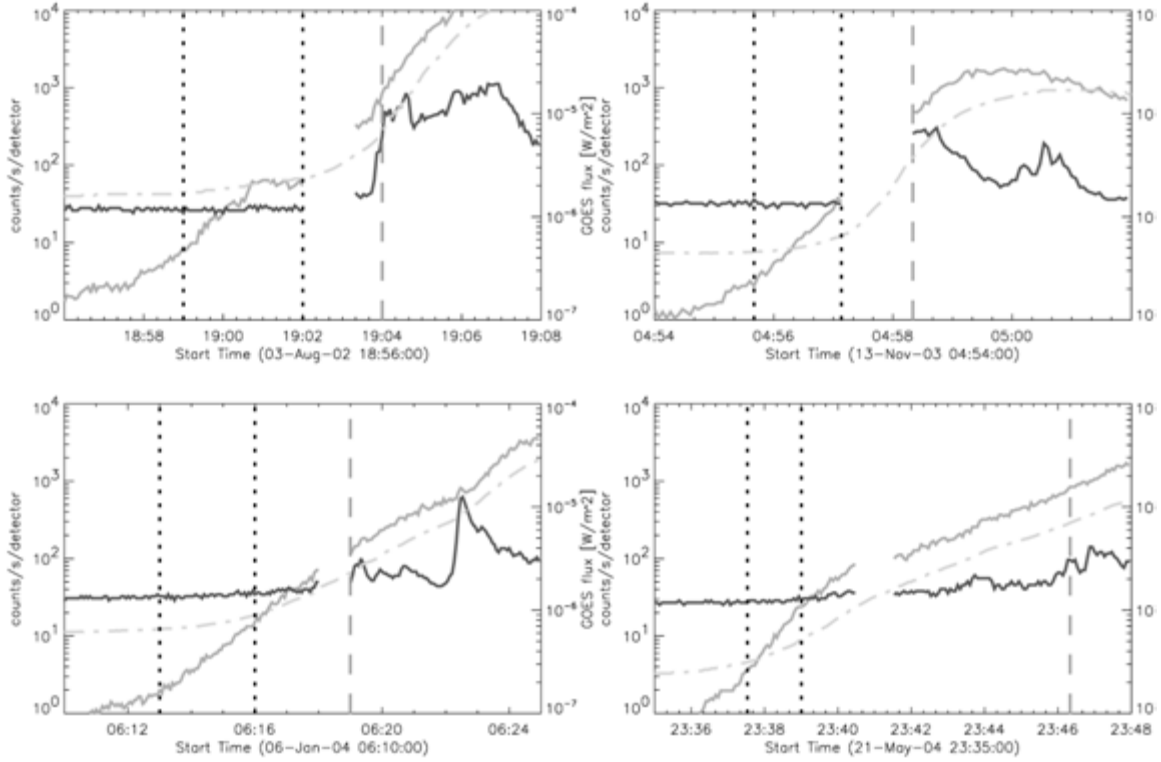


Figure 6.1: RHESSI corrected count rate lightcurves in 6-12 keV and 25-50 keV during the pre-flare and early impulsive phase of the events. Missing data in the RHESSI lightcurves indicate the time interval that was omitted in the analysis due to attenuator state change. The *dotted* vertical lines indicate the time interval of the primary analysis, the *dashed* line gives the start time of the image in which footpoints are observed first. GOES lightcurve (*dash-dotted*).

- SXR & GOES emission had to start increasing at least 1 min before the HXR emission;
- Events with a simple morphology involving one SXR source at the onset and two HXR sources appearing later in the event. This indicates the time when the acceleration process becomes dominant;
- High enough detector livetime ($> 90\%$) for reliable spectroscopy and imaging.

Four events were selected as best suited for this kind of study. Their key parameters are listed in Table 6.1. The RHESSI attenuators were out during the earliest phase of all events with the thin attenuator moving in as the count rates increased, typically after 2-3 minutes.

Table 6.1: Eventlist. The attenuator state is 0 for all events at the very beginning, then changes to 1 as the flux increases. The attenuator times give the rough time interval that must be avoided because of attenuator motion.

Date	Analyzed time	Position	GOES class	Attenuator	Attenuator times
03-Aug-2002	18:59-19:02	912/-271	X1.2	0/1	19:02:20/19:03:10
13-Nov-2003	04:55:40-04:57:12	-977/23	M1.7	0/1	04:57:20/04:58:20
06-Jan-2004	06:13-06:16	-992/88	M5.9	0/1	06:18/06:19
21-May-2004	23:37:30-23:39	-757/-157	M2.6	0/1	23:40:30/23:41:30

6.3 Time evolution of events

The time evolution of the SXR emission in GOES and RHESSI 6-12 keV along with the HXR emission (RHESSI 25-50 keV) is shown in Fig. 6.1. The missing data in the RHESSI lightcurves indicate the time intervals omitted due to attenuator state change. The attenuator state was 0 for all events at the onset of the flare.

We studied the time evolution of the pre-flare phase both in images and spectra. CLEAN and Pixon images (Hurford et al. 2002; Metcalf et al. 1996) during the pre-flare and early impulsive phase were made. The time interval of each image was 30s in order to get high enough count rates throughout the pre-flare phase. Full sun spectra were fitted using approximately the same time binning as used for the images.

6.3.1 Spatial evolution

Figure 6.2 shows CLEAN images of the events taken at the beginning, at the time when a non-thermal component was first fitted and at the time when the footpoints first appear. For each event, 3 energy-bands (6-12, 12-25, 25-50 keV) are shown.

All events start with a single source visible only at the lowest energies in the range 6-12 keV (upper left image of the 9-image panel per flare in Fig. 6.3.1. This is interpreted as a source at the top of a loop (coronal source). After some minutes two additional sources appear at higher energies (25- 50 keV) which are interpreted as chromospheric footpoints (lower right image of each flare in Fig. 6.3.1). In three events the position of the first appearing source is clearly displaced from the footpoint position, implying that there is an actual loop

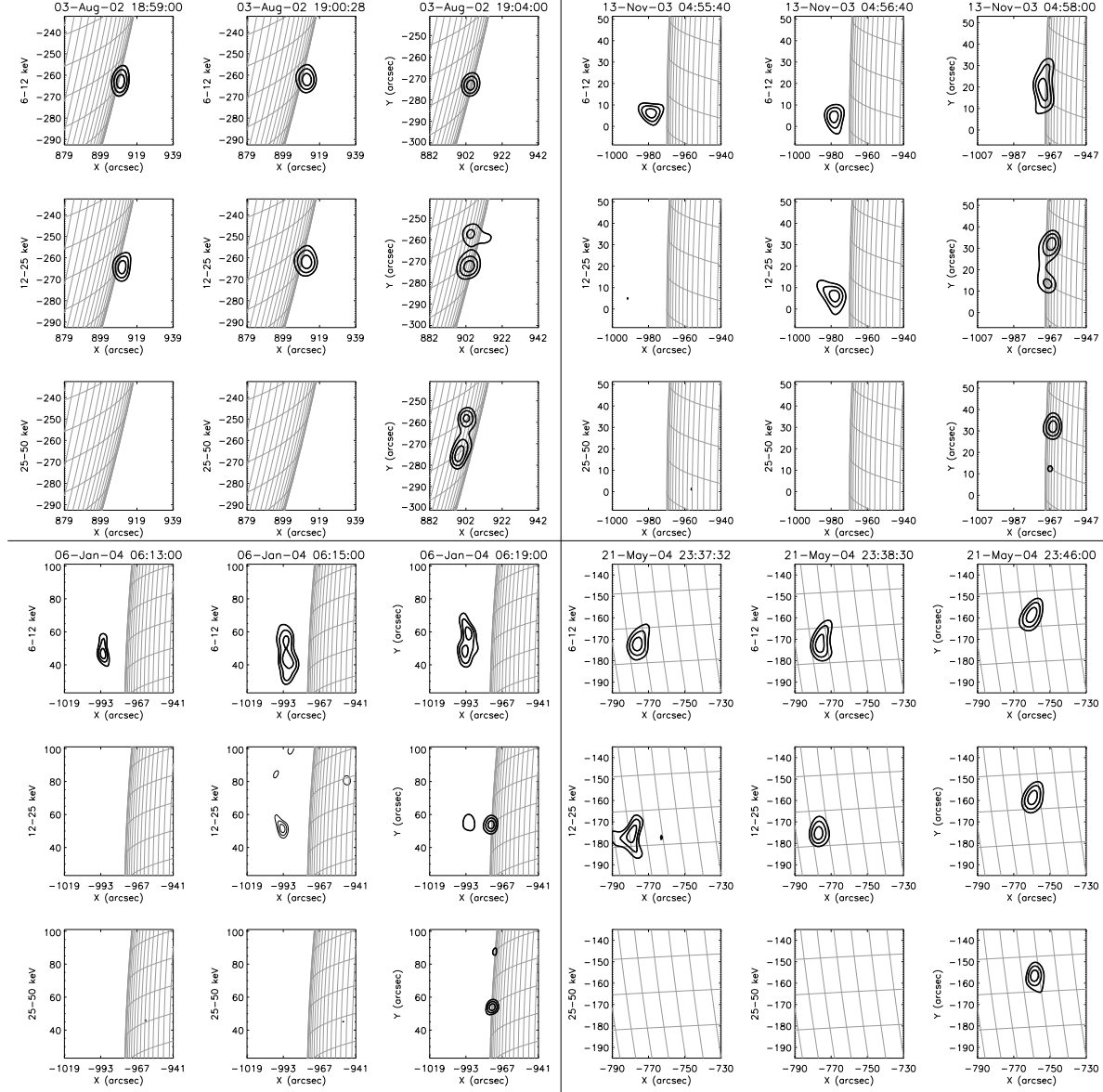


Figure 6.2: Contour plots from CLEAN images (60%, 75% and 90% of maximum flare emission) of all events taken at the first fit interval of the rise phase (*left*), the time interval when a non-thermal component could first be fitted (*middle*) and at the first appearance of the footpoints (*right*). Those times correspond to the times of the spectra shown in Fig. 6.4. The energy bands are 6-12 keV (*top*), 12-25 keV (*middle*) and 25-50 keV (*bottom*).

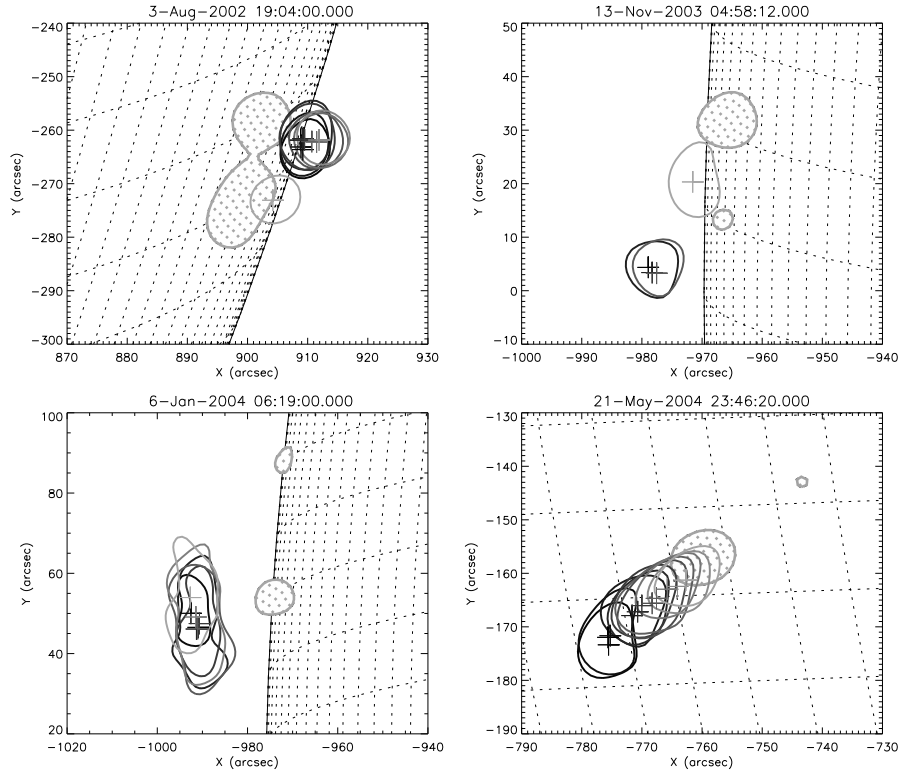


Figure 6.3: Position of the coronal source in time in the energy range 6-12 keV. Time evolution is indicated by 70% intensity contours in colors ranging from black to light with the first appearance of the footpoints (25-50 keV) given as dotted areas in the appropriate color. The centroid position is marked with a *cross* in the corresponding color.

geometry with a coronal source on top and footpoints in the chromosphere. In the fourth event, the separation is not as clear but from the spectral evolution (see next Section) one can still assume a coronal-source-footpoints-geometry.

Movement of coronal sources

We analyzed the time evolution of the source position by measuring the centroid position of the 50% contour in CLEAN and Pixon images in the energy range 6-12 keV. The position from both imaging methods agree within the uncertainties. Figure 6.3 displays the 70% contour from CLEAN images with positions as found from CLEAN. Colors go from black to light (time of first appearance of footpoints). The positions shown indicate the position of the coronal source from the beginning until the time of the first appearance of footpoints, in the same time steps as used in spectroscopy (30s).

In all events, the sources move slightly during the pre-flare phase. The source in the event of 03-Aug-2002 is stable within the position uncertainties during the pre-flare phase, but appears at a displaced location in the last image (at the first appearance of the footpoints). Due to the attenuator state change just before the last image, an interval of about 1 minute is missing. Therefore, one cannot say whether the source moves continuously or not. The same holds for the event of 13-Nov-2003 while the source position of the 6-Jan-2004 event remains constant over time. The 21-May-2004 event is somewhat peculiar, displaying pronounced, continuous source motion. The displacement of the position is clearly larger than the uncertainties.

6.3.2 Spectral evolution

Full-sun photon spectra were fitted in 30 s time intervals, corresponding to the image time intervals. The fitting model consisted of a thermal component fitted from 6 keV and, if possible, a non-thermal component. All four events display a purely thermal spectrum in the first of the analyzed time intervals. This spectroscopic finding is further supported by GOES SXI images (not shown here). These are available for three out of four events and show a soft X-ray source minutes to hours before the RHESSI observations. In RHESSI observations the apparently purely thermal phase lasts one to two minutes, after which a small tail to higher energies becomes visible (Fig. 6.4). At this stage, there are as yet no footpoints observed, indicating that the non-thermal emission is coronal. The tail appears independent of albedo correction and as the events are all near the limb, the influence of albedo on the total flux is minimal. Further, pile-up is not large enough at this stage to account for the emission. It is therefore safe to assume that the tail is real. It can be fitted with a power-law or with a second, very hot thermal component. During the impulsive phase (after attenuator state change) the HXR component becomes very pronounced and clearly distinguishable. Figure 6.4 shows spectra of the selected events, one taken at flare onset and one when the non-thermal tail first appears.

6.3.3 Time evolution of flare parameters

The time evolution of the fit parameters, namely temperature, emission measure and spectral index is shown in Fig. 6.5. The figure displays panels for each event. The top panel of each event shows RHESSI lightcurves in the 6-12 and 25-50 keV energy band. The cross indicates the time of first appearance, and the hardness, of the non-thermal component. The second panel displays

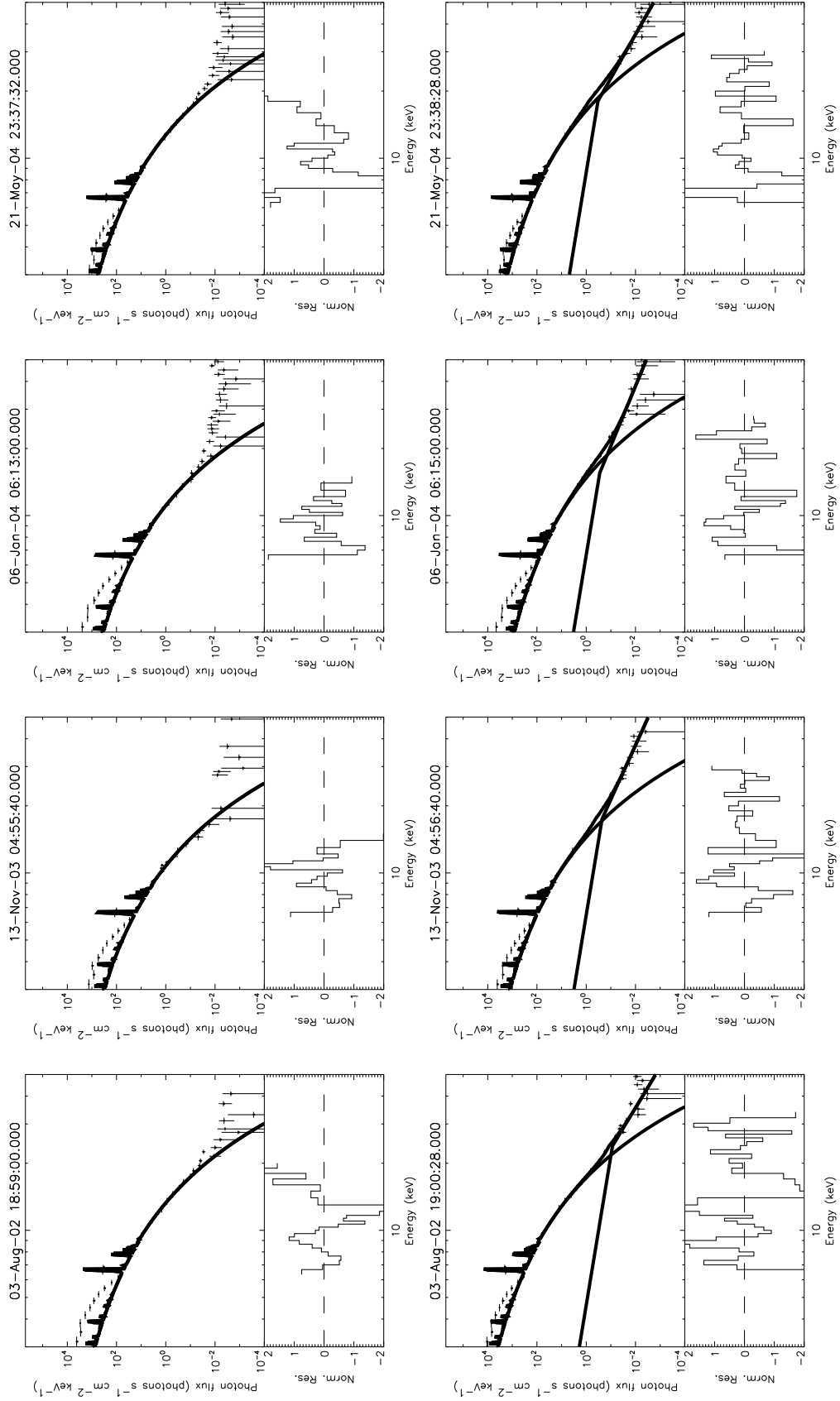


Figure 6.4: Spectra with model fits for 2 time intervals. *Top:* First analyzed time interval. *Bottom:* First interval during which a non-thermal component could be fitted.

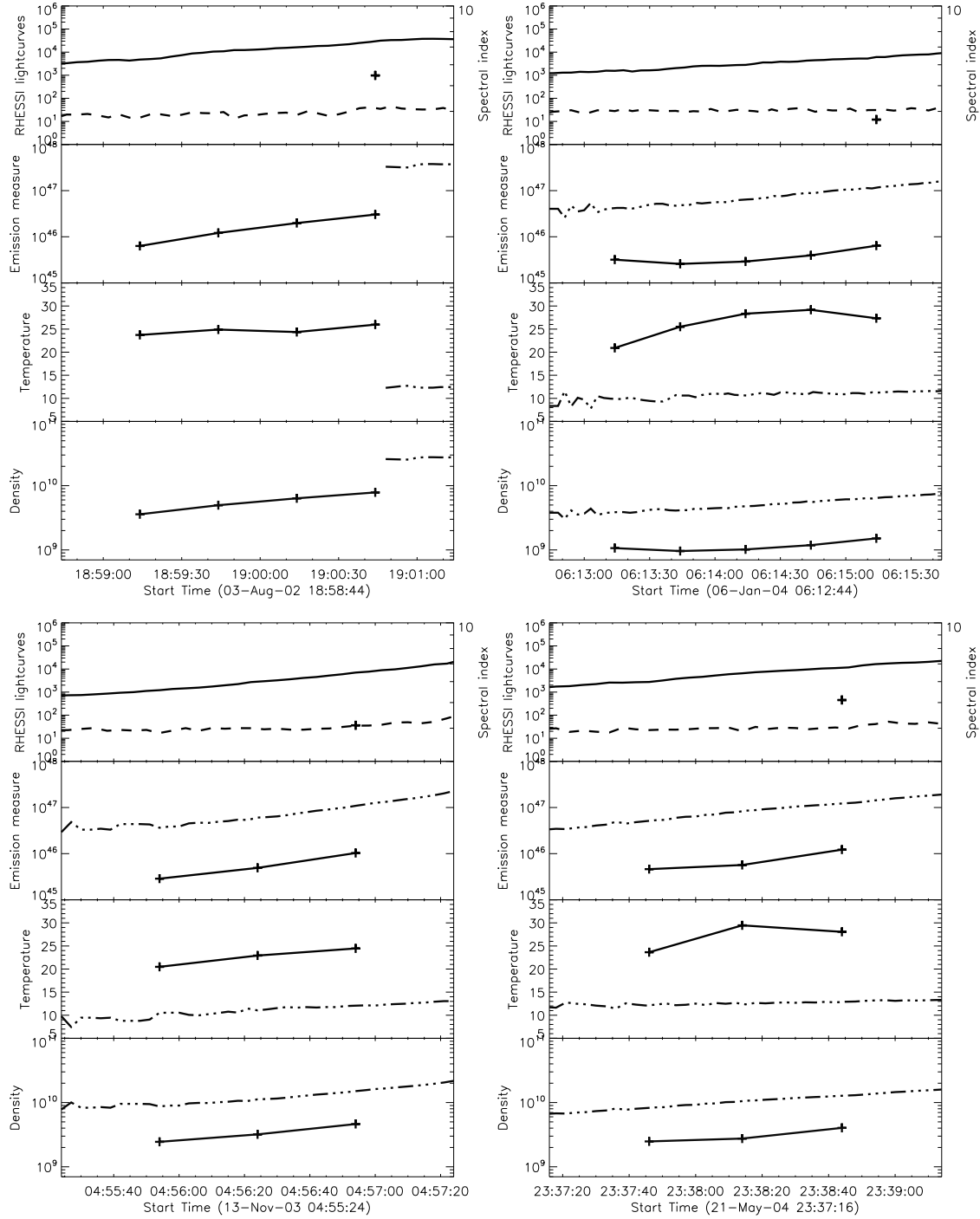


Figure 6.5: Time evolution of the fit parameters for all 4 events. *Top:* RHESSI lightcurves in the 6-12 and 25-50 keV energy band. The cross indicates first appearance and hardness of the non-thermal component. *Second:* Emission measure [cm^{-3}] as computed from RHESSI (*crosses*) and GOES (*dash-dotted*). *Third:* Temperatures [MK], same as for emission measures. *Fourth:* Electron density [cm^{-3}] in the coronal source, same as for emission measures.

the emission measures as determined from RHESSI spectra and GOES. In the third panel, temperatures are presented the same way as the emission measures. The fourth panel shows the electron density estimates. The critical parameter in computing densities is the flare volume. RHESSI images allow an estimate of the volume by measuring the source area A and approximating the volume as $V = A^{3/2}$. Measuring the area from RHESSI images is quite imprecise with large uncertainties. We determined the 50 % contours in CLEAN (de-convolving the CLEAN beam) as well as Pixon images. For both methods, the area is constant over the pre-flare evolution and we made an estimate of the quantitative value of the volume by taking the average of the CLEAN and Pixon values, averaged over time. The average electron density in the coronal source is then given as

$$n_e \approx \sqrt{EM/V}. \quad (6.1)$$

6.4 A theoretical model to explain the observations

In Fig. 6.5 we present the time evolution of flare parameters such as temperature, emission measure and density, as well as images. The observations reveal increasing emission measure and densities over the course of the pre-flare as well as generally increasing temperatures. Assuming a constant, or even increasing, source volume, the density increase can only be attributed to additional material which is added to the coronal source region. The most likely scenario causing such a density increase is chromospheric evaporation. In this scenario, chromospheric plasma (including the transition region) is heated and expands upward the magnetic loops. There are two possible main heating mechanisms for the chromosphere; non-thermal electron beams and thermal conduction. In the former case, a beam of high energetic electrons impinges on the chromosphere, where the particles are completely stopped in the dense target. As a consequence of this energy deposition, the temperature rises. In the latter case, energy is transported from the hot coronal source to the cooler chromosphere by thermal conduction. We are going to discuss the thermal conduction scenario further in the following subsection. Reasons why thermal conduction is favored over particle beams are presented in the discussion.

6.4.1 Theory of thermal conduction

Our model will explain chromospheric evaporation by heating due to energy input from heat conduction. The coronal source is much hotter than the chromospheric plasma, therefore a temperature gradient develops, driving a heat flux downward along the magnetic loop.

The conductive heat flux is given as

$$F_{cond} = \kappa_0 T^{5/2} \frac{\partial T}{\partial s}. \quad (6.2)$$

In classical thermal conduction theory following Spitzer (1965), the conductive coefficient is $\kappa_0 = 10^{-6} \text{ erg cm}^{-1} \text{ s}^{-1} \text{ K}^{-7/2}$. For a flare of half loop length L_{loop} and coronal source temperature T_{cs} , this may be approximated by

$$F_{cond} \approx 10^{-6} \frac{T_{cs}^{7/2}}{L_{loop}} \quad [\text{erg cm}^{-2} \text{ s}^{-1}]. \quad (6.3)$$

However, the maximum heat flux a plasma can carry is limited by a fraction of the thermal energy-flux $F_{therm} = n_e k T_e v_{th}$, where v_{th} is the thermal electron velocity. For sufficiently large temperature gradients, such as occur in solar flares, the heat flux is expected to reach this limit and saturate. Gray & Kilkenny (1980) showed that there are two regimes of flux saturation. A non-classical treatment with local flux limiting is necessary if the electron mean free path $\lambda_{emf} = 5.21 \cdot 10^3 T^2 / n_e$ (Benz 2002) is larger than only 0.12% of the temperature scale length L_{th} . If the electron mean free path even exceeds the temperature scale length, the heat flux becomes non-local in the sense that it depends on the global density and temperature structure of the plasma. Figure 6.6 illustrates the boundary conditions for locally limited and non-local heat flux in the density-temperature plane of typical solar flare values. The locally limited regime is described by Campbell (1984) as a continuous transition from the purely classical treatment to the non-local regime. Depending on the ratio $\mathcal{R} = \lambda_{emf} / L_{th}$, a reduction factor $\varrho < 1$ is applied to the classical heat flux, resulting in an effective heat flux of $F_{red} = \varrho(\mathcal{R}) \cdot F_{cond}$. Campbell (1984) published the values of ϱ for different \mathcal{R} and atomic number Z . Using the values for $Z=1$, we fitted a function of the form

$$\varrho = A \cdot e^{-b(x+c)^2} \quad (6.4)$$

to the values published by Campbell (1984). The parameters are $x = \ln(\mathcal{R})$, $A=1.01$, $b=0.05$, $c=6.63$. Using those values, the locally limited, reduced heat flux can be computed for any \mathcal{R} from Eq. (6.4).

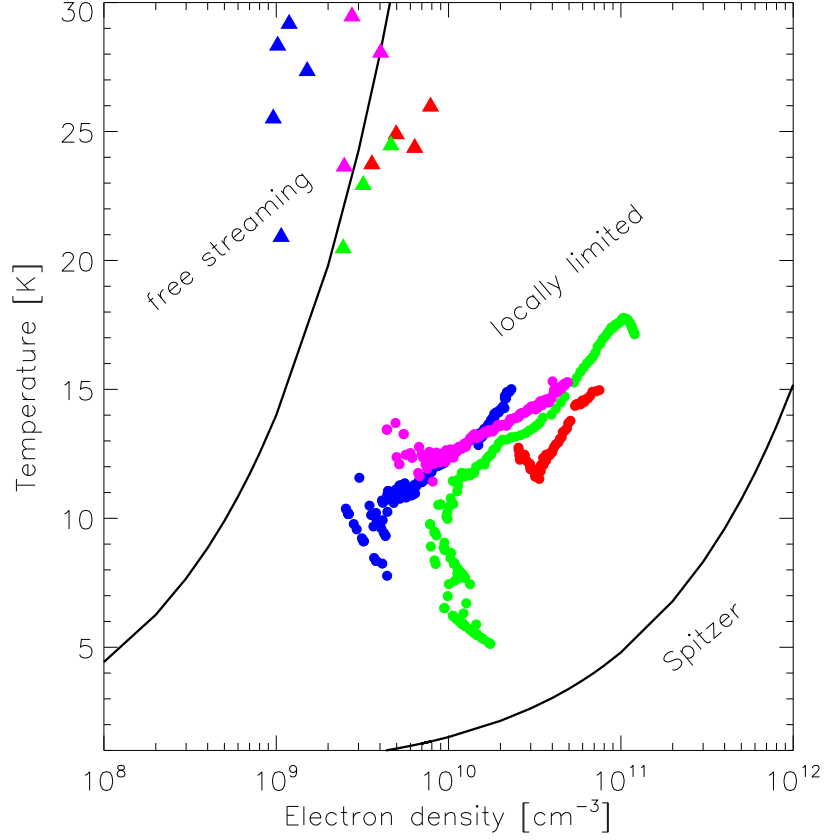


Figure 6.6: Temperature vs. density space of typical flare loop values, indicating the boundaries and regimes for classical thermal conduction, flux limited and non-local conduction. The density and temperature values of the observed events are given as *dots* for GOES and *triangles* for RHESSI observations. Different shades stand for the different events.

In the non-local regime where the electrons are freely streaming and complete saturation is reached, the flux can be expressed as:

$$F_{sat} = 0.53n_em_ev_{th}^3 \quad \text{erg cm}^{-2}\text{s}^{-1} \quad (6.5)$$

(Karpen & Devore 1987).

6.4.2 Observation of thermal conduction

In studies of thermal conduction in flare loops, a classical scenario involving Spitzer conduction is often assumed. Are the conditions in the observed pre-flares consistent with classical conduction or is the flux limited? The densities

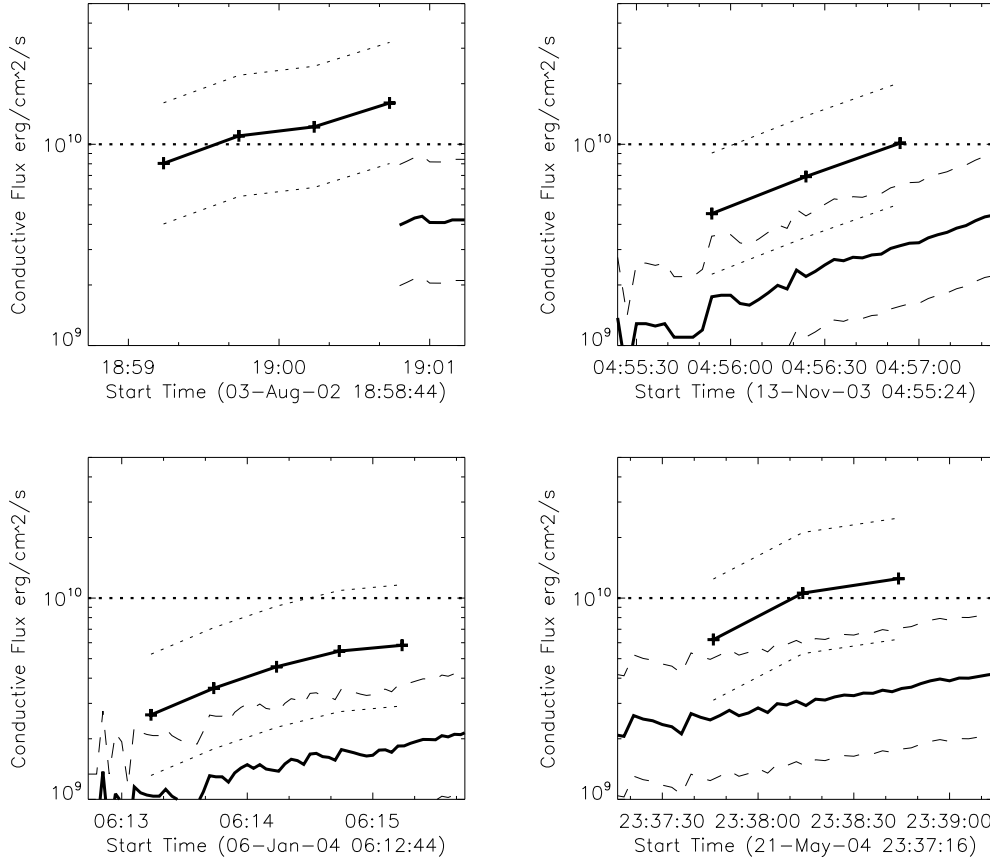


Figure 6.7: Effective conductive flux derived from RHESSI (*crosses on solid line*) and GOES (*solid line*). The *dotted* line marks the threshold energy flux to trigger explosive evaporation (from Fisher et al. 1985). The *thin dashed* lines mark the level of uncertainty (see 6.5).

and temperatures as derived from GOES and RHESSI observations are displayed in Fig. 6.6. Values measured with GOES are given as dots, RHESSI measurements are marked as triangles. GOES typically yields larger emission measures and smaller temperatures than RHESSI. Assuming the same emission volume, this results in higher densities for GOES. The figure reveals that the conditions during the observed times of the pre-flare cannot sustain a classical heat flux, the heat flux is limited. The resulting effective flux was computed from the observed values. Temperatures and densities yield the electron mean free path λ_{mfp} . The temperature scale length L_{th} is given as $L_{th} = T/\Delta T \approx L_{loop}$, where ΔT was approximated as $\Delta T \approx T_{cs}/L_{loop}$. Using an estimated loop half-length of 10^9 cm we computed the ratio \mathcal{R} . The correction factor and therefore the effective heat flux was computed from Eq. (6.4).

The results are displayed in Fig. 6.7, again for both, GOES and RHESSI values.

6.4.3 Chromospheric evaporation

We assume that the heat flux computed in the section above is deposited in the transition region and chromosphere, heating the chromospheric material. The hot material will then expand upward the magnetic loops. This chromospheric evaporation is usually divided into two types; gentle evaporation and explosive evaporation. The determining factors distinguishing the two are the ratios between heating, radiative cooling and expansion rate in the chromosphere. If the heating rate is much smaller than the radiative loss rate, all the deposited energy is radiated away. If the heating rate is only marginally larger than the radiative loss rate, the temperature and pressure rise slowly and the material evaporates gently. If the deposited energy rate exceeds a certain threshold value, the chromospheric plasma is heated to coronal temperatures quickly, a large overpressure develops and explosive expansion of plasma is the consequence. Fisher et al. (1985) derived a value for the critical heating flux of 10^{10} erg cm⁻²s⁻¹ for typical coronal and chromospheric conditions. It is generally assumed that explosive evaporation is associated with the large energy input provided by beams of fast electrons hitting the chromosphere, while gentle evaporation is normally attributed to heating by thermal conduction.

Conduction driven chromospheric evaporation

Can the observed emission measure and density increase in the presented events be explained with chromospheric evaporation driven by the heat flux presented in Sect 6.4.2? The total energy flux in the evaporated plasma is given as

$$F_{up}^{evap} = 3n_e^{evap}kT^{evap}v_{up} = 3m_en_e^{evap}v_{th}^2v_{up} \quad [\text{erg cm}^{-2}\text{s}^{-1}], \quad (6.6)$$

where v_{up} is the velocity of the upward moving plasma, v_{th} the thermal velocity and n_e^{evap} the density of the upflowing plasma.

We use the evolution of the density in the coronal source to estimate v_{up} .

$$\frac{dn_e}{dt} = \frac{\partial n_e}{\partial s} \frac{\partial s}{\partial t} \approx \frac{n_e^{evap}}{L_{loop}} v_{up} \quad (6.7)$$

$$v_{up} \approx \frac{L_{loop}}{n_e^{evap}} \cdot \frac{dn_e}{dt} \quad (6.8)$$

The density of the upflowing plasma cannot be determined from observations. Assuming $n_e^{evap} = n_e$, the density in the coronal source, the upflow velocities derived from Eq. (6.8) range from 20 km s^{-1} to 150 km s^{-1} . This results in an evaporative flux of the order of $10^8 \text{ erg cm}^{-2}\text{s}^{-1}$. Further, the evaporative expansion requires an energy of

$$E_{exp} = \int p \, dl \quad (6.9)$$

where p is the total pressure. Assuming isothermal expansion the expansion energy flux can be computed (see Benz & Krucker 2002):

$$F_{exp} = 2m_e n_e v_{th} v_{up} \ln(L_{loop}/l_i) \quad (6.10)$$

The expansion energy flux is larger than the thermal energy flux (Eq. 6.6) by a factor of $2/3 \ln(L_{loop}/l_i)$ which amounts to about 5.

The total energy flux for evaporation is therefore in the range of $5 \cdot 10^8 \text{ erg cm}^{-2}\text{s}^{-1}$, which is well below the values obtained from the data (Fig. 6.7). The rest of the conducted energy heats the transition region and upper chromosphere to sub-coronal temperatures and is radiated away.

6.5 Discussion

6.5.1 Electron beams in the pre-flare phase

In the above section, we demonstrated that conduction driven chromospheric evaporation can account for observations of pre-flares. Can electron beams below the detection limit do the same? Let us estimate the maximum expected non-thermal electron flux and the expected chromospheric heating rate. We estimate the electron beam strength starting from the observed coronal source spectrum. The first time-interval when non-thermal emission from the corona was observed was used as an estimate of the upper limit to the electron flux, assuming a thin target in the coronal source. If a beam constituting of this electron flux hits the chromosphere, a thick target footpoint spectrum $F_{fp} = AE^{-\gamma}$ is expected. From observations of footpoints and coronal sources (eg. Battaglia & Benz 2006), we know that a flux F_{fp} as found from this estimate would be well observed in images and spectra. Therefore, the effective electron flux that reaches the footpoints has to be about a factor 100 smaller. For the computation of the beam heating rate, we therefore use an assumed footpoint photon flux spectrum $F_{fp}^{eff} = 0.01 \cdot F_{fp}$.

The heating rate of a beam of electrons was derived by Brown (1973) and Lin & Hudson (1976). The rate of energy input per unit volume at column density N and time t is given as

$$I_B(N, t) = 10^7 n(N, t) [x(N, t) + 0.55] \times \frac{A}{a} C(\gamma) (1.1 \cdot 10^{-17} N)^{-(\gamma+1)/2} \quad [\text{erg cm}^{-3}] \quad (6.11)$$

where $n(N, t)$ is the hydrogen density, $x(N, t)$ the fractional ionization, a the cross-section area, A the normalization of the observed photon spectrum, γ the spectral index of the observed photon spectrum and $C(\gamma)$ a function of the β -function and γ . The parameters of the expected footpoint spectrum were used as input for A and γ in Eq. (6.11). As an estimate of the column density, the stopping depth of a 35 keV electron was used according to $N = 10^{17} E_{\text{kev}}^2$ (Tandberg-Hanssen & Emslie 1988). The resulting density $n(N, t)$ and fractional ionization $x(N, t)$ was taken from Brown (1973, Table1). The cross-section area was taken as 10^{17} cm^2 , which corresponds to typical footpoint areas as measured by RHESSI. Finally, the factor $C(\gamma)$ was taken from Fig. 2 in Lin & Hudson (1976). Inserting the above values gives a total energy input of the order of 3-4 $\text{erg cm}^{-3}\text{s}^{-1}$. From the expression of the column density $N = nl$, where l is the path length, l can be determined and by multiplying Eq. (6.11) with l we get an energy input of $5\cdot7\cdot10^7 \text{ erg cm}^{-2}\text{s}^{-1}$, which is two orders of magnitude smaller than the energy input by thermal conduction. Therefore, if there is any chromospheric heating by electron beams in the pre-flare phase, its contribution is minimal compared to the energy input by thermal conduction.

6.5.2 Influence of assumptions

In all computations throughout this work, the values measured in the coronal source were used also for the loop legs. For some parameters, e.g. the electron mean free path λ_{mfp} , those values may not be accurate. For a complete treatment, the temperature and density in the loop is needed. However, those values cannot be determined observationally. If the loop was at the same temperature and density as the coronal source, it would be visible in X-ray images. As no loop emission is observed in the images, the actual loop has to be either less dense or cooler than the coronal source. Thus the coronal source values represent an upper limit to the true conditions in the loop. Smaller temperature could result in an order of magnitude smaller \mathcal{R} . On the other hand, a smaller density could cause an order of magnitude larger ratio \mathcal{R} of

electron mean free path to temperature scale length. The correction factor ϱ (Eq. 6.4) would change by 0.5 to 2, respectively and so would the conductive flux. The resulting upper and lower limits of the conductive flux are indicated by dashed lines in Fig. 6.7. Even if the conductive flux differed by a factor of 2, this would not change the basic interpretation.

The evaporated flux $F_{up}^{evap} \sim n_e T v_{up} \sim T$ only depends on the temperature. It is therefore expected to be at most about a factor of 4 smaller. However, the upflow velocities derived from Eq. (6.8) are proportional to $1/n_e$ and could therefore be up to an order of magnitude larger for smaller densities. Eq. (6.8) may then give velocities higher than the local sound speed which would be unphysical.

6.5.3 Mode of conduction

Our results indicate that the conductive heat flux during the pre-flare phase is non-classical. The temperature gradient between the coronal source region and the chromosphere is so steep that the classical Spitzer conduction is not valid. The conductive flux is locally limited for temperature and density values determined from GOES and may be fully saturated (i.e. the electrons are freely streaming) in the case of the RHESSI measurements. Both situations lead to a reduced heat flux compared to the classical Spitzer conductivity. This finding does not change directly the conclusions drawn from the work presented here. However, it requires that care be taken when computing total flare energy budgets as the energy loss of the coronal source due to conduction may be smaller than anticipated from the assumption of classical Spitzer conductivity.

6.5.4 Acceleration vs. heating

Despite the energy loss in the corona due to the heat flux, increasing temperatures during the pre-flare phase are observed. Continuous heating in the coronal source is therefore necessary to sustain and even increase the observed temperature. A strong candidate heating mechanism is wave-particle interaction as described in the transit-time-damping model (Miller et al. 1996; Grigis & Benz 2006). Such a model could also explain the spectral time evolution of the observations: Depending on the escape time and wave density in the acceleration region, particles are not accelerated to non-thermal energies but remain at a quasi-Maxwellian distribution observationally not distinguishable from a purely thermal plasma at enhanced temperature. For increasing wave density or escape time, particles are accelerated to higher energies, constituting a non-thermal tail which is clearly noticeable in the observations.

However, the three dimensional geometry of the flare site has to be considered and a smooth transition from heating to acceleration at the same site may not reflect reality in two of the presented events. As shown in Fig. 6.3, the position of the coronal source changes over time in the events of 03-Aug-2002 and 13-Nov-2003. Fárník et al. (1996) and Fárník & Savy (1998) made a statistical study on the position of Yohkoh pre-flares and the successive impulsive flares, finding that only in 25% of the observed events were the pre-flare emission and impulsive flare emission spatially coincident. The other events were classified into what the authors termed “distant” and “adjacent/overlapping” events. In the latter case, parts of the pre-flare 50% maximum intensity emission overlap with parts of the main flare emission while in the “distant” events, the two emission patterns are spatially separated. If our two flares indeed fall into the category of distant events, it will not change the interpretation of the pre-flare phase, but care should be taken when interpreting the time-evolution of the spectrum beyond the purely thermal phase.

6.6 Conclusions

The observed increase in thermal emission and SXR emission measure up to minutes before the start of the impulsive flare phase in the four events presented here can be explained by chromospheric evaporation driven by thermal conduction. To compensate for the heat loss, continuous heating in the coronal source is needed. In this early phase, acceleration of particles to non-thermal energies is minimal or non-existent. A scenario following stochastic acceleration is conceivable in which the coronal source region is only heated in the early flare stages. As soon as the acceleration mechanism becomes efficient enough, a tail of non-thermal particles is produced, first visible in the coronal source and eventually in the footpoints.

Chapter 7

Summary and Outlook

Flare physics has come a long way since the first discovery of flares by Carrington (1859). Despite the vast amount of data observed in all wavelengths of the electromagnetic spectrum, many aspects of flare physics are still not well understood.

The goal of this thesis was a better understanding of the particle acceleration in flares and the particle transport processes in flare loops, as well as energy transport and deposition mechanisms. For this purpose, the time evolution and the geometry of flares observed with the RHESSI satellite were studied in images and spectra.

One conclusion that could be drawn from any flare study involving more than one event is that no two flares are quite the same. Small flares are softer than large flares (Chapter 2). The difference in spectral hardness between coronal sources and footpoints is expected to be two from theoretical models. However, differences significantly larger than two as well as differences smaller than two are observed (Chapters 3, 4). Some events even display more than two HXR footpoints, the most famous among them being a large event on 23. July 2002 (Emslie et al. 2003; Holman et al. 2003), while others do not seem to have any footpoint emission at all (Veronig & Brown 2004). While a soft-hard-soft time evolution of the HXR spectrum can often be observed, even in the coronal source (Chapter 3) there are also cases displaying a soft-hard-harder time evolution (eg. Frost & Dennis 1971; Grigis & Benz 2008). Further, some flares experience pronounced pre-heating which cannot be explained within the framework of the standard impulsive flare model (Chapter 6). In the pre-flare phase, thermal conduction seems to be the major energy transport agent as opposed to electron beams. As a consequence of this large variety of flare characteristics, it will be difficult if not impossible to find THE one flare model which can explain all observations.

In the here presented analysis, we concentrated on flares with a “classical” geometry, i.e. one coronal source and two footpoints. Even among those, each

is unique concerning the spectral time evolution and the relation between the coronal source and footpoint spectra. We can explain a large difference in spectral hardness between corona and footpoints with return currents. What about small differences? Can it be explained by physics rather than just instrumental effects? What if we could extend our samples of up to 5 events to 50? Would we see the trends we expect from the small sample? Finally, do we see the start of the acceleration process in pre-flares? If one was to analyze that phase more closely and in the framework of an acceleration model, one could gain valuable insight into the acceleration process.

Of course it would be desirable to have even more and better data to work on those questions. However, for researchers interested in the active Sun and large flares, a long lasting solar activity minimum makes the current times somewhat tedious. The HEDC database (Saint-Hilaire et al. 2002) lists only 2 X-class events in the year 2006 and none in the years 2007 and 2008. In contrast there were 15 registered X-class events during 2002, the first year of the RHESSI operation. On the other hand, these are good times to study the quiet Sun. Hinode provides excellent instruments to observe micro-flares, nano-flares and the quiet Sun and RHESSI was used to estimate the quiet Sun HXR flux (Hannah et al. 2007).

While solar activity will increase eventually, planning for new missions is ongoing. The Solar Dynamics Observatory (SDO) is scheduled for launch in 2010 carrying an EUV imager as well as instruments for magnetic field measurements and helioseismology. The ESA Solar Orbiter and the NASA Solar Sentinels are ambitious projects to go “close up”. They are planned to approach the Sun as close as 0.3 AU enabling the in-situ study of particles accelerated to interplanetary space. The Solar Probe mission is supposed to approach the Sun even further, as close as 4 solar radii. Although those projects are still in the planning phase, the prospects for Solar Cycle 24 and beyond are promising.

The sun is new each day
Heraclitus

Appendix A

Units and unit conversions

Table A.1: Unit conversion cgs to mks

Quantity	cgs	mks
energy	1 erg	10^{-7} J
power	1 erg s $^{-1}$	10^{-7} W
force	1 dyne	10^{-5} N
charge	1 statcoul	$\frac{1}{3} \cdot 10^{-9}$ C
electric field	1 statvolt cm $^{-1}$	$3 \cdot 10^4$ Vm $^{-1}$
current	1 statamp	$\frac{1}{3} \cdot 10^{-9}$ A
current density	1 statamp cm $^{-2}$	$\frac{1}{3} \cdot 10^{-5}$ Am $^{-2}$
magnetic field	1 G	10^{-4} T
electrical conductivity	1 s $^{-1}$	$\frac{1}{3} \cdot 10^{-9}$ siemens m $^{-1}$

Table A.2: Conversions between measures used in solar physics

Wavelength \Leftrightarrow Frequency	1 cm	\Leftrightarrow	29.97925 GHz
Wavelength \Leftrightarrow Energy	1 Å	\Leftrightarrow	12.398413 keV
Energy	1 keV	=	$1.602 \cdot 10^{-9}$ erg
Energy \Leftrightarrow Temperature	1 keV	\Leftrightarrow	11.604 MK
Scales on the Sun, from Earth	972 arcsec	\Leftrightarrow	$7 \cdot 10^{10}$ cm

Appendix B

Conversion of photon to electron spectra

X-ray observations such as the ones made with RHESSI yield a energy/flux *photon* spectrum. To study the physics of a flare, one needs to know the spectrum of the *electrons* which caused the X-ray emission.

Here, I am going to demonstrate the easy and often used approach of forward-fitting a power-law function. Assume the photon spectrum can be approximated by a power-law function in the following way:

$$F(\epsilon) = A_\epsilon \epsilon^{-\gamma} = \frac{F_{norm}}{(\epsilon_{norm})^{-\gamma}} \epsilon^{-\gamma} \quad [\text{photons s}^{-1} \text{cm}^{-2} \text{keV}^{-1}] \quad (\text{B.1})$$

with the photon spectral index γ and the normalization $A_\epsilon = \frac{F_{norm}}{(\epsilon_{norm})^{-\gamma}}$, where F_{norm} is the flux at energy ϵ_{norm} . The photon energy ϵ is given in keV. The parameters γ and A_ϵ can be found by fitting the observed photon spectrum.

In the simplest approach, it is assumed that the corresponding electron spectrum had the shape of a power-law, as well, which can then be written in a similar way:

$$F(E) = A_E E^{-\delta} = \frac{F_{norm}}{(E_{norm})^{-\delta}} E^{-\delta} \quad (\text{B.2})$$

with the electron spectral index δ and the normalization $A_E = \frac{F_{norm}}{(E_{norm})^{-\delta}}$.

The relation between the photon and electron spectrum, in particular between γ and δ and between A_ϵ and A_E depends on whether the electrons are fully stopped in the target (thick target emission) or whether the beam passes through the target without the particles losing a significant amount of energy (thin target).

In a *thick target*, the incident electrons are fully stopped, loosing all their energy to the target. Following Brown (1971) the parameters for the electron spectrum are:

$$\delta = \gamma + 1 \quad (\text{B.3})$$

$$A_E = \frac{4\pi D^2}{Z^2} \frac{K}{\kappa_{BH}} \frac{\gamma(\gamma - 1)}{B(\gamma - 1, 1/2)} A_\epsilon \quad (\text{B.4})$$

or, if we write the normalization A_ϵ in terms of flux and normalization energy:

$$A_E = \frac{4\pi D^2}{Z^2} \frac{K}{\kappa_{BH}} \frac{\gamma(\gamma - 1)}{B(\gamma - 1, 1/2)} \frac{F_{norm}}{(\epsilon_{norm})^{-\gamma}} \quad (\text{B.5})$$

D is the distance of the sun to the earth, B the beta-function, κ_{BH} the Bethe-Heitler constant, and $K = 2\pi e^4 \ln \Lambda$. In this computation, the non-relativistic Bethe-Heitler differential bremsstrahlung cross-section is used. All the constants in one constant give:

$$A_E = 6.44 \cdot 10^{33} \frac{\gamma(\gamma - 1)}{B(\gamma - 1, 1/2)} \frac{F_{norm}}{(\epsilon_{norm})^{-\gamma}} \quad (\text{B.6})$$

In the *thin target* case, the parameters for the electron spectrum are:

$$\delta = \gamma - 1 \quad (\text{B.7})$$

$$A_E = \frac{4\pi D^2}{\Delta N \kappa_{BH} Z^2} \frac{\gamma - 1}{B(\gamma - 1, 1/2)} A_\epsilon \quad (\text{B.8})$$

Energy

The non-thermal power of an injected electron beam is given as:

$$P = \int_{E_c}^{\infty} E \cdot F(E) \, dE \quad (\text{B.9})$$

As a straight power-law extended to low energies would lead to an infinite amount of energy in the particles, a low energy cut off or turnover energy E_c is introduced. The injected power is then given as:

$$P_c = \frac{A_E}{\delta - 2} E_c^{-(\delta-2)} \quad [\text{keVs}^{-1}]. \quad (\text{B.10})$$

The assumption of an electron turnover as opposed to a cutoff, as well as the choice of the cross-section has an influence on the outcome of the above transformations and computation. For a careful investigation of this issue as well as some guidance for dealing with the issue consult Saint-Hilaire & Benz (2005).

Bibliography

- Acton, L. W., Feldman, U., Bruner, M. E., et al. 1992, *Publ. Astron. Soc. Jpn.*, 44, L71
- Alexander, D., Harra-Murnion, L. K., Khan, J. I., & Matthews, S. A. 1998, *Astrophys. J., Lett.*, 494, L235+
- Alexander, D. & Metcalf, T. R. 1997, *Astrophys. J.*, 489, 442
- Antiochos, S. K. & Sturrock, P. A. 1978, *Astrophys. J.*, 220, 1137
- Antonucci, E., Gabriel, A. H., Acton, L. W., et al. 1982, *Sol. Phys.*, 78, 107
- Aschwanden, M. J. 2005, *Physics of the Solar Corona. An Introduction with Problems and Solutions* (2nd edition) (Pour la Science)
- Aschwanden, M. J. & Acton, L. W. 2001, *Astrophys. J.*, 550, 475
- Bai, T., Hudson, H. S., Pelling, R. M., et al. 1983, *Astrophys. J.*, 267, 433
- Battaglia, M. & Benz, A. O. 2006, *Astron. Astrophys.*, 456, 751
- Battaglia, M. & Benz, A. O. 2007, *Astron. Astrophys.*, 466, 713
- Battaglia, M., Grigis, P. C., & Benz, A. O. 2005, *Astron. Astrophys.*, 439, 737
- Benz, A., ed. 2002, *Astrophysics and Space Science Library*, Vol. 279, *Plasma Astrophysics*, second edition
- Benz, A. O. 1977, *Astrophys. J.*, 211, 270
- Benz, A. O. & Grigis, P. C. 2002, *Sol. Phys.*, 210, 431
- Benz, A. O., Grigis, P. C., Csillaghy, A., & Saint-Hilaire, P. 2005, *Sol. Phys.*, 226, 121
- Benz, A. O. & Krucker, S. 2002, *Astrophys. J.*, 568, 413
- Brown, J. C. 1971, *Sol. Phys.*, 18, 489
- Brown, J. C. 1973, *Sol. Phys.*, 31, 143
- Brown, J. C. & Loran, J. M. 1985, *Mon. Not. R. Astron. Soc.*, 212, 245
- Brown, J. C. & Mallik, P. C. V. 2008, *Astron. Astrophys.*, 481, 507
- Brown, J. C. & McClymont, A. N. 1975, *Sol. Phys.*, 41, 135

- Bumba, V. & Křivský, L. 1959, Bulletin of the Astronomical Institutes of Czechoslovakia, 10, 221
- Campbell, P. M. 1984, Phys. Rev. A, 30, 365
- Carrington, R. C. 1859, Mon. Not. R. Astron. Soc., 20, 13
- Cliver, E. W., Dennis, B. R., Kiplinger, A. L., et al. 1986, Astrophys. J., 305, 920
- Culhane, J. L., Bentley, R. D., Hiei, E., et al. 1991, Sol. Phys., 136, 89
- Czaykowska, A., Alexander, D., & De Pontieu, B. 2001, Astrophys. J., 552, 849
- Czaykowska, A., de Pontieu, B., Alexander, D., & Rank, G. 1999, Astrophys. J., Lett., 521, L75
- Datlowe, D. W. & Lin, R. P. 1973, Sol. Phys., 32, 459
- Dennis, B. R. & Zarro, D. M. 1993, Sol. Phys., 146, 177
- Domingo, V., Fleck, B., & Poland, A. I. 1995, Sol. Phys., 162, 1
- Dougherty, B. L., Zirin, H., & Hsu, K. 2002, Astrophys. J., 577, 457
- Dulk, G. A., Kiplinger, A. L., & Winglee, R. M. 1992, Astrophys. J., 389, 756
- Emslie, A. G., Kontar, E. P., Krucker, S., & Lin, R. P. 2003, Astrophys. J., Lett., 595, L107
- Fárník, F., Hudson, H., & Watanabe, T. 1996, Sol. Phys., 165, 169
- Fárník, F. & Savy, S. K. 1998, Sol. Phys., 183, 339
- Feldman, U. 1990, Astrophys. J., 364, 322
- Feldman, U., Doschek, G. A., Behring, W. E., & Phillips, K. J. H. 1996, Astrophys. J., 460, 1034
- Feldman, U., Hiei, E., Phillips, K. J. H., Brown, C. M., & Lang, J. 1994, Astrophys. J., 421, 843
- Fermi, E. 1949, Physical Review, 75, 1169
- Fisher, G. H., Canfield, R. C., & McClymont, A. N. 1985, Astrophys. J., 289, 425
- Fletcher, L. & Hudson, H. S. 2002, Sol. Phys., 210, 307
- Fletcher, L. & Martens, P. C. H. 1998, Astrophys. J., 505, 418
- Fletcher, L., Pollock, J. A., & Potts, H. E. 2004, Sol. Phys., 222, 279
- Frost, K. J. & Dennis, B. R. 1971, Astrophys. J., 165, 655
- Gallagher, P. T., Williams, D. R., Phillips, K. J. H., et al. 2000, Sol. Phys., 195, 367

- Gan, W. Q. 1998, *Astrophys. Space. Sci.*, 260, 515
- Garcia, H. A. 1994, *Sol. Phys.*, 154, 275
- Golub, L., Deluca, E., Austin, G., et al. 2007, *Sol. Phys.*, 243, 63
- Gray, D. R. & Kilkenny, J. D. 1980, *Plasma Physics*, 22, 81
- Grigis, P. C. & Benz, A. O. 2004, *Astron. Astrophys.*, 426, 1093
- Grigis, P. C. & Benz, A. O. 2005, *Astron. Astrophys.*, 434, 1173
- Grigis, P. C. & Benz, A. O. 2006, *Astron. Astrophys.*, 458, 641
- Grigis, P. C. & Benz, A. O. 2008, *Astrophys. J.*, 683, 1180
- Hannah, I. G., Hurford, G. J., Hudson, H. S., Lin, R. P., & van Bibber, K. 2007, *Astrophys. J., Lett.*, 659, L77
- Harra, L. K., Matthews, S. A., & Culhane, J. L. 2001, *Astrophys. J., Lett.*, 549, L245
- Harrison, R. A., Sawyer, E. C., Carter, M. K., et al. 1995, *Sol. Phys.*, 162, 233
- Hey, J. S. 1946, *Nature*, 157, 47
- Holman, G. D. 1985, *Astrophys. J.*, 293, 584
- Holman, G. D., Sui, L., Schwartz, R. A., & Emslie, A. G. 2003, *Astrophys. J., Lett.*, 595, L97
- Hoyng, P., Duijveman, A., Machado, M. E., et al. 1981, *Astrophys. J., Lett.*, 246, L155+
- Hudson, H. S. 1978, *Astrophys. J.*, 224, 235
- Hudson, H. S. 1991, *Sol. Phys.*, 133, 357
- Hudson, H. S. & Fárník, F. 2002, in *ESA Special Publication, Vol. 506, Solar Variability: From Core to Outer Frontiers*, ed. J. Kuijpers, 261–264
- Hudson, H. S., Strong, K. T., Dennis, B. R., et al. 1994, *Astrophys. J., Lett.*, 422, L25
- Hurford, G. J., Schmahl, E. J., Schwartz, R. A., et al. 2002, *Sol. Phys.*, 210, 61
- Isobe, T., Feigelson, E. D., Akritas, M. G., & Babu, G. J. 1990, *Astrophys. J.*, 364, 104
- Jones, F. C. & Ellison, D. C. 1991, *Space Science Reviews*, 58, 259
- Kahler, S. W. 1982a, *Astrophys. J.*, 261, 710
- Kahler, S. W. 1982b, *J. Geophys. Res.*, 87, 3439
- Kane, S. R. & Anderson, K. A. 1970, *Astrophys. J.*, 162, 1003
- Karpen, J. T. & Devore, C. R. 1987, *Astrophys. J.*, 320, 904

- Kerdr on, A. & Delouis, J.-M. 1997, in *Lecture Notes in Physics*, Berlin Springer Verlag, Vol. 483, *Coronal Physics from Radio and Space Observations*, ed. G. Trottet, 192–+
- Kiplinger, A. L. 1995, *Astrophys. J.*, 453, 973
- Knight, J. W. & Sturrock, P. A. 1977, *Astrophys. J.*, 218, 306
- Kosugi, T., Sakao, T., Masuda, S., et al. 1992, *Publ. Astron. Soc. Jpn.*, 44, L45
- Krucker, S., Christe, S., Lin, R. P., Hurford, G. J., & Schwartz, R. A. 2002, *Sol. Phys.*, 210, 445
- Krucker, S. & Lin, R. P. 2008, *Astrophys. J.*, 673, 1181
- Labrum, N. R. 1972, *Sol. Phys.*, 27, 496
- Larosa, T. N. & Emslie, A. G. 1989, *Sol. Phys.*, 120, 343
- Leach, J. & Petrosian, V. 1981, *Astrophys. J.*, 251, 781
- Lin, R. P., Dennis, B. R., Hurford, G. J., et al. 2002, *Sol. Phys.*, 210, 3
- Lin, R. P. & Hudson, H. S. 1976, *Sol. Phys.*, 50, 153
- Lin, R. P. & Schwartz, R. A. 1987, *Astrophys. J.*, 312, 462
- Litvinenko, Y. E. 1996, *Astrophys. J.*, 462, 997
- Longair, M. S. 1992, *High energy astrophysics. Vol.1: Particles, photons and their detection* (*High Energy Astrophysics*, by Malcolm S. Longair, pp. 436. ISBN 0521387736. Cambridge, UK: Cambridge University Press, March 1992.)
- Lu, E. T. & Hamilton, R. J. 1991, *Astrophys. J., Lett.*, 380, L89
- Lu, E. T., Hamilton, R. J., McTiernan, J. M., & Bromund, K. R. 1993, *Astrophys. J.*, 412, 841
- Masuda, S., Kosugi, T., Hara, H., Tsuneta, S., & Ogawara, Y. 1994, *Nature*, 371, 495
- Matthews, S. A., van Driel-Gesztelyi, L., Hudson, H. S., & Nitta, N. V. 2003, *Astron. Astrophys.*, 409, 1107
- McTiernan, J. M., Fisher, G. H., & Li, P. 1999, *Astrophys. J.*, 514, 472
- McTiernan, J. M., Kane, S. R., Loran, J. M., et al. 1993, *Astrophys. J., Lett.*, 416, L91+
- Messmer, P., Benz, A. O., & Monstein, C. 1999, *Sol. Phys.*, 187, 335
- Metcalf, T. R. & Alexander, D. 1999, *Astrophys. J.*, 522, 1108
- Metcalf, T. R., Hudson, H. S., Kosugi, T., Puetter, R. C., & Pina, R. K. 1996, *Astrophys. J.*, 466, 585

- Mewe, R., Gronenschild, E. H. B. M., & van den Oord, G. H. J. 1985, *Astron. Astrophys. Suppl. Ser.*, 62, 197
- Miller, J. A., Cargill, P. J., Emslie, A. G., et al. 1997, *J. Geophys. Res.*, 102, 14631
- Miller, J. A., Larosa, T. N., & Moore, R. L. 1996, *Astrophys. J.*, 461, 445
- Milligan, R. O., Gallagher, P. T., Mathioudakis, M., et al. 2006a, *Astrophys. J., Lett.*, 638, L117
- Milligan, R. O., Gallagher, P. T., Mathioudakis, M., & Keenan, F. P. 2006b, *Astrophys. J., Lett.*, 642, L169
- Nakajima, H., Nishio, M., Enome, S., et al. 1994, *IEEE Proceedings*, 82, 705
- Narain, U. & Ulmschneider, P. 1990, *Space Science Reviews*, 54, 377
- Narain, U. & Ulmschneider, P. 1996, *Space Science Reviews*, 75, 453
- Neupert, W. M. 1968, *Astrophys. J., Lett.*, 153, L59+
- Ogawara, Y., Takano, T., Kato, T., et al. 1991, *Sol. Phys.*, 136, 1
- Orwig, L. E., Frost, K. J., & Dennis, B. R. 1980, *Sol. Phys.*, 65, 25
- Parks, G. K. & Winckler, J. R. 1969, *Astrophys. J., Lett.*, 155, L117+
- Petrosian, V., Donaghy, T. Q., & McTiernan, J. M. 2002, *Astrophys. J.*, 569, 459
- Phillips, K. J. H., Chifor, C., & Dennis, B. R. 2006, *Astrophys. J.*, 647, 1480
- Saint-Hilaire, P. & Benz, A. O. 2005, *Astron. Astrophys.*, 435, 743
- Saint-Hilaire, P., von Praun, C., Stolte, E., et al. 2002, *Sol. Phys.*, 210, 143
- Schwartz, R. A. 1996, *Compton Gamma Ray Observatory Phase 4 Guest Investigator Program: Solar Flare Hard X-ray Spectroscopy*, Technical Report, NASA Goddard Space Flight Center
- Shibata, K. & Yokoyama, T. 1999, *Astrophys. J., Lett.*, 526, L49
- Simnett, G. M. & Benz, A. O. 1986, *Astron. Astrophys.*, 165, 227
- Smith, D. M., Lin, R. P., Turin, P., et al. 2002, *Sol. Phys.*, 210, 33
- Spicer, D. S. & Sudan, R. N. 1984, *Astrophys. J.*, 280, 448
- Spitzer, L. 1965, *Physics of fully ionized gases* (Interscience Tracts on Physics and Astronomy, New York: Interscience Publication, 1965, 2nd rev. ed.)
- Sui, L., Holman, G. D., & Dennis, B. R. 2007, *Astrophys. J.*, 670, 862
- Tandberg-Hanssen, E. & Emslie, A. G. 1988, *The physics of solar flares* (Cambridge and New York, Cambridge University Press, 1988, 286 p.)
- Tsuneta, S., Acton, L., Bruner, M., et al. 1991, *Sol. Phys.*, 136, 37

- Vaiana, G. S., van Speybroeck, L., Zombeck, M. V., et al. 1977, *Space Science Instrumentation*, 3, 19
- van Beek, H. F. & de Feiter, L. D. 1973, in *Solar Activity and Related Interplanetary and Terrestrial Phenomena*, ed. J. Xanthakis, 103–+
- van den Oord, G. H. J. 1990, *Astron. Astrophys.*, 234, 496
- Veronig, A. M. & Brown, J. C. 2004, *Astrophys. J., Lett.*, 603, L117
- Veronig, A. M., Brown, J. C., Dennis, B. R., et al. 2005, *Astrophys. J.*, 621, 482
- Wheatland, M. S. & Melrose, D. B. 1995, *Sol. Phys.*, 158, 283
- Xu, Y., Emslie, A. G., & Hurford, G. J. 2008, *Astrophys. J.*, 673, 576
- Zarro, D. M. & Lemen, J. R. 1988, *Astrophys. J.*, 329, 456
- Zharkova, V. V. & Gordovskyy, M. 2006, *Astrophys. J.*, 651, 553

Acknowledgments

As with any major undertaking, a PhD cannot be achieved without help, be it moral, financial or professional. I got plenty of it all from various people. First of all I want to express my gratitude to Prof. Arnold Benz for giving me the chance to proof that also a researcher with just average marks in some random oral exam can be a good researcher. With patience and enthusiasm he shared his substantiated knowledge of flares and plasma physics, guiding me to new questions and projects. And he gave me the opportunity of presenting my work at many conferences and meetings, visiting places such as San Francisco, Boston, Berlin or Glasgow along the way. I would also like to thank Prof. Marcella Carollo and Dr. Lyndsay Fletcher who kindly agreed to be my co-examiners.

Special thanks go to Paolo Grigis and Pascal Saint-Hilaire. They taught me all the little helpful tricks in using RHESSI data, not to mention Paolo's countless hours of IDL-tutorials.

A little distraction from research was offered by Stephen Marsden when he initiated a Dungeons & Dragons roleplaying group. Long nights with a lot of fast food and laughter gave me the chance of being with old friends from undergraduate days such as Simone Weinmann, Christian Thalmann and Athman Boukhaoua but also to make new friends with people from the Institute, namely René Holzreuter. His visits to my office to discuss D&D questions often turned into chats far beyond just D&D.

Be it for a coffee, a chat, a little encouragement, a new muffin recipe or the root-password, the following people made life at IfA just a little easier: Simon Bruderer, Christian Monstein, Susanne Wampfler, Esther Buenzli, Alessandra Telleschi, Kevin Briggs, Owen Matthews, Manuel Güdel, Svetlana Berdyugina, Dominique Fluri, Alexander Shapiro, Laure Fouchet, Lucia Kleint, Richard Wenzel, Barbara Codoni and Peter Steiner. Not to forget Nadine Afram with whom I shared countless 'Thai-curry-pasta' lunches, gossiping and sharing the smaller and larger troubles of life.

Special thanks go to my parents. They brought me up in the conviction that I can become anything I like and supported my career-choices all along the way.

I am also very grateful to my late step-father, Remo Allemann. He taught me to take life as it is, to live in the present and make the best out of situations you cannot influence - or at least to try. Many thanks also to my recently deceased Gromi for dreaming my dreams with me and to Gropi who passed the “physics-virus” on to me.

The last and most special thanks go to Michi Gysel, the man in my life. He moved to Zürich to be with me, he supported me in every way possible, he keeps me down to earth by climbing the highest mountains with me.

List of Publications

Publications as first author

- Observations of conduction driven evaporation in the early rise phase of solar flares
Marina Battaglia, Lyndsay Fletcher & Arnold Benz
2009, submitted to A&A
- Observational evidence for return currents in solar flare loops
Marina Battaglia & Arnold O. Benz,
2008, A&A, **487**, 337
- Exploring the connection between coronal and footpoint sources in a thin-thick target solar flare model
Marina Battaglia & Arnold O. Benz,
2007, A&A, **466**, 713
- Relations between concurrent hard X-ray sources in solar flares
Marina Battaglia & Arnold O. Benz,
2006, A&A, **456**, 751
- Size dependence of solar X-ray flare properties
Marina Battaglia, Paolo C. Grigis & Arnold O. Benz,
2005, A&A, **439**, 737

Publications as co-author

- Implications of X-ray observations for electron acceleration and propagation in solar flares
Holman G. et al.
2008, Space Science Reviews, submitted
- Hard X-ray emission from the solar corona
Krucker S. et al.
2007, A&A Review, in press

- Particle acceleration in solar flares: observations versus numerical simulations

Arnold O. Benz, Paolo C. Grigis and Marina Battaglia
2006, Plasma Phys. Control. Fusion, **48**, B115-B121

Curriculum Vitae

Name	Marina Battaglia
Date of birth	October 23, 1979
Place of birth	Chur, Switzerland
Nationality	Swiss

2008	Doctoral Thesis <i>Particle kinematics in solar flares: observations and theory</i> Thesis supervisor: Prof. Dr. Arnold O. Benz
2004 - 2008	Research assistant at Institute of Astronomy, ETH Zürich
2004	dipl. phys. ETH Diploma Thesis: <i>Properties of solar flares of different size observed by RHESSI</i> Supervisor: Prof. Dr. Arnold O. Benz
1999 - 2004	Studies of Physics at ETH Zürich with focus on Astrophysics and Particle Physics
1999	Matura Typus C
1994 - 1999	Kantonsschule Chur

Member of the Swiss Society of Astrophysics and Astronomy (SGAA)

